

Stefan Marsen

The Spatio-temporal Structure of Electrostatic Turbulence in the WEGA Stellarator

IPP 13/11
Oktober, 2008

The Spatio-temporal Structure of Electrostatic Turbulence
in the WEGA Stellarator

I N A U G U R A L D I S S E R T A T I O N

zur

Erlangung des akademischen Grades eines
doctor rerum naturalium (Dr. rer. nat.)

an der Mathematisch-Naturwissenschaftlichen Fakultät

der

Ernst-Moritz-Arndt-Universität Greifswald

vorgelegt von

Stefan Marsen

geboren am 28.6.1977

in Frankfurt(Main)

Greifswald, im März 2008

Dekan: Prof. Dr. Klaus Fesser
1. Gutachter: Prof. Dr. Friedrich Wagner
2. Gutachter: Prof. Dr. Ulrich Stroth
Tag der Promotion: 30.05.2008

Zusammenfassung

Ziel der vorliegenden Arbeit ist eine ausführliche Charakterisierung elektrostatischer Turbulenz im Stellarator WEGA, sowie die Identifikation der zugrundeliegenden Instabilität. Die zur Untersuchung der räumlich-zeitlichen Struktur der Turbulenz notwendige Auflösung wird durch eine Vielzahl von Langmuir Sonden erreicht.

Die Turbulenz in WEGA wird von Driftwellen dominiert. Dies wird durch die Beobachtung einer Reihe markanter, aus dem physikalischen Mechanismus der Driftwelle resultierender, Eigenschaften gezeigt. Die Phasenverschiebung zwischen Dichte- und Potenzialfluktuationen ist hinreichend klein; Fluktuationen treten vornehmlich im Bereich des Dichtegradienten auf; die poloidale Phasengeschwindigkeit turbulenter Strukturen weist in Richtung der diamagnetischen Drift der Elektronen.

Das Augenmerk in den Turbulenzuntersuchungen richtet sich auf den Rand des Plasmas innerhalb der Bereichs geschlossener Flussflächen. WEGA kann in zwei unterschiedlichen Betriebsarten arbeiten, die sich in der Induktion des einschließenden Magnetfeldes unterscheiden (57 mT bzw. 500 mT). Die zwei Modi zeigen starke Unterschiede in der Dynamik der Turbulenz. Bei 57 mT zeigen sich Strukturen mit einer poloidalen Ausdehnung die der räumlichen Ausdehnung des Plasmas nahekommt. Bei 500 mT sind die Strukturen deutlich kleiner, wobei die Ausdehnung der Strukturen nahezu proportional zur inversen Induktion ist. Dies legt eine direkte Verbindung der Strukturgröße zur Dispersions-Skalenlänge der Driftwelle, $\rho_s = \sqrt{m_i k_B T_e} / (qB)$, nahe. Gegen diesen Zusammenhang spricht jedoch, dass die Strukturgröße bei einer Variation der Ionenmasse unverändert bleibt. Die poloidale Phasengeschwindigkeit innerhalb des Einschlussbereiches, wo die $\mathbf{E} \times \mathbf{B}$ Drift vernachlässigbar ist, ist in guter Übereinstimmung mit der diamagnetischen Driftgeschwindigkeit der Elektronen. Die Energie im turbulenten Wellenzahl-Frequenzspektrum verteilt sich um die Dispersionsrelation der Driftwelle.

Die dreidimensionale Struktur der Turbulenz wird mit Hilfe entlang einer Feldlinie angeordneter Sonden untersucht. Wie für Driftwellen erwarten zeigt sich eine endliche parallele Wellenzahlkomponente. Das Verhältnis von mittlerer paralleler zu poloidaler Wellenzahl liegt bei $\bar{k}_{\parallel} / \bar{k}_{\theta} \approx 10^{-2}$. Die parallele Geschwindigkeit der Strukturen liegt zwischen der Ionenschall- und der Alfvén-Geschwindigkeit. In der parallelen Dynamik der Turbulenz zeigt sich ein grundlegender Unterschied zwischen den beiden Betriebsarten. Bei 500 mT lassen sich die Strukturen als Überlagerung von Wellenpaketen mit parallelen Wellenfronten beschreiben. Bei 57 mT zeigt das parallele Wellenzahlspektrum eine Verteilung der Energie auf Anteile, die sowohl parallel als auch antiparallel zum magnetischen Feld ausgerichtet sind. In beiden Fällen entstehen die Strukturen vornehmlich auf der Niedrigfeld-Seite des Torus.

Erste Ergebnisse zu einem neuen Gebiet im Bereich der Plasmaturbulenz werden gezeigt: Der Einfluss resonanter Magnetfeldstörungen und damit verbundener magnetischer Inseln auf die Turbulenz. Magnetische Inseln werden mit Hilfe externer Störspulen manipuliert. Es zeigt sich ein deutlicher Einfluss von Störfeldern auf die Turbulenz. Eine ausgeprägte Erhöhung der Fluktuationsamplitude und des damit verbundenen turbulenten Teilchenflusses tritt im Bereich magnetischer Inseln auf.

Abstract

The present work is the first work dealing with turbulence in the WEGA stellarator. The main object of this work is to provide a detailed characterisation of electrostatic turbulence in WEGA and to identify the underlying instability mechanism driving turbulence. The spatio-temporal structure of turbulence is studied using multiple Langmuir probes providing a sufficiently high spatial and temporal resolution.

Turbulence in WEGA is dominated by drift wave dynamics. Evidence for this finding is given by several individual indicators which are typical features of drift waves. The phase shift between density and potential fluctuations is close to zero, fluctuations are mainly driven by the density gradient, and the phase velocity of turbulent structures points in the direction of the electron diamagnetic drift.

The structure of turbulence is studied mainly in the plasma edge region inside the last closed flux surface. WEGA can be operated in two regimes differing in the magnetic field strength by almost one order of magnitude (57 mT and 500 mT, respectively). The two regimes turned out to show a strong difference in the turbulence dynamics. At 57 mT large structures with a poloidal extent comparable to the machine dimensions are observed, whereas at 500 mT turbulent structures are much smaller. The poloidal structure size scales nearly linearly with the inverse magnetic field strength. This scaling may be argued to be related to the drift wave dispersion scale, $\rho_s = \sqrt{m_i k_B T_e / (qB)}$. However, the structure size remains unchanged when the ion mass is changed by using different discharge gases. Inside the last closed flux surface the poloidal $\mathbf{E} \times \mathbf{B}$ drift in WEGA is negligible. The observed phase velocity is in good agreement with the electron diamagnetic drift velocity. The energy in the wavenumber-frequency spectrum is distributed in the vicinity of the drift wave dispersion relation.

The three-dimensional structure is studied in detail using probes which are toroidally separated but aligned along connecting magnetic field lines. As expected for drift waves a small but finite parallel wavenumber is found. The ratio between the average parallel and perpendicular wavenumber is in the order of $\bar{k}_\parallel / \bar{k}_\theta \approx 10^{-2}$. The parallel phase velocity of turbulent structures is in-between the ion sound velocity and the Alfvén velocity. In the parallel dynamics a fundamental difference between the two operational regimes at different magnetic field strength is found. At 500 mT turbulent structures can be described as an interaction of wave contributions with parallel wavefronts. At 57 mT the energy in the parallel wavenumber spectrum is distributed among wavenumber components pointing both parallel and antiparallel to the magnetic field vector. In both cases turbulent structures arise preferably on the low field side of the torus.

Some results on a novel field in plasma turbulence are given, i.e. the study of turbulence as a function of resonant magnetic field perturbations leading to the formation of magnetic islands. Magnetic islands in WEGA can be manipulated by external perturbation coils. A significant influence of field perturbations on the turbulence dynamics is found. A distinct local increase of the fluctuation amplitude and the associated turbulent particle flux is found in the region of magnetic islands.

Contents

1	Introduction	1
2	Theory	7
2.1	Magnetic Confinement	7
2.1.1	Drifts in Magnetised Plasmas	8
2.1.2	Concept of Nested Magnetic Surfaces	9
2.1.3	Confinement Concepts	10
2.1.4	Resonances in the Magnetic Topology	12
2.2	Transport in Plasmas	15
2.2.1	(Neo)Classical Transport	15
2.2.2	Turbulent Transport	16
2.3	Instabilities in Magnetised Plasmas	18
2.3.1	Curvature Driven Instabilities	18
2.3.2	Drift Wave Instability	19
2.4	The Character of Turbulent Fluctuations	22
2.5	Theoretical Modelling of Drift Wave Turbulence	25
3	Data Analysis Methods	27
3.1	Statistical Analysis	27
3.1.1	Distribution Function	27
3.1.2	Statistical Moments	28
3.2	Correlation Function	28
3.3	Fourier Analysis	30
3.3.1	One-Dimensional Fourier Transform	30
3.3.2	Cross Spectrum and Coherence	31
3.3.3	Averaged Cross-Phase	32
3.3.4	Wavenumber-Frequency Spectrum ($\mathbf{k}\nu$ -spectrum)	32
3.3.5	Relation between Correlation Function and Fourier Transform	33
4	Experimental Setup and Diagnostics	35
4.1	The WEGA Stellarator	35
4.2	Magnetic Configuration	37
4.2.1	Error Field Compensation	40
4.3	Langmuir Probes	43
4.3.1	Principle of Operation	43

4.3.2	A brief Summary of Probe Theory	45
4.3.3	Fluctuation Measurements using Langmuir Probes	50
4.4	Diagnostic Setup	51
4.4.1	Poloidal Probe Array	51
4.4.2	Toroidally Resolved Measurements	51
4.4.3	Data Conditioning and Acquisition	53
4.4.4	Reconstruction of Turbulent Structures in the Poloidal Plane	55
4.4.5	Microwave Interferometer	55
4.5	Equilibrium Profiles	56
4.5.1	Magnetron Operation at 57 mT - Low Field	56
4.5.2	Gyrotron Operation at 500 mT - High Field	58
4.5.3	Typical Plasma Parameters	59
5	Characterisation of Fluctuations	61
5.1	Characterisation of Fluctuations in the Temporal Domain	61
5.1.1	Dependence of Fluctuation Properties on the Magnetic Topology	61
5.1.2	Radial Profiles of Fluctuation Amplitude	64
5.1.3	Cross-Phase Spectra	66
5.1.4	A Qualitative Treatment of Turbulent Transport	68
5.1.5	Statistical Properties of Fluctuations	70
5.2	Perpendicular Dynamics of Turbulence in WEGA	74
5.2.1	Turbulent Structures in Raw Data	74
5.2.2	Poloidal-Temporal Correlation Function	74
5.2.3	$k_{\theta}\nu$ -Spectrum	76
5.2.4	Wavenumber Spectrum	77
5.2.5	Poloidal Velocity Profiles	78
5.2.6	Differences in High and Low Field Operation	79
5.2.7	Scaling of Structure Size	81
5.3	Parallel Dynamics of Turbulence	84
5.3.1	Heuristic Model of Three-dimensional Drift-Wave Turbulence	85
5.3.2	Field Line Tracing	88
5.3.3	Results from High Field Operation	91
5.3.4	Results from Low Field Operation	97
5.4	Summary of Major Results	103
5.5	Conclusions and Outlook	105
6	On Magnetic Islands and Turbulence	109
6.1	Motivation	109
6.2	Initial Experimental Results	110
6.2.1	Profile Flattening Caused by Magnetic Islands	112
6.2.2	Impact of Magnetic Islands on Turbulence	113
6.3	Discussion	119
6.4	Outlook	120

Nomenclature

\tilde{x}	fluctuating part of quantity x
a	minor plasma radius
A	probe surface
\mathbf{B}	ambient magnetic field vector
B	modulus of \mathbf{B}
B_0	toroidal field on the magnetic axis
δB	magnetic field perturbation
$c_s \approx \sqrt{T_e/m_i}$	ion sound velocity
d_θ	poloidal correlation length
D	particle diffusion coefficient
$e = 1.602 \cdot 10^{-19}$ As	elementary charge
\mathbf{E}	electric field vector
E	modulus of \mathbf{E}
\mathbf{F}	mechanical force
$\mathbf{F}_L = q\mathbf{v} \times \mathbf{B}$	Lorentz force
I_{cc}	current in error field compensation coil
I_H, I_T	toroidal and helical field coil current, respectively
I_p	probe current
$I_{sat,(e/i)}$	electron/ion saturation current
\mathbf{k}	wavenumber vector
$k_B = 1.381 \cdot 10^{-23}$ J/K	Boltzmann constant
K	kurtosis
l_p	probe length
L_c	parallel connection length between probes
m_j	particle mass of particle species j
n	particle density
$p_j = nk_B T_j$	plasma pressure of particle species j
p_n	neutral gas pressure
q	electric charge
Q	energy flux
r_{eff}	effective radius, flux surface label
r_p	probe radius
$r_{L,j} = m_j v_j / eB$	Larmor radius of species j
R	major torus radius
R_0	major radius of the magnetic axis
\mathbf{R}_C	field line curvature vector
\mathfrak{Re}	Reynolds number
s	magnetic shear
S	skewness
$S(\nu)$	power spectral density
T_j	temperature of particle species j
U_p	probe biasing voltage

\mathbf{v}	velocity vector
v	modulus of \mathbf{v}
$v_A = B/(\mu_0 n m_i)$	Alfvén-velocity
$\mathbf{v}_{dia,j} = -\nabla p_j \times \mathbf{B}/(q n B^2)$	diamagnetic drift velocity of species j
$v_{h,j} = \sqrt{2k_B T_j/m_j}$	thermal velocity
W_H	Hanning windowing function
W_{pl}	total plasma energy
Z	ion charge state
α	ionisation degree
α_{fg}	cross-phase between signals f and g
$\bar{\alpha}$	cross-power weighted average cross-phase
$\beta = 2\mu_0 n k_B T/B^2$	ratio of plasma pressure to magnetic field pressure
γ_{fg}	coherence between signals f and g
Γ	particle flux
δ_θ	poloidal shift of structure with respect to the connecting field line
$\epsilon_0 = 8.854 \cdot 10^{-12} \text{ As/Vm}$	dielectric constant
η	resistivity
θ	poloidal angle coordinate
$t = \iota/2\pi$	rotational transform
λ	wavelength
$\lambda_D = \sqrt{\epsilon_0 k_B T_e / 2 n_e e^2}$	Debye shielding length
λ_e	mean free path of electrons
μ	mean value
$\mu_0 = 4\pi \cdot 10^{-7} \text{ Vs/Am}$	vacuum permeability
ν	frequency
$\nu_b = (m_e R \nu_e)/(m_i c_s t^2)$	ballooning parameter
ν_{jk}	collision frequency between particle species j and k
ν_s	sampling frequency
ρ	mass density
$\rho_s = c_s/\omega_{c,i}$	drift wave dispersion scale
σ	standard deviation
τ_E	energy confinement time
τ_L	average lifetime of turbulent structures
φ	toroidal angle coordinate
Φ	electrostatic potential
Φ_{fl}	floating potential
Φ_{pl}	plasma potential
χ	heat diffusivity
ψ_{fg}	cross correlation function between signals f and g
$\Psi_{fg}(\nu)$	complex cross spectrum between signals f and g
$\omega_{c,j} = qB/m_j$	cyclotron frequency

Chapter 1

Introduction

The phenomenon of turbulence is a feature of fluid motion and is very often referred to as one of the last unsolved problems in classical physics [FS06]. Although turbulence has been studied intensively during the last two centuries, including great physicists and mathematicians like e.g. Heisenberg, Feynman or Kolmogorov, no non-contradictory solution for the problem based on first principles has been found up to now (see e.g. ref. [Sre99] or [Yag01] for a historical review). One fundamental problem in the theoretical understanding of turbulence is the non-integrability of the equations describing the evolution of turbulent system. This means, that with the mathematical procedures available today, no general exact solution is possible.

The present work will understandably not make any attempt to contribute to the general theoretical understanding of turbulence. It presents experimental investigations of one special branch of science, where turbulence plays a crucial role for the solution of a fundamental practical problem: finding a sustainable source of energy for the future generations.

In principle every fluid can become turbulent under certain conditions. The following list shall give a phenomenological description of turbulence in order to find a clear distinction between turbulence and other kinds of fluid motion [TL72]:

- Turbulent flow is highly disordered, i.e. random. Randomness is a necessary but not sufficient criterion for turbulent motion.
- Turbulent flow is highly diffusive, causing rapid mixing and increased rates of momentum, mass and energy transfer among fluid elements.
- Turbulent flow is typically rotational, characterised by a high level of fluctuating vorticity ($\nabla \times \mathbf{v}$, with the flow velocity \mathbf{v}).
- Turbulent flow is strongly dissipative, converting energy of the velocity fluctuations into internal energy. Turbulence would eventually decay, unless provided a source of kinetic energy.
- Turbulent flow contains motions with a wide range of amplitudes, and temporal and spatial scales.

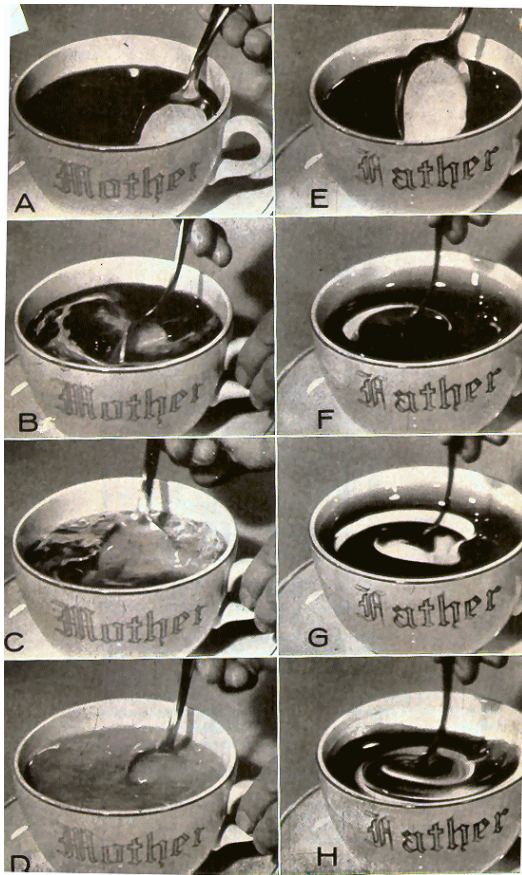


Figure 1.1: Turbulent mixing of two fluids, illustrated by coffee and milk (left). Using a more viscous fluid than milk the mixing is less effective because the flow is laminar (right). (Picture from [Cor61])



Figure 1.2: Snap-shot of a turbulent flow developing from an initial laminar jet flow. The formation of turbulent structures is apparent in the developed turbulence. (Picture from [VD82])

To give a simplified textbook definition, turbulence is a fluid motion involving random macroscopic mixing, with a large range of length and time scales [Rey74].

The phenomenon of turbulence is ubiquitous. An example of the occurrence of turbulence, which is almost too simple to be associated with such a complicated problem, is preparing white coffee. After pouring milk (carefully) locally into the coffee it is sufficient to stir a few times and the milk disperses throughout the entire volume of the cup. The milk picks up velocity by the stirring process. The induced flow will then develop into turbulence. Strands of milk of various sizes move in the coffee; thicker strands become thinner and longer by time, until the coffee is homogeneous. In fig. 1.1 the temporal evolution of this two fluid system is depicted. For comparison the same experiment is also shown with a fluid more viscous than milk. The flow stays laminar and the mixing is weak.

A more general picture of how a turbulent flow appears in space is shown in

fig. 1.2. It shows a snapshot in time of an initial laminar fluid jet developing into turbulence. Swirling flow patterns of various size can be seen. The formation of such patterns, or structures, is a typical feature of turbulence, which is also subject of this work. Being static, however, the picture does not do justice to the dynamical interaction among the constituent scales of the flow. Observations suggest that the patterns get stretched, folded and tilted as they evolve, losing shape by agglomeration or breakup, all in a manner that does not repeat itself in detail [Sre99]. The turbulent system has only a short term memory in the sense of structures rapidly changing their shape and becoming decorrelated. The definition of what constitutes “rapidly” varies from time scales in the order of microseconds (e.g. for phenomena observed in this work) up to several million years in interstellar medium [Bur06]. The snapshot in fig. 1.2 evokes the impression of a high degree of order, which is not present when looking at the fluid velocity as a function of time measured at any point in space. In this case the random character making turbulence a statistical phenomenon manifests itself.

Fig. 1.2 also shows that turbulence develops from an initial laminar flow. The control parameter responsible for the onset of turbulence is the balance between nonlinear and dissipative properties of the flow. Nonlinear interactions produce, if prevailing, finer and finer structures covering a wide range of spatial scales over several orders of magnitude. The wide range of scales involved and the randomness, are what makes turbulence a statistical phenomenon. The theory of turbulence by its nature cannot be other than statistical, i.e., an individual description of the characteristics of turbulent flow is in principle impossible [MY71].

Historically turbulence research originated from studying the behaviour of incompressible fluids, where the general equations of motion applying to laminar as well as turbulent flows (Navier-Stokes equations) were developed by the first half of the 19th century. During the last decades another field of turbulence research has attracted much attention, i.e. plasma turbulence, which leads us to the topic of the present work.

The occurrence of turbulence in plasmas is as ubiquitous as in neutral fluids. However, the dynamics of turbulent plasma flow is far more complicated because plasma can be treated in principle as a charged fluid being subject to electromagnetic forces additional to the viscous forces acting in a neutral as well as in a charged fluid. The study of plasma turbulence is mainly motivated by its relevance in nuclear fusion research. Nuclear fusion refers to thermonuclear reactions converting parts of the mass of the reactants into energy. It was found in the 1930's that nuclear fusion of light nuclei can release energy [Wv35]. Fusion processes have been found to be the source of energy production in stars [Bet39], and thus the fundamental source of life on earth. Nowadays, that mankind's attentions is more and more directed to the sustainment of the sensitive equilibrium of life on earth, nuclear fusion is spotlighted for other reasons. The change of climate on earth caused by human activities is evident [IPC07]. Nuclear fusion is a promising candidate for a sustainable source of energy for future generations.

The idea to construct a reactor producing energy by fusion reactions arose in the

1950's. In contrast to the energy production of stars relying on proton-proton interactions, terrestrial fusion research depends upon hydrogen isotopes that are more reactive [HM92]. Deuterium-tritium (D-T) reactions are emphasised due to their relatively favourable cross section. However, the optimum operating temperature for a (D-T) reactor is in the order of $T \approx 10^8 \text{ K} \hat{=} 10 \text{ keV}$ ¹. At these temperatures the reactor fuel is in the state of a fully ionised plasma.

The goal of nuclear fusion research is to construct a reactor containing a steady-state, self-sustained plasma, maintaining its high temperature against energy losses solely from heating by the energy from fusion reactions. The fundamental demand to reach this state has been derived by Lawson [Law55]. Roughly speaking, a sufficiently dense plasma at optimum temperature has to be confined in a closed boundary for a time, long enough to ensure a sufficiently high probability for fusion reactions. The characteristic time under consideration is called energy confinement time τ_E being defined by the ratio of total plasma energy W_{pl} and power input P_{in} :

$$\tau_E = \frac{W_{pl}}{P_{in}}. \quad (1.1)$$

Lawson's criterion states that the product of particle density n and confinement time τ_E in a fusion reactor must equal or exceed a critical value to reach the aspired plasma state:

$$n\tau_E \gtrsim 5 \cdot 10^{20} \text{ s/m}^3 \quad (1.2)$$

for the important case of D-T reactions at the optimum temperature of $T_e \approx 10 \text{ keV}$.

Plasma confinement can be realised by applying magnetic fields to the plasma relying on the Lorentz force acting on the charged plasma particles, thus building up a magnetic cage for the plasma. However, confining a plasma under thermonuclear conditions is such a striking challenge, that the Lawson criterion has not been reached in any experimental fusion device up to now, more than fifty years after its derivation. Plasma confinement is always imperfect. Dissipation induced by Coulomb-collisional scattering provides an irreducible minimum of energy and particle loss from the containment volume [HH76]. However, it has been found already in the early days of fusion research that the losses are of orders of magnitude higher than the collisional minimum. The reason for this enhanced loss is not yet fully understood. But it is well known that it is mainly due to turbulent plasma flow triggered by fluid instabilities.

The detailed understanding of plasma turbulence is therefore a key issue on the way to an energy producing fusion reactor. The present work addresses the problem from the experimental point of view. The experimental framework, i.e. the WEGA stellarator allows a deep insight into the spatio-temporal structure of turbulence, which is typically not given in fusion devices.

¹In plasma physics it is customary to give temperatures in units of energy corresponding to $k_B T$, where $k_B = 1.38 \cdot 10^{-23} \text{ J/K}$ is Boltzmann's constant. The plasma temperature is closely related to the average kinetic energy of the species under consideration, but not equal [Che84].

Outline

Subsequently, the thesis is structured as follows: In chapter 2 the theoretical framework, which is necessary to understand the experimental results and their interpretation is given. The fundamentals of magnetic confinement and the technical implementations of the concepts will be introduced. Instabilities leading to a turbulent plasma behaviour will be explained concentrating on types of instabilities which are probably most relevant for this work. Some basics on the nature of turbulence will be explained followed by a brief history of the theoretical understanding of plasma turbulence.

In chapter 3 the mathematical methods used to approach the statistical phenomenon of turbulence are introduced. These are mainly correlation and spectral analysis techniques.

In chapter 4 the experimental framework for this work, i.e. the WEGA stellarator is introduced. The description includes the machine setup, the magnetic field configuration as well as typical equilibrium plasma conditions under which turbulence is studied. Since all measurements in this work rely on electrostatic probes (Langmuir probes), their functionality will be explained, highlighting aspects being relevant for this work. The presented diagnostic setup has been developed within this work for spatio-temporally resolved fluctuation measurements.

The following chapter 5 addresses the major experimental results, characterising the spatio-temporal structure of turbulence in WEGA under various boundary conditions. Starting from relatively simple local measurements with single probes, the perspective will be expanded upon, concluding with an deep insight into the three-dimensional structure of turbulence.

Chapter 6 will present some initial results on a new aspect of plasma turbulence, which has not been investigated in other experiments before in this way, i.e. the influence of resonant magnetic field perturbations on turbulence.

Chapter 2

Theory

2.1 Magnetic Confinement

Every charged particle moving in a magnetic field \mathbf{B} is subject to the Lorentz force acting perpendicular to \mathbf{B} and the particle velocity \mathbf{v} :

$$\mathbf{F}_L = q\mathbf{v} \times \mathbf{B}. \quad (2.1)$$

In a plasma, particles of a species j with a temperature T_j and a mass m_j move on average with the thermal velocity $v_{th,j} = \sqrt{2k_B T_j / m_j}$ [Che84]. The velocity component parallel to the magnetic field is unaffected by the Lorentz force. In the plane perpendicular to \mathbf{B} the Lorentz force \mathbf{F}_L causes the particles to gyrate around a field line with a frequency $\omega_{c,j}$ (*gyro* frequency or *cyclotron* frequency) and an average radius $r_{L,j}$ (*gyro* radius or *Larmor* radius).

$$\omega_{c,j} = \frac{qB}{m_j} \quad \text{and} \quad r_{L,j} = \frac{\sqrt{2m_j k_B T_j}}{qB} \quad (2.2)$$

The particle orbit resulting from the free parallel motion and the gyration is a helical path along the field lines. The centre of this helical orbit is called *guiding centre*. Hence, with an appropriate geometry it is possible to confine a plasma in a magnetic field. The most simple geometry is a cylinder with magnetic field lines along the cylinder axis. Achieving nuclear fusion in a linear magnetic field is not feasible as it is practically impossible to reach the Lawson criterion. Particles moving along the cylinder axis with v_{th} reach the endplates after a time of $\tau = L/v_{th}$, where L is the length of the cylinder. To reach the Lawson criterion, L would have to be in the order of 10^6 m. A practical approach to overcome the end plate problem is to bend the plasma to a torus. In a toroidal plasma the field lines are closing upon themselves, hence no end plate losses occur. The geometry of a toroidal magnetic field is depicted in fig. 2.1.1. The torus axis pointing in vertical direction is encircled by the toroidal angle coordinate φ . The major radius R measures the distance from the torus axis. The poloidal angle θ encircles the so called magnetic axis, which itself has a major radius of R_0 . The minor radius r measures the distance from the magnetic axis.

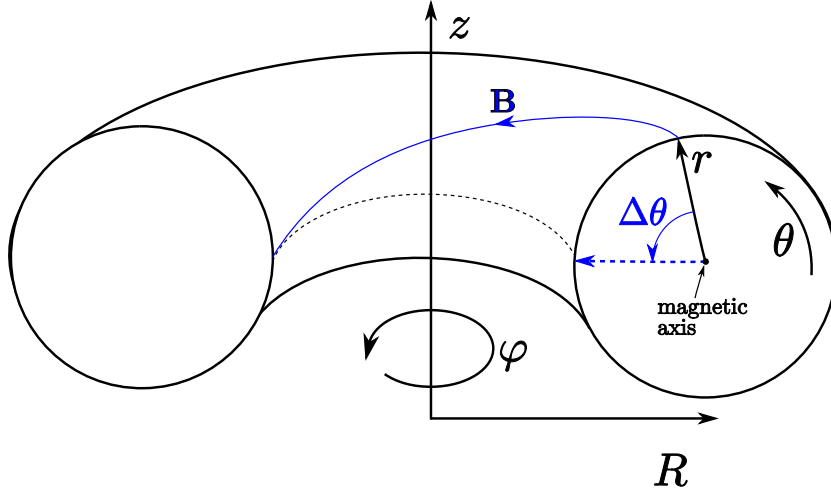


Figure 2.1.1: Sketch of a simple (half) torus, illustrating the general geometric topology. In blue a helical field line with a finite rotational transform ι is indicated.

2.1.1 Drifts in Magnetised Plasmas

Any force \mathbf{F} acting on a charged particle in a magnetic field gives rise to a drift velocity which can be described by:

$$\mathbf{v}_d = \frac{\mathbf{F} \times \mathbf{B}}{qB^2}. \quad (2.3)$$

In a toroidal magnetic field two forces are important, inertia caused by the field line curvature and a force caused by the field inhomogeneity ($\nabla\mathbf{B}$ -force). In sum they cause the so-called torus drift:

$$\mathbf{v}_{tor} = \left(v_{\parallel}^2 + \frac{1}{2}v_{\perp}^2 \right) \frac{m}{qRB^2} \mathbf{R}_C \times \mathbf{B}, \quad (2.4)$$

where \mathbf{R}_C is the field line curvature largely equivalent to the major radius of the torus. v_{\parallel} and v_{\perp} are the particle velocity components parallel and perpendicular to \mathbf{B} , respectively. v_{tor} points in vertical direction and leads to a charge separation because its sign is opposite for electrons and ions. A further drift, being independent of the charge is the $\mathbf{E} \times \mathbf{B}$ drift related to the electric force $\mathbf{F} = q\mathbf{E}$:

$$\mathbf{v}_{\mathbf{E} \times \mathbf{B}} = \frac{\mathbf{E} \times \mathbf{B}}{B^2}. \quad (2.5)$$

The charge separation caused by the torus drift induces a vertical electric field E_z giving rise to an $\mathbf{E} \times \mathbf{B}$ drift pointing radially outwards for both, ions and electrons. Therefore, the whole plasma in a pure toroidal magnetic field drifts radially outwards towards the vessel walls.

The drifts explained so far can be derived from a single particle description of the plasma. A further drift which is important in the understanding of the results

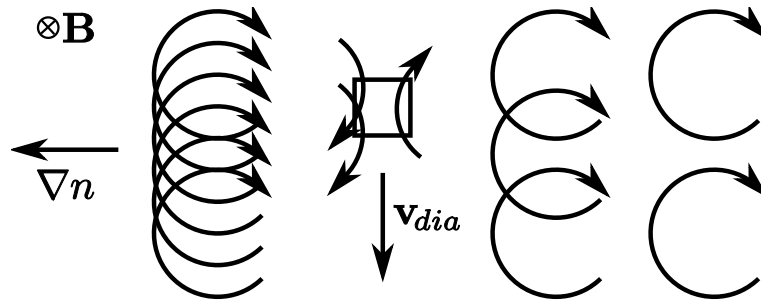


Figure 2.1.2: Origin of the diamagnetic drift for magnetised electrons in a density gradient. The magnetic field points into the drawing plane. The density gradient points to the left, indicated by the higher density of gyrating electrons (circles) on the l.h.s.

presented in this work, and for the stability of the plasma is the so called diamagnetic drift. The physical reason for the diamagnetic drift can only be explained in the fluid description of the plasma since it is not a single particle drift. Fig. 2.1.2 depicts its origin. Here, the orbits of gyrating electrons in a magnetic field with a density gradient pointing to the left are shown. More particles can be found in the same volume element at higher density. Through any fixed volume element there are more electrons moving downward than upward, since the downward-moving electrons come from a region of higher density. Therefore, there is a fluid drift perpendicular to ∇n and \mathbf{B} , even though the guiding centres are stationary [Che84]. The resulting drift velocity is given by:

$$\mathbf{v}_{dia,j} = -\frac{\nabla p \times \mathbf{B}}{qnB^2}, \quad (2.6)$$

where $p_j = nk_B T_j$ is the plasma pressure of the particle species j and n is the corresponding particle density, being equal for electrons and ions due to quasineutrality of the plasma (assuming singly charged particles). In a toroidal plasma with a density gradient pointing along the minor radius \mathbf{v}_{dia} points in poloidal direction and leads to a poloidal rotation of the plasma column.

2.1.2 Concept of Nested Magnetic Surfaces

As shown above a pure toroidal magnetic field is not able to provide a plasma confinement necessary for nuclear fusion. A way to solve the problem of the radial $\mathbf{E} \times \mathbf{B}$ drift is to superimpose a poloidal magnetic field component B_θ bending the toroidal field lines into helical windings around the torus. By doing this, the upper and lower parts of the torus are connected by field lines and hence, the vertical polarisation induced by the torus drift is short circuited by the high parallel conductivity of the plasma. No net radial drift occurs and the plasma is confined. The field line pitch is characterised by the so-called *rotational transform* t . Along a toroidal angle of $\Delta\varphi$ a helical field line passes a poloidal angle of $\Delta\theta$ as indicated in

fig. 2.1.1. t is defined as the poloidal angle displacement per toroidal turn ($\Delta\varphi = 2\pi$) [Wes97]:

$$t = \frac{\Delta\theta}{2\pi}. \quad (2.7)$$

t can be calculated from the ratio of poloidal and toroidal field component:

$$t(r) = \frac{R_0 B_\theta}{r B_\varphi}, \quad (2.8)$$

and is in general not constant along the minor radius r of the torus. The radial variation of t is characterised by the magnetic shear:

$$s = -\frac{r}{t} \frac{\partial t}{\partial r}. \quad (2.9)$$

In the general case of irrational values of t the field line will never close and span up a closed area which is then called a closed *flux surface*. For $t = 1$ a field line returns to its starting point after one toroidal turn. For any rational value of $t = m/n$, where m and n are integers, the field line closes upon itself after m toroidal and n poloidal turns. A flux surface at rational values of t cannot be described by a single field line, but only by an infinite number of closed field lines.

Since plasma particles can (ideally) move freely along a field line they will be confined on a flux surface infinitely long if no cross field transport mechanism causes them to leave the flux surface¹. When considering plasma equilibrium theoretically, one can show, that flux surfaces are isobars for the plasma [HM92]. A confining cage for the plasma can be formed by producing a magnetic field configuration which is build up of a set of nested closed flux surfaces. In the centre of the flux surfaces there exists one single field line that closes after a single toroidal turn. This line is called the magnetic axis.

2.1.3 Confinement Concepts

From the experimental point of view two major technical concepts to confine a plasma magnetically have been successfully developed in the past decades of fusion research. The major difference between these two types of experiments is the way the poloidal field component is produced.

The Tokamak

The *tokamak* was developed in the Soviet Union following the theoretical ideas of Tamm and Sakharov for a thermonuclear reactor [TS61]. In a tokamak the toroidal magnetic field is produced by a set of coils wound poloidally around the torus. The poloidal magnetic field is generated by a toroidal current in the plasma. This current is usually generated by induction, where the plasma simply acts as the secondary

¹The effect of transport perpendicular to \mathbf{B} is discussed in section 2.2.

winding of a transformer. The technical concept of a tokamak is relatively simple. The magnetic field topology of tokamaks is axially symmetric, implying that it does not change in toroidal direction. Therefore, it has an intrinsically two-dimensional character. Although tokamaks have reached a state of development which is relatively close to the demands of nuclear fusion [KHP99], the drawback of the tokamak is that driving the plasma current is a challenge in steady state operation. Tokamaks with inductively driven plasma current can in principle only operate in a pulsed mode. Steady state current drive is possible in principle, e.g. by generating a net parallel momentum by injecting energetic particles or electromagnetic waves into the plasma [Fis78]. However, this technique is not yet satisfactorily established.

The Stellarator

A concept for magnetic confinement without the need of a net toroidal plasma current is the *stellarator* [SJ58]. In a stellarator the twist of field lines is produced by external coils only, giving the stellarator the intrinsic capability of steady state operation. The price one has to pay for this advantage is that stellarators sacrifice the toroidal symmetry of a tokamak. Stellarators are fully three-dimensional plasma confinement devices. The rotational transform in a stellarator can be achieved in several ways [Boo98]. One way is to bend the magnetic axis as in the first stellarators following the figure-eight concept proposed by Spitzer [SJ58]. Another method is to provide a set of coils winding helically around the torus as shown in fig. 2.1.3. This is the so called *classical stellarator* concept as it has been realised in the WEGA stellarator. Thinking of a linear stellarator, the helical field coils produce an additional transverse multipolar field with a helical symmetry. The magnetic field for a given radius is a periodic function of $\theta' = l(\theta - 2\pi z/h)$, where l is half the number of helical multipole conductors, z is the axial coordinate and h is the pitch length of the helical windings. Bending the linear stellarator to a torus, the periodicity becomes: $l\theta - m\varphi$, where m is the toroidal periodicity given by $2\pi Rl/h$. In this case the helical symmetry is destroyed by the toroidicity and the configuration becomes three-dimensional. The number of coil pairs l is the crucial factor for the shape of a flux surface in the poloidal plane. $l = 2$ leads to a quasi elliptical shape, $l = 3$ to a triangular shape.

Due to the assumptions of flux surfaces as being isobars and the 3D magnetic geometry it is advantageous to redefine the toroidal coordinate system (r, φ, θ) into a coordinate system which is based on the flux surface topology. Every flux surface is given a label r_{eff} describing the radius of a circle covering the same area in the $r - \theta$ -plane as the flux surface under consideration. A toroidal circuit is any loop that encircles the torus axis. A poloidal loop encircles the magnetic axis. Surfaces on which $r_{eff}(\mathbf{r})$ is constant define a set of nested tori, the flux surfaces. The magnetic axis is a toroidal circuit with $r_{eff} = 0$.

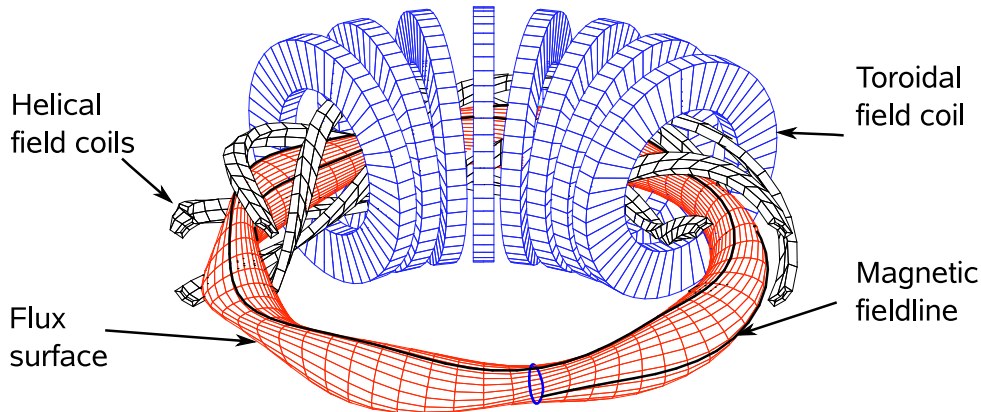


Figure 2.1.3: Conceptual sketch of a classical stellarator. The toroidal and the poloidal field components are produced by individual coil sets. The poloidal field originates from helical windings, resulting in non-axisymmetric flux surfaces (red). The field topology is periodic in toroidal direction. The periodicity is determined by the number of turns of the helical field coils. (Adapted from [Wob99])

2.1.4 Resonances in the Magnetic Topology

The structure of magnetic fields is described mathematically by nonlinear differential equations with coefficients varying periodically along the torus (see ref. [MS66]). Due to the periodicity of the magnetic field in a toroidal confinement system, it can be described by a discrete Fourier series as a function of the toroidal and the poloidal angle coordinate:

$$B_j(r_{eff}) = \sum_{m,n} (B_{j,0}^s(r_{eff}) \sin(n\theta + m\phi) + B_{j,0}^c(r_{eff}) \cos(n\theta + m\phi)), \quad (2.10)$$

where the integers m and n are the toroidal and poloidal periodicity of each Fourier component, respectively, and j represent the components of the field vector. A decisive role for the magnetic field structure is given to the so called resonant surfaces where the rotational transform is a rational value, $t = m/n$. A perturbation being in resonance with rational surfaces may lead to a strong influence on the magnetic field lines. The problem has been analysed in detail by Rosenbluth et al. [Ros+66] and is explained in the following without going into the mathematical details. Any perturbation field δB can be described in a similar way as eqn. (2.10). A radial component of the perturbation leads to a deviation of field lines from a given flux surface. This deviation may have strong effects if the periodicity of the perturbation (m, n) is in resonance with the periodicity of the unperturbed field line on a flux surface, hence it has the same rotational transform, $t = m/n$. For irrational t the perturbation vanishes on average along the path of the field line on the flux surface. For closed field lines on rational surfaces the initially small perturbation is amplified due to the resonance with the perturbation. The geometry of the change in the magnetic topology arising from resonant perturbations can be calculated by

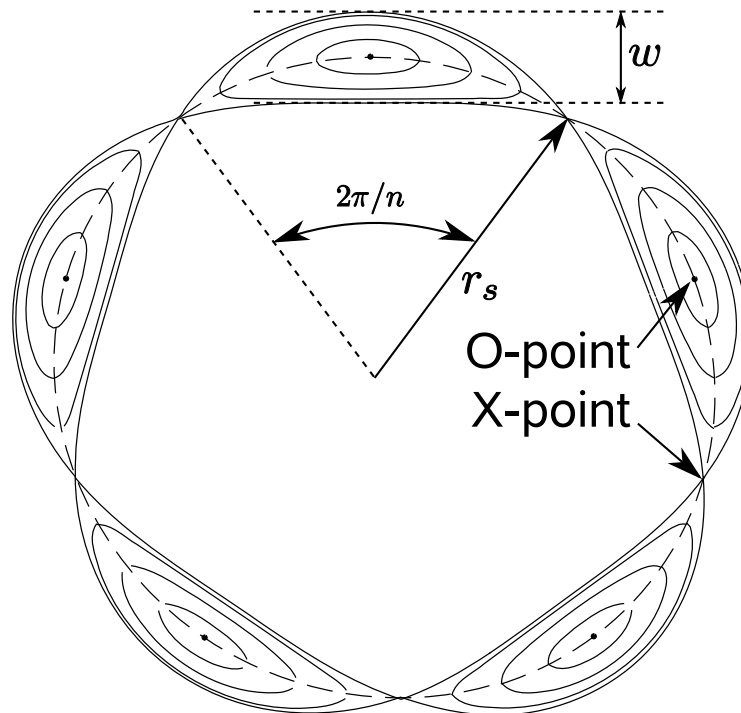


Figure 2.1.4: Geometry of the magnetic field lines in a $n = 5$ island in the $r - \theta$ -plane according to eqn. (2.12). The island chain is typically surrounded by undisturbed closed flux surfaces.

determining the trajectory of the magnetic field line. The field perturbation may be taken to have the form:

$$\delta B_r = \delta \hat{B}_r(r) \sin n\chi, \quad (2.11)$$

with $\chi = \theta - \frac{m}{n}\varphi$ and $\delta \hat{B}_r(r)$ being the amplitude of the perturbation field. If $\delta \hat{B}_r(r)$ is essentially constant over the radius, the radial deviation Δr of the field line from the unperturbed flux surface is given by [Wes97]:

$$\Delta r^2 = \frac{w^2}{8} (\cos n\chi - \cos n\chi_0) \quad (2.12)$$

The result is a so called magnetic island structure, as shown in fig. 2.1.4. w is the radial width of the island and χ_0 is the point where the field line under consideration crosses the unperturbed resonant surface ($\Delta r = 0$). The magnetic field lines within the island lie on a set of nested helical flux surfaces with their own magnetic axis, the field line describing the O-point. The poloidal distance between two X-points corresponds to the poloidal wavelength of the perturbation, $\Delta\theta = 2\pi/n$. The O-point of the island strictly reflects the point where the perturbation vanishes and the field line closes upon itself after n toroidal turns. Every helical flux surface within the island can be described by a single field line.

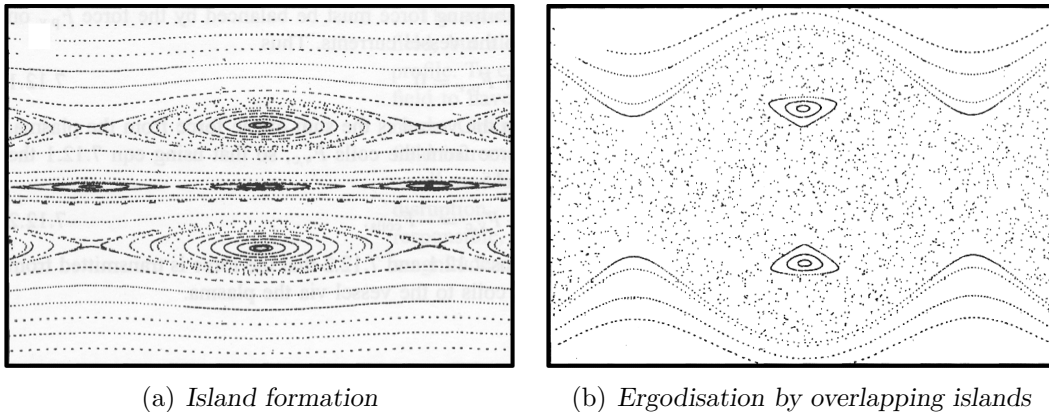


Figure 2.1.5: Magnetic field topology in case of a sheared magnetic field with neighbouring resonant surfaces. At small perturbing magnetic field the islands are separated from each other (a). With increasing magnitude of the perturbation the islands will start overlapping resulting in ergodic field lines (b). (Picture from [Wes97])

The radial width of an island is given by [Bic97]:

$$w_{mn} = 4 \left| \frac{\delta B_{mn} R}{n B dt/dr} \right|^{1/2}. \quad (2.13)$$

w is proportional to the square root of the relative perturbation $\delta B/B$ and decreases with increasing order n of the resonance. The dependence of w on dt/dr shows that magnetic shear helps reducing the island width by restricting the perturbation to a smaller radial region.

A sheared t profile is a prerequisite for the formation of islands in general. Only if t changes with the radius, i.e. the magnetic field is sheared, the resonant surface is radially localised. If there is no magnetic shear, then a perturbation being resonant with the now constant t may completely destroy the magnetic surfaces [Ker62]. In the spectrum of a perturbation field in a sheared magnetic field different islands may develop independently at the corresponding resonant surface, as shown in fig. 2.1.5 (a). With increasing field perturbation neighbouring islands will overlap. In this case field lines may jump from one island to the next and a Brownian motion of field lines occurs, leading to the destruction of flux surfaces. Fig. 2.1.5 (b) shows an example for field line ergodisation in case of overlapping resonances.

The formation of islands and ergodic regions is an important issue for plasma confinement since plasma losses can be severely enhanced by these phenomena. Islands and ergodic regions represent a radial short circuit for the plasma. Inner and outer boundaries are connected by field lines on which particles can propagate almost freely. A strong dependence of confinement on the rotational transform has already been found in early stellarator experiments (Wendelstein 2B) [Gri+71], with a deterioration of confinement at low order rational values of t ($1/2$ or $1/3$). Similar results have been obtained at the Wendelstein 7A stellarator [Cat+85], where it

could be shown, that the decreased confinement was due to the effect of magnetic surface destruction at resonances [WF88].

Field perturbations may arise from any irregularities of magnetic coils, being periodic along the torus. In tokamaks an additional source of field perturbations are instabilities driven by the plasma current. In stellarators islands are an inherent consequence of the lack of continuous symmetry. A stellarator which has m toroidal field periods may be considered as a helical symmetric configuration perturbed by a m -period perturbation [Wob94]. The corresponding islands are called natural islands. They are usually rather small because of the $m^{-1/2}$ dependence of the island width. Most dangerous for plasma confinement are perturbations breaking the m -fold toroidal symmetry of the stellarator. These may be caused, e.g. by errors in the coil positioning or asymmetries induced by current leads.

2.2 Transport in Plasmas

The Lawson criterion includes a characteristic time scale τ_E , which denotes the energy confinement of a fusion device. τ_E is the limiting factor in the balance of density, temperature and confinement time on the way to an energy producing fusion reactor. Although toroidal devices with nested flux surfaces provide confinement for the plasma, transport processes perpendicular to the flux surfaces lead to a loss of particles and energy from the confinement zone. The understanding of these transport processes is a prerequisite to building a fusion reactor.

2.2.1 (Neo)Classical Transport

The classical approach to describe energy transport in a magnetised plasma perpendicular to the magnetic field is a diffusion process:

$$Q_r = -\lambda \cdot \nabla p = -n\chi k_B \nabla T - k_B T \underbrace{D \nabla n}_{-\Gamma_r}, \quad (2.14)$$

where Q_r is the radial energy flux and λ is a constant of proportionality. The first term on the r.h.s. of eqn. (2.14) is of conductive nature with χ being the heat diffusivity. The second term is of convective nature. It includes the diffusive particle flux $\Gamma_r = -D \nabla n$, where D is the particle diffusion coefficient. χ as well as D are in the so called classical theory caused by collisions in a homogeneous magnetic field and can be interpreted as step size squared times collision frequency in a random walk process. The step size for each collision is in the classical theory given by the Larmor radius of the colliding particles. Since Larmor radius as well as collision frequency are different for different particle species, the diffusion coefficients also have to be treated separately for electrons and ions. A detailed treatment of classical plasma transport can be found in several textbooks, e.g. by Chen [Che84] or Wesson [Wes97]. Experimentally observed diffusion coefficients are in general much larger than predictions from classical theory by 3 to 5 orders of magnitude. A better description of experimental results is obtained when effects arising from the toroidal

geometry are considered in the collisional transport description. This leads to the so called neoclassical theory [GS79] which predicts a strongly increased diffusivity compared to the classical theory. For a review of collisional cross field transport see ref. [Wag94]. Neoclassical theory has been found to match experimentally observed diffusion coefficients in the core of plasmas in optimised confinement regimes [Bra+97]. But it generally fails in the plasma edge region.

2.2.2 Turbulent Transport

The above mentioned mismatch between classical predictions and experimental observations of plasma diffusivity has been known for several decades now. Bohm suggested, that transport caused by broad band plasma oscillations might be responsible for this enhanced transport [Boh49b]. The poor confinement in early stellarator experiments has also already been addressed to a kind of plasma turbulence [Coo61]. Nowadays it is widely accepted, that cross field plasma transport in the edge region of magnetically confined plasmas is mainly caused by turbulent fluctuations of plasma parameters [Woo+90; End99; CA05]. The following section will give a basic explanation of how fluctuations may cause cross field transport of particles and energy in a magnetised plasma.

Some of the terminology has to be clarified beforehand. What is of interest in terms of confinement is not transport perpendicular to \mathbf{B} in general but only the radial component pointing perpendicular to a flux surface. Hence, only the radial component of transport will be treated. A further note is related to the definition of a fluctuating quantity. For parameters $x(t)$ which can be measured directly, the fluctuating part $\tilde{x}(t)$ is what remains of the signal after subtracting its mean value. Hence by definition the fluctuating part of measured plasma parameters like density or potential, has a mean value of zero. This is different for derived quantities like the time dependent transport caused by fluctuating plasma parameters. They may have a finite mean value, as will be shown in the following, but are still called fluctuating quantities in order to discriminate them from parameters derived from stationary plasma parameters. The transport equations presented follow the formulation given by Ross [Ros92].

The diffusive approach to describe the particle flux Γ is extended by a purely convective term:

$$\Gamma_r = -D\nabla n + nv_r, \quad (2.15)$$

where v_r is a radial flow velocity of particles which may be caused by fluctuations. Turbulent flux is in general of convective nature and can be described by

$$\tilde{\Gamma}_r = \tilde{n}\tilde{v}_r + (n\tilde{v}_r + \tilde{n}v_r), \quad (2.16)$$

where only the first term on the r.h.s. can contribute to a net transport as will be shown later. \tilde{v}_r can be caused by two classes of fluctuations: fluctuating electric fields that do not perturb the magnetic configuration (*electrostatic turbulence*), or fluctuating magnetic field perpendicular to a flux surface (*magnetic turbulence*).

In the case of magnetic turbulence transport is caused by a stochastic radial displacement of magnetic field lines in conjunction with the high parallel mobility of electrons [Bic97]. \tilde{v}_r caused by a fluctuating radial magnetic field \tilde{B}_r is given by [Lie85]:

$$\tilde{v}_{r,mag} = v_{\parallel} \frac{\tilde{B}_r}{B_{\varphi}}. \quad (2.17)$$

Due to the high parallel mobility of particles already small relative fluctuation amplitudes may lead to a significant radial transport. A ratio of $\tilde{B}_r/B_{\varphi} \approx 10^{-3}$ is sufficient to explain experimentally observed electron heat fluxes [WS93]. However experiments show, that magnetic fluctuations may contribute significantly to the observed transport in reversed field pinches. But in stellarators and tokamaks the experimentally observed transport can be well explained by electrostatic fluctuations [WTP92; Fik+96]. Electrostatic turbulence can cause radial flows by $\mathbf{E} \times \mathbf{B}$ -drift. A poloidal electric field leads to a radial $\mathbf{E} \times \mathbf{B}$ velocity:

$$\tilde{v}_{r,el} = \frac{\tilde{E}_{\theta}}{B} = \frac{\nabla_{\theta} \tilde{\Phi}}{B}. \quad (2.18)$$

The subscript (*el*) standing for electrostatic will be omitted subsequently, because magnetic fluctuations will not be considered in this work.

Net radial transport is determined from an averaging over eqn. (2.16):

$$\Gamma_r = \langle \tilde{\Gamma}_r \rangle = \langle \tilde{n} \tilde{v}_r \rangle = \frac{\langle \tilde{n} \nabla_{\theta} \tilde{\Phi} \rangle}{B}. \quad (2.19)$$

Only the bi-linear combination of fluctuating quantities may lead to a net transport because the relation $\langle x \tilde{y} \rangle = x \langle \tilde{y} \rangle = 0$ makes the second and third term on the r.h.s. of eqn. (2.16) vanish. Non vanishing average flux is only possible if both, density and potential fluctuations are present. Using spectral techniques (see section 3.3 for details) it is possible to describe the contribution of individual frequency components to the total transport [Pow74]:

$$\Gamma_r(\nu) \propto \gamma_{n\Phi}(\nu) \sin \alpha_{n\Phi}(\nu) \sqrt{S_n(\nu) S_{\Phi}(\nu)}. \quad (2.20)$$

$\Gamma_r(\nu)$ is the fraction of transport carried by the frequency component ν in the spectrum, $\gamma_{n\Phi}(\nu)$ is the coherence between density and potential fluctuations, $\alpha_{n\Phi}(\nu)$ is the cross phase and $S_{n/\Phi}(\nu)$ is the spectral power of density and potential, respectively. Eqn. (2.20) shows that besides the fluctuation amplitude the phase relation between density and potential is important for the transport and both signals must show a phase coherence. Maximum transport is obtained if \tilde{n} and $\tilde{\Phi}$ are fully coherent ($\gamma_{n\Phi} = 1$) and phase shifted by $\alpha = \pi/2$.

Similar transport equations can be derived for the energy transport \tilde{Q}_r :

$$\tilde{Q}_r = \frac{3}{2} \frac{\langle \tilde{E}_{\theta} \tilde{p} \rangle}{B}. \quad (2.21)$$

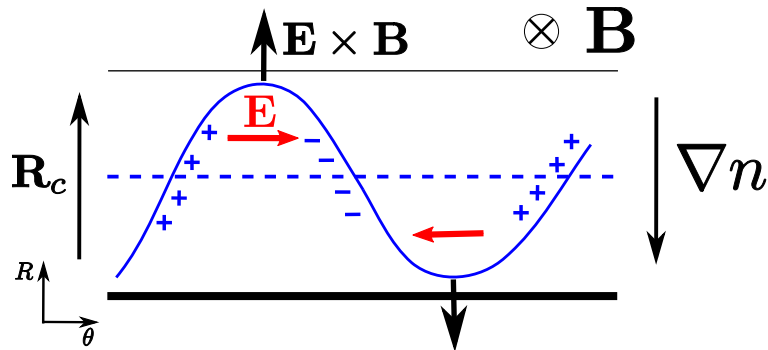


Figure 2.3.1: Physical mechanism of a curvature driven instability in the region of unfavourable curvature. A density perturbation, indicated as a ripple on an isobar in blue, leads to a charge separation by the curvature drift. The resulting $\mathbf{E} \times \mathbf{B}$ drift amplifies the initial density perturbation in the case of unfavourable magnetic curvature.

Temperature fluctuations lead to additional terms besides a convective turbulent energy transport $\tilde{Q}_{r,conv} = T\tilde{\Gamma}_r$, what makes the situation more complex. The role of temperature fluctuations for \tilde{Q}_r is not clear and is discussed in the literature [Pfe+98; Sch05].

2.3 Instabilities in Magnetised Plasmas

The following section will be used to explain the basic physical mechanisms of instabilities in magnetised plasmas. The description is constricted to those instabilities driven by the pressure gradient.

2.3.1 Curvature Driven Instabilities

In fluid dynamics the Rayleigh-Taylor instability occurs when a dense fluid is stratified on top of a less dense fluid under the influence of a gravitational force. An analogon is found in curved magnetic fields with a pressure gradient [KSH78]. The curvature drift takes the place of the gravitational force:

$$\mathbf{F}_c = mv_{\parallel}^2 \frac{\mathbf{R}_c}{R_c^2}, \quad (2.22)$$

where \mathbf{R}_c is the curvature radius of the magnetic field lines. \mathbf{F}_c results in a charge separating drift velocity $\mathbf{v}_c = \mathbf{F}_c \times \mathbf{B}/qB^2$ if isolines are disturbed by e.g. a density ripple as indicated in fig. 2.3.1, where the physical mechanism of a curvature driven instability is depicted. The charge separation leads to an electric field perturbation which is in phase with the initial density perturbation and thus to an $\mathbf{E} \times \mathbf{B}$ -drift. The direction of the curvature vector with respect to the density gradient

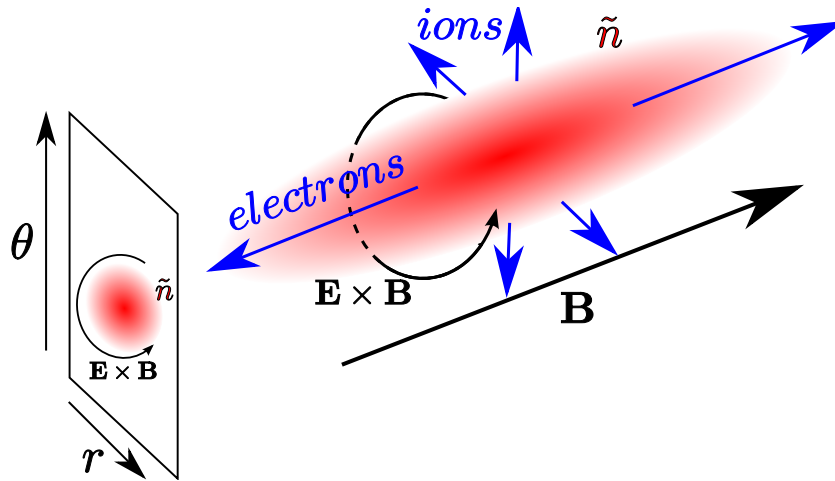


Figure 2.3.2: Plasma response on an initial density perturbation (red blob) in a 3D picture. Electrons stream away from the initial density perturbation parallel to \mathbf{B} due to their high mobility. The lack of electrons gives rise to $\mathbf{E} \times \mathbf{B}$ drift in the $r - \theta$ -plane followed by the polarisation drift of the ions. (Picture adapted from [Sco00])

now determines whether the initial density perturbation is damped or grows. If ∇n and \mathbf{R}_c are parallel, the initial perturbation is damped and the system is stable. This situation is called *favourable magnetic curvature*. Antiparallel gradient and curvature lead to an amplification and thus to an unstable system, what is then called *unfavourable magnetic curvature*. In a toroidal plasma the density gradient typically points to the minor axis of the torus. The high and low field sides of the torus are therefore regions of favourable and unfavourable curvature, respectively. Curvature driven instabilities are in principle two-dimensional phenomena, since no parallel dynamics is involved in the physical mechanism ($k_{\parallel} = 0$). However, in toroidal plasmas this is not generally the case, because regions of favourable and unfavourable curvature are connected parallel to \mathbf{B} by the helical nature of the field lines. In this case parallel dynamics may become important and the instability gets a three-dimensional character ($k_{\parallel} \neq 0$).

2.3.2 Drift Wave Instability

Another more universal instability is the drift wave instability which can occur in any magnetised plasma with a density gradient. Drift waves are an inherently three-dimensional phenomenon because the physical mechanism is based on a strong coupling between dynamics parallel and perpendicular to the magnetic field vector. Fig. 2.3.2 depicts how a drift wave arises from an initial density perturbation. A local density perturbation leads to a density gradient in all three dimensions. Due to their high mobility parallel to \mathbf{B} the electrons react on the perturbation by streaming away with their thermal velocity. The resulting lack of electrons induces a potential

perturbation with a gradient in all three dimensions. The potential perturbation is in case of adiabatic electrons in phase with the density perturbation. Consequentially an electric field arises around the perturbation which leads to a circular $\mathbf{E} \times \mathbf{B}$ drift. Together with the potential perturbation arising in time, another drift comes into play, keeping the system quasineutral and the current divergence free. The polarisation drift acts on the ions in the $r - \theta$ plane.

$$\mathbf{v}_p = \frac{1}{\omega_c B} \frac{d\mathbf{E}}{dt} \quad (2.23)$$

The combination of $\mathbf{E} \times \mathbf{B}$ and polarisation drift leads to a spiral path of the ions away from the perturbation. The polarisation drift amounts to a perpendicular current which has a divergence. This divergence matches that in the parallel current, so that in balance the electrostatic potential evolves according to [Sco00]

$$\nabla \mathbf{J} = \nabla \mathbf{J}_\perp + \nabla \mathbf{J}_\parallel = 0, \quad (2.24)$$

with $\mathbf{J}_\perp = ne\mathbf{v}_p$ and $\mathbf{J}_\parallel \approx nev_{th,e}$. When the parallel ion dynamics is additionally taken into account, the bulk density perturbation propagates in parallel direction with the ion sound velocity $c_s = \sqrt{T_e/m_i}$. In a homogeneous plasma the system develops into a parallel ion acoustic wave. An additional cross field density gradient is what forms a drift wave propagating perpendicular to \mathbf{B} . The effect of a density gradient is shown in fig. 2.3.3. The $\mathbf{E} \times \mathbf{B}$ drift shifts the thin plasma inwards and the dense one outwards on the left and right hand side of the initial perturbation. Hence, the whole structure propagates in electron diamagnetic drift direction because $\tilde{\Phi}$ continuously excites a density perturbation ahead in electron diamagnetic drift direction, which in turn gives rise to a potential perturbation by the parallel electron response and so on. The described mechanism ends up in a perturbation propagating in electron diamagnetic drift direction, which can in a linear picture be described as a plane wave, the drift wave.

The coupling between parallel and perpendicular dynamics leads to a finite parallel wavenumber for drift waves ($k_\parallel \neq 0$), which is much smaller than the poloidal wavenumber ($k_\parallel \ll k_\theta$) due to the strong anisotropy caused by the magnetic field. The result of a finite k_\parallel is that the wavefront of a drift wave is slightly tilted with respect to the magnetic field by an angle of ϑ , as indicated in fig. 2.3.4. The perpendicular phase velocity of the drift wave is $v_{dia,e}$. The small value of ϑ causes the wavefront to propagate predominantly in poloidal direction. The parallel phase velocity is given by $v_\parallel \approx v_{dia,e} \arctan \vartheta$.

In case of adiabatic electrons, reacting instantaneous to a density perturbation, \tilde{n} and $\tilde{\Phi}$ are in phase. This leads to a linear stable drift wave. The dispersion relation in this case is given by

$$\omega = \frac{\omega_{dia}}{1 + (k_\theta \rho_s)^2}, \quad (2.25)$$

where $\omega_{dia} = k_\theta v_{dia,e}$. Eqn. (2.25) is valid for low frequency drift waves with $\omega \approx \omega_{dia}$, whereas for high frequencies ($\omega \gg \omega_{dia}$) the fluid equations from which it is derived result in an Alfvén wave [Jen98]. The dispersion scale ρ_s is called the

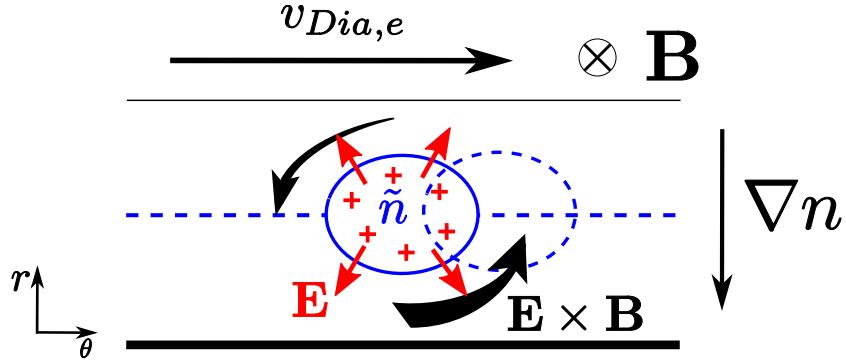


Figure 2.3.3: The existence of a density gradient is essential for the formation of a drift wave from the initial density perturbation shown in fig. 2.3.2. The circular $\mathbf{E} \times \mathbf{B}$ drift shifts the dense plasma outwards and the thin one inwards. As a result the perturbation propagates in electron diamagnetic drift direction.

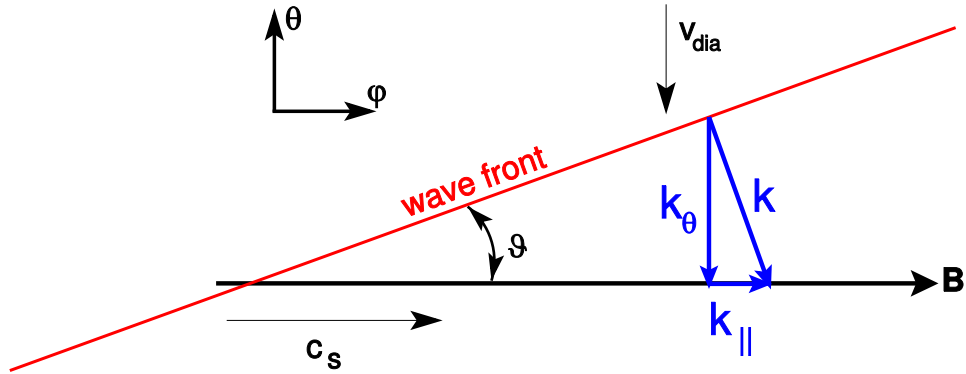


Figure 2.3.4: The coupling of parallel and perpendicular dynamics in the drift wave mechanism leads to a finite parallel wavenumber of the stable drift wave. Its wave front is tilted by a small angle of ϑ with respect to the magnetic field line. The parallel and perpendicular phase velocity are determined by the ion sound velocity c_s and the electron diamagnetic drift velocity $v_{dia,e}$, respectively.

drift parameter and is given by the ratio $c_s/\omega_{c,i}$. ρ_s is a characteristic scaling length for drift waves. For large scales ($k_\theta \rho_s \ll 1$) the dispersion relation is linearly. Eqn. (2.25) has a maximum at $k_\theta \rho_s = 1$ and decays for smaller scales. The deviation of the denominator in eqn. (2.25) from one reflects the increasing importance of the polarisation drift for the dynamics of drift waves for small scales. On scales of $k_\theta \rho_s > 0.3$ the polarisation drift starts to alter the parallel dynamics of the density perturbation [Mah07].

So far only adiabatic electrons have been considered, which lead to stable drift waves with density and potential fluctuations in phase. Any effect leading to non-adiabatic electrons leads to a destabilisation of drift waves and a finite phase shift between \tilde{n} and $\tilde{\Phi}$. Destabilisation occurs if the parallel mobility of the electrons is reduced. For weakly ionised plasmas the electron mobility is primarily reduced by electron-neutral collisions, in fully ionised and collisional plasmas mainly by electron-ion collisions, and in almost collisionless plasmas by kinetic effects, e.g. Landau damping [Gru01].

The identification of drift waves in the experiment can be done by checking a list of typical properties [Hor99]:

- Fluctuations are driven by the density gradient,
- Small cross phase between density and potential perturbations, typically $\alpha < \pi/4$,
- Phase velocity pointing in electron diamagnetic drift direction,
- Small but finite parallel wavenumber ($k_\parallel \ll k_\theta$),
- ρ_s is a typical poloidal scaling length for drift waves.

2.4 The Character of Turbulent Fluctuations

A general definition of turbulence has already been given in chapter 1. The following section will give a brief overview of some basic concepts describing the dynamics of turbulent systems.

The fundamental hydrodynamic equation describing the dynamics of an incompressible fluid ($\nabla \cdot \mathbf{v} = 0$) is the Navier-Stokes equation:

$$\frac{\partial \mathbf{v}}{\partial t} = -\mathbf{v} \cdot \nabla \mathbf{v} + \frac{\nabla p}{\rho} + \nu \nabla^2 \mathbf{v}. \quad (2.26)$$

\mathbf{v} is the velocity field of the fluid, p is the pressure and ρ the mass density of the fluid. ν is the kinematic viscosity. The nonlinear first term on the r.h.s. of the Navier-Stokes equation describes a change in \mathbf{v} by convective transport. The second term describes changes due to a gradient in the pressure, and the third term dissipation due to inner friction (ν) [Gro95]. The Navier-Stokes equation is also the equation of motion for turbulent flows. It has been found by Reynolds in 1883 [Rey83], that

the character of the flow can be described by a single dimensionless number, the Reynolds number:

$$\mathfrak{Re} = \frac{Lv}{\nu}. \quad (2.27)$$

L is a characteristic length scale describing the system under consideration, e.g. the diameter of a tube along which a fluid flows. \mathfrak{Re} describes the ratio of the time scales for molecular ($L^2/\nu \sim 1/\nu\nabla^2$) and convective ($L/v \sim 1/v\nabla$) momentum transport [Gro95]. For small values of \mathfrak{Re} the system is stable and the flow is laminar. Above a critical value of $\mathfrak{Re}_{crit} \approx O(10^3)$ a perturbation may become unstable and develop into turbulence. This is the case when the nonlinear convective term dominates the dynamics. The nonlinearity leads to a redistribution of the energy of the flow over a wide range of spatial scales of motion. However, a high Reynolds number does not automatically lead to turbulence. It only means that the system reacts more sensitively on perturbations. Hence, both the perturbation and \mathfrak{Re} must be large enough to reach turbulent states. The origin of turbulence is always an initial perturbation.

The distribution of energy over spatial scales can be thought of as a hierarchy of eddies of different spatial scales. In Fourier space a wave with a wavelength of the eddy size is assigned to individual eddies in the hierarchy. A broad band wavenumber spectrum consequentially follows from the hierarchy of eddies. In this context a common picture behind the development of turbulence is the nonlinear interaction of initially coherent waves. Two or more nonlinearly interacting waves of wavenumber \mathbf{k}_1 and \mathbf{k}_2 interact resulting in the drive of a third wave \mathbf{k}_3 with $\mathbf{k}_1 + \mathbf{k}_2 + \mathbf{k}_3 = 0$. This interaction process is called three-wave coupling. It provides an additional degree of freedom by driving a further wave, what allows further three-wave coupling processes. Finally in fully developed turbulence many wave triplets are exchanging energy amongst each other. The complete dynamics involves many degrees of freedom. Each interaction is coherent, but the fact that there are many of them going on simultaneously results in a weak degree of overall coherence between waves at differing \mathbf{k} . These processes lead to nonlinear growth or damping of the various modes. Saturated steady-state turbulence results if the rate at which each \mathbf{k} mode gains energy is balanced by the losses of energy to the particles or other modes [Lie85]. The turbulent system has a short term memory: dynamics at the same spatial point but separated in time become uncorrelated beyond a time range called the correlation time. The dynamics in this case has to be treated statistically.

The spatial distribution of energy has been first treated mathematically by Kolmogorov in 1941 [Kol91]. He considered the case of isotropic turbulent flows under the assumption that energy is put into the system at scales which are much larger than the dissipation scale defined by the viscosity. The theory is based on similarity considerations assuming that in the intermediate range between energy input and dissipation no scale length is preferred. The result is, that the energy distribution in wavenumber space in this intermediate range follows a power law²: $E(k) \propto \epsilon^{2/3} k^{-5/3}$. The range, where these assumptions hold is called inertial range. The typical shape

²The exponent ($-5/3$) is called spectral index

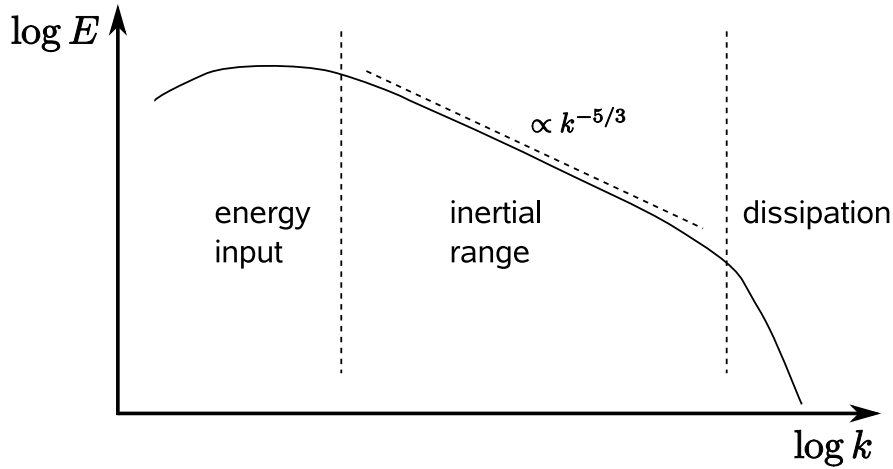


Figure 2.4.1: Typical shape of a turbulent wavenumber spectrum for the case of homogeneous isotropic turbulence. Energy is injected at small wavenumbers (large scales) and dissipated at large wavenumbers (small scales). The intermediate range, called inertial range, follows a power law decay.

of a turbulent wavenumber spectrum is shown in fig. 2.4.1. The flat region at low k is the range where energy is put into the system, e.g. by stirring. These large scale vortices split into smaller and smaller ones in the inertial range, where the energy is conserved. At small scales (high k) the spectral index gets higher, because energy is lost by dissipation.

Plasma turbulence is phenomenologically similar to fluid turbulence. But, the dynamics of plasma particles is much more complicated than in neutral fluids because electrical and magnetic forces act in addition to the viscous force in a neutral fluid. Furthermore, in magnetised plasmas a strong anisotropy is caused by the magnetic field. One has to distinguish between different scales: the free propagation of electrons along the magnetic field leads to a much larger parallel scale than perpendicular to \mathbf{B} where the dynamics is governed by drifts. This anisotropy has already been mentioned above in the explanation of the drift wave mechanism ($k_{\parallel} \ll k_{\theta}$). The assumptions leading to Kolmogorov's spectral law are not valid anymore in this case. In addition to the anisotropy, the clear separation between scales of energy input and dissipation is not generally given. Hence, it may be expected to find wavenumber spectra following the shape of fig. 2.4.1 in general, but the spectral index can be completely different.

2.5 Theoretical Modelling of Drift Wave Turbulence

Drift waves as a universal instability are one of the most commonly observed instabilities in magnetic confinement [EMMM80]. Theoretical modelling of turbulence driven by drift wave instabilities has been first undertaken by Hasegawa and Mima [HM77; HM78] who derived equations to handle fluctuations in magnetised plasmas including drift wave physics with adiabatic electrons and cold ions in their model. Numerical simulations including realistic parameters for tokamak edge plasmas have been undertaken by Wakatani and Hasegawa [WH84]. Wavenumber spectra for fully developed turbulence found by these authors are in good agreement with experiments. However, a discrepancy between theory and experiment has been found in the place of the shoulder of the spectrum where the inertial range starts. These early simulations predicted the shoulder to be located at the dispersion scale of the drift wave, $k_{\perp}\rho_s \approx 1$. Experiments report the shoulder to be located typically around $k_{\perp}\rho_s \approx 0.15$ [Lie85]. Terry and Diamond [TD85] found a better agreement with experiments by taking additional dissipation effects, i.e. electron dynamics parallel to \mathbf{B} into account. The width of the spectra is reduced in their simulations. The inertial range follows a power law with a spectral index of $-17/6$.

Over the years turbulence simulation codes experienced a continuous evolution by including more and more details into the underlying models. This evolution is closely associated to the progress in computer technology. Modern turbulence simulation codes are three-dimensional implementations of either fluid or gyrokinetic equations in realistic geometry of tokamaks or stellarators (see e.g. [Sco06; Sco07] for recent overview articles).

Some simulation results, which are specifically of interest for this work, shall be mentioned here. The 3D turbulence code DALF3 [Sco97b], based on an electromagnetic fluid model, has been used to simulate turbulence in the TJ-K torsatron [NSS02]. The DALF3 code was originally developed for fusion edge plasmas. Its applicability for low temperature plasmas is based on the use of dimensionless parameters controlling the dynamics in the simulations. These parameters are in a wide range comparable for low temperature plasmas like in TJ-K and fusion devices. As a result of these simulations, it was predicted that drift waves are the dominant instability mechanism driving turbulence in TJ-K. The prediction could be verified experimentally [Str+04; Mah+07]. Plasma parameters in TJ-K as well as the machine dimensions are comparable to WEGA parameters. Therefore, drift wave turbulence is also expected to be found in WEGA, which shall be clarified within this work.

Chapter 3

Data Analysis Methods

The statistical nature of turbulence makes a careful treatment of raw data necessary. Looking at the raw data from turbulent systems one can hardly discriminate it from strong noise. Therefore, raw data is treated with several statistical methods to recognise the intrinsic correlations and to characterise the dynamics of fluctuations. During data processing one always has to keep in mind that the data is quantised both in time (by ADC sampling rates) and space (by the geometry of diagnostics). Spatio-temporally resolved data appear as a series of discrete values $f_{i,j}$ with $i = 0, 1, \dots, M - 1; j = 0, 1, \dots, N - 1$, where M is the number of points in space and N is the number of samples taken in time. The spatial quantisation is especially restrictive and leads to strong limitations in the significance of results because a part of the information is always lost. The methods used to analyse data in this work is introduced in the following sections.

3.1 Statistical Analysis

3.1.1 Distribution Function

One feature characterising turbulent systems is the irreproducibility of instantaneous values. The probability distribution function (PDF) of a turbulent system is close to the Gaussian distribution of a random signal. The deviation from Gaussian distribution can give information about the nature of turbulent signals. For example a typical feature observed for turbulent transport would be intermittency¹ which appears as a high amplitude tail in the PDF. For discrete signals the PDF is not a continuous function but a histogram describing the probability p_f to find the signal amplitude f_j in a certain interval.

¹Textbook definition of intermittency [Fri95]: “A signal is intermittent, if it displays activity during a fraction of time only, which decreases with the scale under consideration.”

3.1.2 Statistical Moments

The shape of a PDF can be characterised by moments which are in general defined by [WH87]:

$$m_n = \frac{1}{N} \sum_{j=0}^{N-1} (f_j - \mu)^n, \quad (3.1)$$

where m_n is the n^{th} moment of a random signal f_j . μ is the ensemble average of f_j defined by:

$$\mu = \frac{1}{N} \sum_{j=0}^{N-1} f_j. \quad (3.2)$$

For $N \rightarrow \infty$, μ tends to the expected value of f . For real measurements appearing as a series of discrete values μ as well as m_n are estimates of the real values. The first moment in this definition is zero. The second moment is called variance, the positive square root of which is the standard deviation, σ :

$$\sigma^2 = \frac{1}{N-1} \sum_{j=0}^{N-1} (f_j - \mu)^2. \quad (3.3)$$

For fluctuation data σ describes the total and σ/μ the relative fluctuation amplitude. A signal with Gaussian PDF is sufficiently described by the ensemble average and standard deviation. The deviation from Gaussian distribution is described by the third and fourth moment called skewness S and kurtosis K , respectively:

$$S = \frac{m_3}{m_2^{3/2}}, \quad (3.4)$$

$$K = \frac{m_4}{m_2^2} - 3. \quad (3.5)$$

For a Gaussian distribution S and K are 0. Negative skewness means that the PDF is more flat for $f < \mu$ than for $f > \mu$. K is a measure for the steepness of the PDF around its maximum. $K > 0$ implies a steeper PDF around the maximum than Gaussian distribution and that most of the variance is due to infrequent extreme deviations, as opposed to frequent modestly-sized deviations. S and K are of interest when the intermittency of fluctuations is to be characterised.

3.2 Correlation Function

Correlation describes the degree of relationship between two random variables. Correlation analysis is a widely used powerful tool to obtain averaged information about fluctuating phenomena [Rit+88]. The cross-correlation function (CCF) of two continuous time dependant signals $f(t)$ and $g(t)$ is defined as :

$$\psi_{fg}(\tau) = \int_{-\infty}^{\infty} f(t)g(t + \tau)dt \quad (3.6)$$

For discrete signals ψ_{fg} can also be discretised:

$$\psi_{fgi} = \frac{1}{N - |i|} \sum_{j=\max(0,-i)}^{\min(N-1,N-1-i)} f_j g_{j+i} \quad j = 0, \dots, N - 1 \quad (3.7)$$

The CCF is a measure for the similarity of two signals shifted against each other by a time lag τ . It shows a maximum at the certain time lag where f and g have a similar shape in amplitude. For spatio-temporally resolved signals the CCF can be expanded into two dimensions. In most cases the spatial resolution is limited to one dimension, e.g. the poloidal resolution of the probe array used in this work. For continuous signals $f(x, t)$ and $g(x, t)$ being functions of the spatial position x and time t , ψ_{fg} is then written as

$$\psi_{fg}(d, \tau) = \int_{-\infty}^{\infty} \int_{-\infty}^{\infty} f(x, t) g(x + d, t + \tau) d\tau dd, \quad (3.8)$$

where d is the spatial distance between the signal sources. The 2D CCF can again be discretised. The second integral in eqn. (3.8) is an averaging in space, or in the discrete case an averaging about channels with equal distance. This is justified if fluctuations are homogeneous in space and the CCF depends only on the distance between channels and not on the absolute position. This assumption is not generally valid, even for poloidally resolved experiments, where probe tips are aligned on a flux surface. Although flux surfaces are assumed to describe isobars for the plasma, asymmetries of fluctuation parameters on flux surfaces are a common observation in fusion devices [Zwe+07]. CCF of identical signals is called the auto-correlation function (ACF). For turbulence measurements the CCF can give important information about fluctuation parameters like lifetime, size and velocity of turbulent structures. The random part which is always present in signals is efficiently removed by the averaging process. For noisy signals it may appear in the ACF as a narrow peak around $d = 0, \tau \approx 0$. Theoretically for a continuous white noise signal ψ_{ff} is the Dirac delta function.

In this work the correlation function is always presented in a simple normalised form where each element is divided by $\psi_{ff}(0, 0) \approx \sigma$.

Restrictions in the Applicability of Correlation Analysis

A prerequisite for the application of eqn. (3.8) is that fluctuation events occur randomly both in space and time. This is easy to explain in space. The CCF is not sensitive to the absolute position of the origin of data. The space lags in eqn. (3.8) is the probe distance. Fluctuations that appear predominantly at a certain position in the sampled region would be smeared out by the CCF because they are treated as the stochastic noisy part of the signal and not the statistically reproducible part of turbulence.

Furthermore the results from the two-dimensional CCF have to be interpreted carefully, because a lack of spatial information may lead to artefacts. The reason is,

that the dynamics are captured only in one spatial dimension. Poloidally resolved measurements are not able to see any radial movement of turbulent structures. For example a structure moving in radial direction is recognised in a poloidally resolved measurement as a standing structure with a lifetime corresponding to the ratio of radial size and velocity.

3.3 Fourier Analysis

As shown in section 2.4 information about the spectral properties is important to understand turbulence.

3.3.1 One-Dimensional Fourier Transform

The transition from the time to the frequency domain for a continuous signal $f(t)$ is given by the Fourier transform:

$$F(\nu) = \int_{-\infty}^{\infty} f(t)e^{-i2\pi\nu t} dt. \quad (3.9)$$

The discrete Fourier transform (DFT) for a series of N equidistantly sampled points with a sampling frequency ν_s is defined as:

$$F_j = \sqrt{\frac{\Delta t}{N}} \sum_{k=0}^{N-1} f_k e^{-\frac{i2\pi jk}{N}} \quad k = 0, \dots, N-1, \quad (3.10)$$

where Δt is the inverse sampling frequency. The frequency resolution for the DFT is also discretised ($\Delta\nu = \frac{1}{N\Delta t}$). For real signals the spectrum is complex and Hermitian:

$$F_n = F_{N-n}^*,$$

where F^* denotes the complex conjugate. Therefore, the full spectral information is contained in the interval $j = 0, \dots, \lfloor \frac{N}{2} \rfloor$. In order to recover all frequency components in the sampled waveform sufficiently high sampling frequency is required. The highest frequency that can be resolved by DFT is limited by the Nyquist sampling theorem to $\nu_{Nyq} = \frac{\nu_s}{2}$. Higher frequencies are mirrored at ν_{Nyq} and appear in the spectrum as low frequency components (aliasing effect). For the practical case aliasing is prevented by using appropriate lowpass filters with an edge frequency below ν_{Nyq} . $F(\nu)$ describes a complex spectrum in general which can be separated into amplitude and phase. The absolute phase of single signals is not of interest, because it depends on the trigger time of sampling. Of great interest in fluctuation studies is the squared amplitude of the DFT, called power spectrum or power spectral density (PSD):

$$S(\nu) = |F(\nu)|^2 = F^*(\nu)F(\nu). \quad (3.11)$$

$S(\nu)$ is the power carried by the Fourier component of $f(t)$ at a certain frequency. Integrating the PSD one obtains the overall power in a signal which is related to the standard deviation:

$$\sigma = \int_{-\infty}^{\infty} S(\nu) d\nu. \quad (3.12)$$

Digitally computed power spectra always carry a statistical error manifesting itself in a large amount of jitter [SPC74]. A common method to reduce this noise is to average spectra over several realisations of the statistical process [The90]. The Fourier transform is then written as:

$$\bar{F}(\nu) = \langle F(\nu) \rangle, \quad (3.13)$$

where $\langle \rangle$ is the ensemble average over several realisations. In practice, ensemble averaging is done by splitting long time traces into subwindows. Fourier transformation is then applied to the individual subwindows and finally spectra from sub-windows are averaged. The bar indicating averaged spectra is omitted in the following because the process of ensemble averaging is treated as standard technique.

3.3.2 Cross Spectrum and Coherence

The phase relation between fluctuating quantities determines turbulent transport (see section 2.2.2) and is important to identify the inherent instability mechanisms (see section 2.3.2). Information about the relative phase between two signals $f(t)$ and $g(t)$ can be obtained from the complex cross spectrum which is defined as:

$$\Psi_{fg}(\nu) = F^*(\nu)G(\nu). \quad (3.14)$$

The complex phase of $\Psi_{fg}(\nu)$ is called the cross-phase spectrum:

$$\alpha_{fg}(\nu) = \arg\{\Psi_{fg}(\nu)\}. \quad (3.15)$$

$\alpha_{fg}(\nu)$ is the relative phase between the two signals f and g at a given frequency ν . The amplitude is called cross-power spectrum which is often presented in a normalised form:

$$\gamma_{fg}(\nu) = \frac{|\Psi_{fg}(\nu)|}{\sqrt{\Psi_{ff}(\nu)\Psi_{gg}(\nu)}} \in [0, 1], \quad (3.16)$$

where $\Psi_{ii}(\nu) = S_i(\nu)$ is the auto-power spectrum, which is equal to the PSD. $\gamma_{fg}(\nu)$ is called coherence spectrum. It is a measure for the phase coherence of two signals at a given frequency.

When eqn. (3.14) is applied to congenerous signals from spatially separated probes, the cross-phase can be interpreted as a local dispersion relation. Following Beall et al. [BKP82]

$$k_y(\nu) = \frac{\alpha(\nu)}{\Delta y} \quad (3.17)$$

is the dispersion relation assuming that turbulence can be interpreted as a superposition of planar waves with a fixed wavenumber and frequency. Δy is the spatial separation of the measurement points. Eqn. (3.17) is valid provided that a significant coherence is observed at a given frequency.

3.3.3 Averaged Cross-Phase

At some points it is useful to merge a cross-phase spectrum into a single number. To this end, an averaged cross-phase $\bar{\alpha}$ is used following the definition given by Ritz et al. [Rit+88]:

$$\bar{\alpha}_{fg} = \frac{\int \Psi_{fg}(\nu) \alpha_{fg}(\nu)}{\int \Psi_{fg}(\nu)}. \quad (3.18)$$

$\alpha(\nu)$ is weighted with the cross-power because the cross-phase is only relevant for spectral regions where both signals f and g show a significant power and coherence. One application of eqn. (3.18) is the evaluation of an averaged phase shift between different fluctuating quantities measured at the same position in space. A further application is the derivation of an averaged wavenumber from a measurement at two points separated in space by averaging eqn. (3.17).

3.3.4 Wavenumber-Frequency Spectrum ($k\nu$ -spectrum)

Similar to the two-dimensional correlation function the Fourier transform can also be expanded to more than one dimension. Additional to the transform of temporally resolved data into frequency space, spatially resolved data is transformed into wavenumber space in this work. The typically low number of data points in space (e.g. 13 probe tips of the array in this work) leads to another spurious effect in digital signal processing besides aliasing. DFT always assumes the input signals to be either periodic or an infinite series of samples. This assumption can never be fulfilled when unknown signals are detected with a fixed number of samples. Discontinuities at the boundaries lead to a shift of energy from real Fourier components to artificial components, an effect called spectral leakage. This effect gets stronger when the signal length becomes shorter. To limit spectral leakage to a minimum, the data can approximate an infinite sequence by decaying to zero at both endpoints. This is accomplished by multiplying with a windowing function. In this work the Hanning window, expanded to two dimensions, is chosen [Bri88]:

$$W_H(\Delta t, \Delta y) = \frac{1}{2} + \frac{1}{2} \cos \left(\pi \sqrt{\left(\frac{\Delta t}{\Delta t_H}\right)^2 + \left(\frac{\Delta y}{\Delta y_H}\right)^2} \right), \quad (3.19)$$

if $\left(\frac{\Delta t}{\Delta t_H}\right)^2 + \left(\frac{\Delta y}{\Delta y_H}\right)^2 \leq 1$, elsewhere $w_H(\Delta t, \Delta y) = 0$,

where Δt_H and Δy_H are the window width in time and space, respectively. When DFT is applied to spatially resolved data, aliasing cannot be prevented by applying filters. Hence the channel separation has to be chosen carefully according to the expected spectral range of data (see section 4.4.1).

3.3.5 Relation between Correlation Function and Fourier Transform

Power spectrum and cross-correlation function have the same information content. Following the Wiener-Khintchine theorem, PSD and CCF represent a pair of Fourier transformed.

$$\Psi_{fg}(\nu) = \int_{-\infty}^{\infty} \psi_{fg}(\tau) e^{-i2\pi\nu\tau} d\tau \quad (3.20)$$

Eqn. (3.20) is used to calculate $k\nu$ -spectra in this work. Although this leads to an increase in computation time² this method brings along some advantages compared to the direct transformation of raw data. Computation time turned out not to be a relevant problem for data processing in our case. One advantage of this method is an increase in spectral resolution which is helpful in wavenumber space, where the small number of data points leads to strong restrictions. The Fourier transform of a series of N points results in a spectrum with $N/2$ points on the abscissa ($(N - 1)/2$ if N is odd). The CCF of N points has $2N - 1$ points. Therefore, the Fourier transform following eqn. (3.20) has N points. In wavenumber space this leads to an increase from 6 to 12 points for the data from the poloidal array. The Nyquist limit is not affected by this expansion. In frequency space this effect is not of importance because time series are usually long enough for a reliable direct Fourier transformation. Using this method to estimate $k\nu$ -spectra another aspect of windowing has to be considered which is again only of importance in the spatial dimension with a low number of points. For small space lags the CCF is quite robust because it averages over a number of realisations of this space lag. However, at large separations very few points enter into the averaging process of the CCF making it less robust. The Fourier transform may therefore only be performed for small lags, or these points must be weighted more heavily in the calculations. This restriction can be implemented by windowing the CCF [McC82]. The spatial window width Δy_H should be set to the largest available extent because of the low number of points available. In the temporal domain the number of available points is usually much larger than the width of the correlation function. Therefore, Δt_H should be chosen to be much smaller than the length of the data set. In [Sch05] a window width of several hundred bins is suggested. The application of a smaller Hanning window to the correlation function has the effect of smoothing the frequency spectrum because the resulting spectrum is the convolution of the real spectrum with the broad spectrum of the windowing function.

²The Fast Fourier Transform (FFT) algorithm provides a very fast and efficient method to calculate the DFT. But the sum in eqn. (3.8) must be calculated before FFT can be applied to the CCF.

Chapter 4

Experimental Setup and Diagnostics

The following chapter gives an overview of the experimental framework for this work, namely the WEGA stellarator. The general setup of the machine will be explained followed by the magnetic configuration and equilibrium plasma parameters. Features being important for this work will be explained in more detail. The diagnostics used to study fluctuations within this work are electrostatic probes. Hence, some theoretical background on the operation of probes will be explained, as well as the technical realisation of probe diagnostics for spatio-temporally resolved fluctuation measurements in WEGA.

4.1 The WEGA Stellarator

WEGA (**W**endelstein **E**xperiment in **G**reifswald zur **A**usbildung) is a classical stellarator which belongs to the family of Wendelstein stellarators [GRW85]. It was originally constructed as a combined tokamak and stellarator experiment in the 1970's in Grenoble, France. Since 2001 WEGA has been operating in Greifswald in the stellarator configuration. The main purposes of WEGA operation in Greifswald are basic plasma research, the education of scientific and technical staff and the testing of diagnostic equipment and plasma control schemes and techniques for Wendelstein 7-X. WEGA a small stellarator with a major radius of $R = 72$ cm. The maximum average plasma radius defined by in vessel components is $a = 11.5$ cm. The 2.45 GHz heating antennas act as limiter. Fig. 4.1.1 shows the main technical components of WEGA. The toroidal field is produced by 40 toroidal field coils. Two pairs of helical field coils are wound around the vacuum vessel. The coil setup results in a $l = 2, m = 5$ configuration, where l is the poloidal and m the toroidal mode number. The magnetic field configuration has a fivefold toroidal symmetry. According to the toroidal symmetry the shape of flux surfaces repeats every 72° . Additional vertical field coils can be used to shift the plasma column in radial direction. As working gases H_2 , He, Ne and Ar are used. The plasma is generated by electron cyclotron resonance heating (ECRH) using microwaves. Two microwave

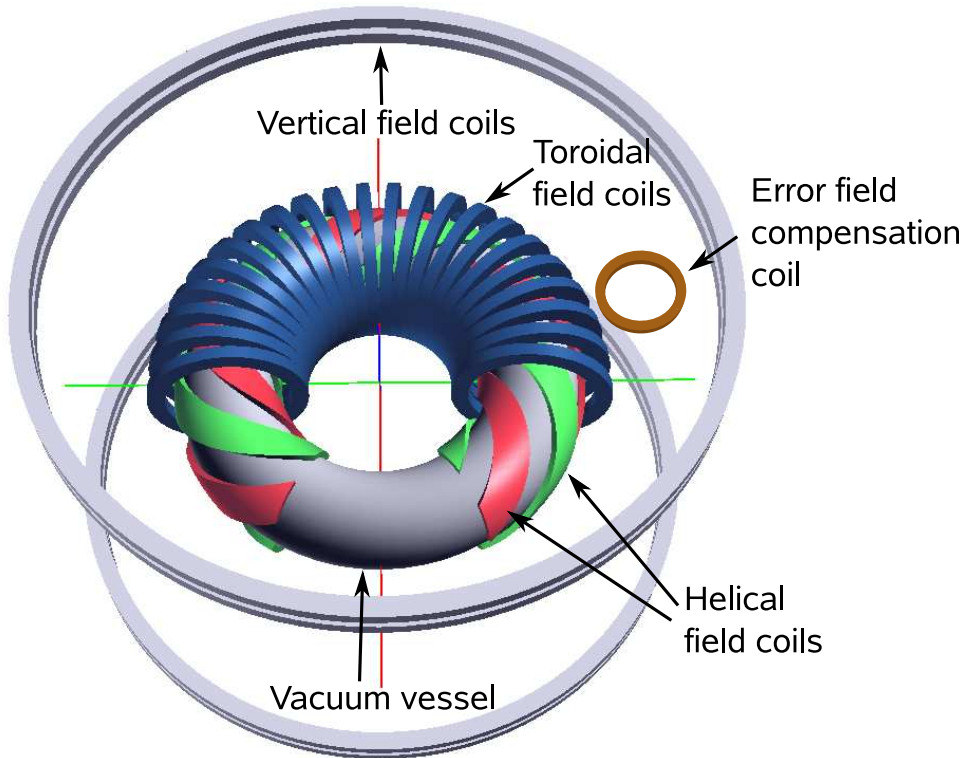


Figure 4.1.1: Magnetic field coil configuration of WEGA. The toroidal and helical field coils are mandatory to produce a field configuration with closed flux surfaces. The vertical field coils represent a Helmholtz coil setup. They can be used to shift the plasma radially and to manipulate the magnetic shear. The error field compensation coils are used to manipulate magnetic islands.

heating systems are available operating at frequencies of 2.45 GHz and 28 GHz, respectively.

2.45 GHz ECRH Two microwave generators (magnetrons) operating at a frequency of 2.45 GHz with a power of 6 kW and 20 kW (cw), respectively, are installed on WEGA. For this frequency the vacuum wavelength is $\lambda = 12$ cm which is comparable to the plasma radius. The frequency corresponds to the electron cyclotron frequency at a magnetic field strength of $B = 87.5$ mT. However, due to the complex heating mechanism explained below optimised plasma parameters can be obtained at a reduced field of $B_0 = 57$ mT [Hor05], where B_0 is the magnetic field strength at the magnetic axis. The plasma is heated by electrostatic Bernstein waves [Ber58] which are generated in a mode conversion process. Microwaves are launched into the plasma in the horizontal plane from the antenna in the ordinary mode (O-mode) under an angle of $\approx 40^\circ$ with respect to the magnetic field vector. The O-mode wave propagates towards the O-cutoff layer where it is partially converted into a slow extraordinary (SX) mode. The SX mode propagates back to the upper hy-

brid resonance (UHR) layer where it is converted into an electrostatic Bernstein (B) mode. The B mode can propagate into the overdense plasma without a density limit. It is absorbed in the plasma edge region. The efficiency of this O-X-B mode conversion process is quite sensitive to the magnetic configuration [Pod+07].

28 GHz ECRH The second heating system installed at WEGA is a gyrotron operating at a frequency of 28 GHz with a maximum power of 10 kW (cw). The resonant magnetic field strength for electrons at this frequency is 1 T. Since WEGA can only be operated up to 0.9 T the second harmonic is used to heat the plasma at $B = 0.5$ T. The beam is launched into the plasma in the extraordinary (X2) mode using a mirror system focussing the beam in the plasma centre. The mirror system is set up to optimise the heating efficiency by multipath absorption of the beam due to reflections with the stainless steel vessel [War+06; Ott+07a]. The vacuum wavelength of $\lambda \approx 1$ cm which is short compared to the plasma radius allows the resonance condition for electrons to be fulfilled locally. Hence, a central power deposition is possible with this system if the magnetic field strength matches the resonance condition at the magnetic axis. This results in a much higher heating efficiency compared to the O-X-B mode conversion process used at 2.45 GHz.

4.2 Magnetic Configuration

The magnetic field in WEGA is produced by several coil systems, resulting in a very flexible field configuration. For steady state operation the toroidal field is limited to $B_0 \approx 0.4$ T and can be increased up to 0.9 T for short pulses of a few seconds. The rotational transform t can be varied in wide range from a value close to 0 up to approximately 1 by increasing the current in the helical field coils. The rotational transform on the magnetic axis t_0 is calculated by [Sch94]:

$$t_0 = 0.0972 \left(\frac{I_H}{I_T} \right)^2. \quad (4.1)$$

Two vertical field coils in a Helmholtz configuration can be used to shift the plasma column in the horizontal direction. The vertical field also has an influence on the magnetic shear. WEGA is designed as a low shear experiment. A typical t -profile and the corresponding shear profile is shown in fig. 4.2.1. The low shear allows to find configurations without low order rational surfaces in the region of closed flux surfaces. The last closed flux surface (LCFS) is for $t < 0.3$ defined by a mechanical limiter. It is determined by the first magnetic surface touching a limiting component in the vessel in these configurations. For WEGA the first limiting structures are the ECRH antennas used for 2.45GHz heating. Vacuum magnetic surfaces exist also in the limiter shadow for low t configurations (Dashed lines in fig. 4.2.2. The region outside the LCFS is called the scrape off layer (SOL). Particles entering the SOL cannot propagate freely on a flux surface anymore but will be peeled off by the limiter even without any radial transport. The magnetic field configuration

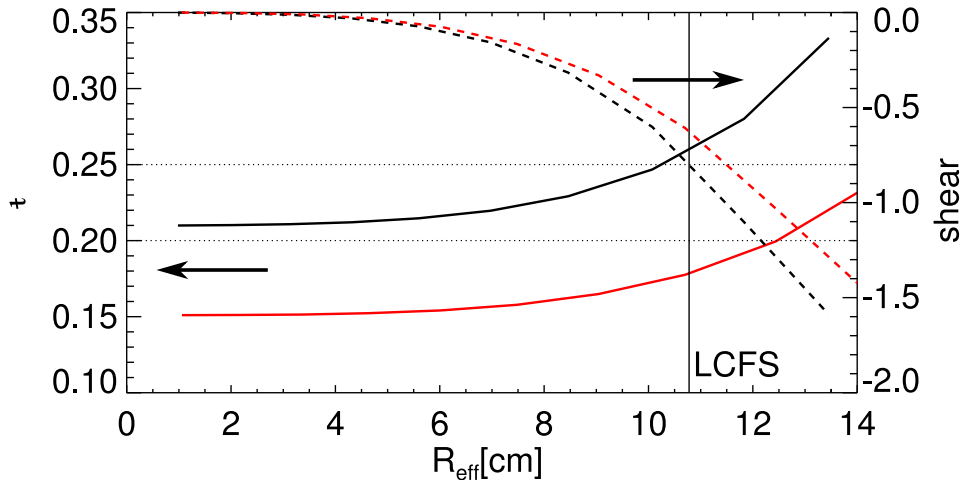


Figure 4.2.1: Radial profiles of the rotational transform t in WEGA and the corresponding magnetic shear s for two arbitrary example configurations at low t without vertical magnetic field. Due to the low magnetic shear it is possible to find magnetic configurations without low order rational surfaces within the LCFS. The dashed horizontal lines indicate the $t = 1/5$ and $1/4$ resonances.

can be calculated using a field line tracing code [Wer] in which the coil setup of WEGA is implemented. The code allows the tracing of magnetic field lines as well as trajectories of charged particle in the magnetic field. Figure 4.2.2 shows a Poincaré plot of vacuum magnetic surfaces in WEGA generated by the code for a limiter configuration ($t_0 = 0.182$). Individual flux surfaces in the plot are generated by following a magnetic field line starting from an arbitrary point on the flux surface for a high number of toroidal turns. A point in the plot is generated everytime the field line crosses the observed φ -plane. For closed flux surfaces the piercing points have been connected to solid lines. The figure shows a set of nested magnetic flux surfaces in a $r - \theta$ plane at constant φ .

The LCFS is at an effective radius of $r_{eff} = 11.5$ cm. r_{eff} is defined as the radius of a circle covering the same area as the corresponding flux surface. For higher t closed magnetic surfaces exist only up to radii located inside the fixed limiter position resulting in magnetic separatrix configurations.

Code calculations describe the properties of the ideal vacuum magnetic field which contains only field perturbations connected to the fivefold toroidal symmetry. These perturbations are inherent to the coil system of WEGA and lead to so-called 'natural' magnetic islands on resonant surfaces $t = \frac{5}{n}$, where n is the poloidal mode number. These islands have been found experimentally and in the code simulations, e.g. at $t = 5/9$, but they are very small and not of interest for this work. Non-natural islands, produced by additional perturbation fields, breaking the toroidal symmetry are more important for WEGA operation. These may for example be generated by currents in supply lines, a small misalignment of coils or external

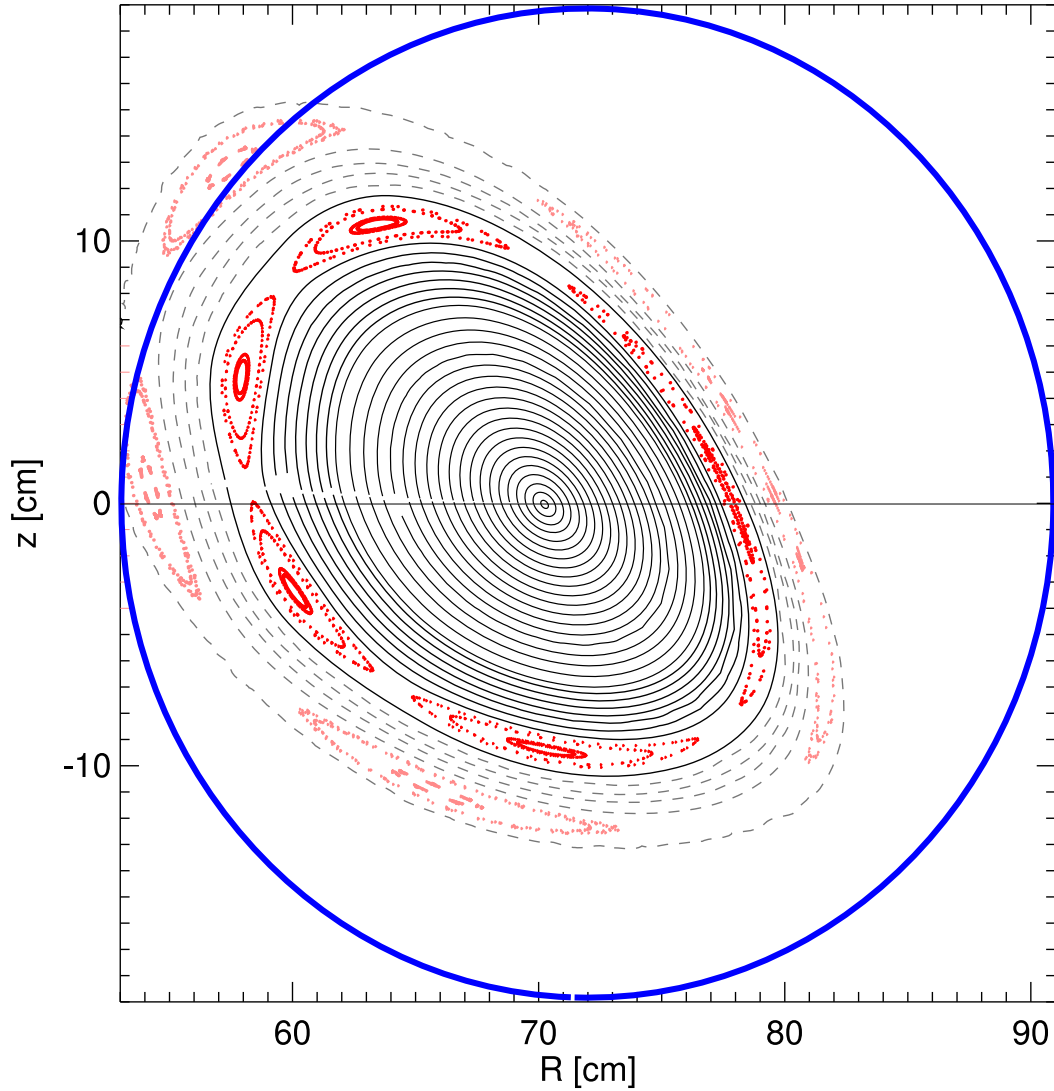


Figure 4.2.2: Poincaré plot of vacuum magnetic surfaces for a magnetic field configuration with $t_0 = 0.182$ including a field error. Solid black lines are closed flux surfaces. Grey dashed lines are open flux surfaces which are in contact with limiting components. Non natural $m = 1$ island chains are plotted in red. The $\tau = 1/5$ island chain is located inside the LCFS. The $\tau = 1/4$ island chain is far outside the LCFS. The shown flux surface configuration corresponds to a toroidal angle coordinate of $\varphi = 144^\circ$, where the poloidal probe array (see sec. 4.4.1) is located.

magnetic fields. Such non-natural islands with toroidal mode numbers of $m < 5$ have been found in flux surface measurements in WEGA [OL02]. Experimentally islands with $m = 1, n = 1 \dots 7$ and $m = 2, n = 3$, respectively, have been identified. The exact source of the field error is unknown as well as its full spectrum of Fourier components. The experimentally observed islands reflect only a part of the full spectrum of the perturbation. However, it has been found that the island width and thus the amplitude of the error field is independent of the magnetic field strength. This implies that the perturbation is due to a geometrical misalignment of coils or due to fields from components driven by the coil current, e.g. supply lines. In the computer code the error field can be simulated by a misalignment between the system of toroidal and the helical field coils, which are in the experimental setup also mechanically decoupled, i.e. individual coils. A radial shift of 3 mm at a toroidal angle of $\varphi = 280^\circ$ produces the appropriate error field to reproduce at least the $m = 1$ and $m = 2$ islands. An exaggerated representation of the geometrical shift is depicted in fig. 4.2.3. Using such a perturbation, the calculated flux surfaces coincide well with measurements. The flux surfaces in fig. 4.2.2 are calculated including the additional perturbation. Two resonances with corresponding magnetic islands are present in the given example; the $\iota = 1/5$ resonance can be seen just inside the LCFS and the $\iota = 1/4$ resonance is located in the limiter shadow. The island width w depends on the one hand on the rotational transform (see eqn. (2.13)). On the other hand, w is not constant on a flux surface. On the low field side of the plasma, which is accessible for probe diagnostics, it is about 1 cm. On the high field side, the island width is at least two times higher and the ι dependence is much higher.

4.2.1 Error Field Compensation

For the magnetic configurations, which are of interest for this work, only $m = 1$ islands were observed. They can theoretically be compensated by introducing an appropriate additional perturbation field. The effect of island compensation can be explained in terms of the Fourier decomposition of fields. A perturbation of a certain toroidal mode number m can be compensated by adding a corresponding Fourier component of the same amplitude phase shifted by π [KA05]. In simulations it could be shown, that the $m = 1$ field perturbations can be influenced effectively by means of simple circular coils placed besides the torus. To this end so called error field compensation coils (EFCC) have been installed at WEGA producing an additional error field. A set of four water-cooled coils with a mean diameter of 30 cm and 36 windings each are used. The coils can be operated at currents up to $I_{cc} = 500$ A. Fig. 4.2.3 shows schematically, how the compensation coils act against the original error field (the misalignment of the toroidal and helical field coils is exaggerated). Ideally the compensation coils should be located at a toroidal angle of $\varphi = 100^\circ$ for optimum compensation. Practically this position is very close to one of WEGA's transformer yokes. In a first campaign of flux surface measurements was been found that the presence of iron close to the coils leads to a strong nonlinearity in the current needed to compensate the islands [OLW03]. To avoid this the new set of coils have

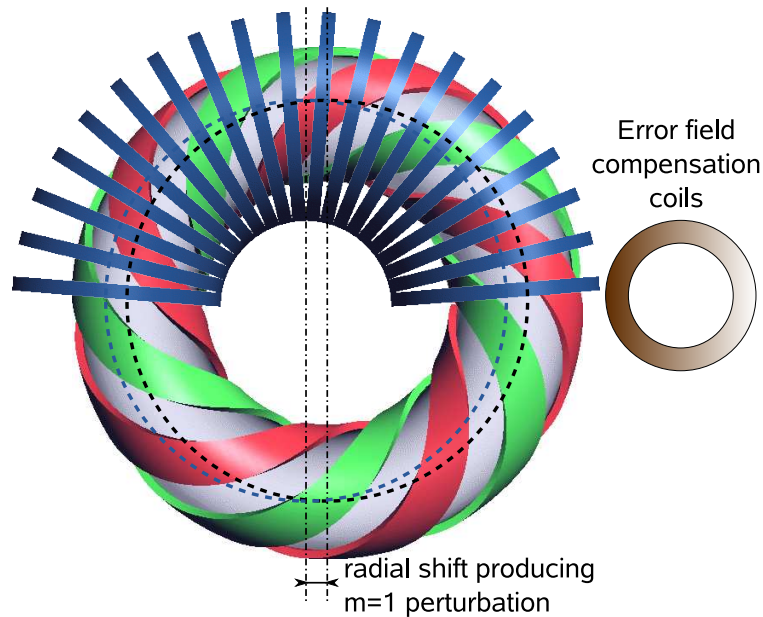


Figure 4.2.3: *The error field producing non-natural magnetic islands in WEGA can be simulated by a radial shift of the whole set of toroidal field coils with respect to the helical field coils. This shift is indicated here strongly exaggerated. The error field compensation coils are installed at a toroidal position, shifted by $\varphi \approx 180^\circ$ with respect to the origin of the intrinsic field error.*

been placed centrally between two yokes at $\varphi = 126^\circ$. The coils can be vertically shifted and tilted in order to locate a position where compensation is most effective. This flexibility was found necessary, as it was not clear whether the compensation would be successful at positions predicted by field line tracing calculations. Such calculations predicted that it is possible to compensate the islands with the EFCC placed as shown in fig. 4.2.4 a). Here, a set of three coils are tilted by 45° and shifted in the vertical direction by about 30 cm. Setting $B_0 = 500$ mT the available current of $I_{cc} = 500$ A was found to be sufficient to compensate the island at $t = 1/5$. However, in flux surface measurements it was found that $I_{cc} = 500$ A is not sufficient for compensation at this configuration. In experiments at a reduced toroidal field it could be shown that the current which is necessary to compensate the islands is about three times higher than the theoretical predictions. Experimentally the optimum compensation for this magnetic configuration was observed with four coils placed in the equatorial plane as shown in 4.2.4 b), with $I_{cc} = 500$ A. The error could still not be fully compensated, but the island width w was reduced by a factor of about 2 without changing the poloidal phase of the island chain. Following the square root dependency of w on the perturbation field amplitude (eqn. (2.13)), this means that the EFCC compensates about 75 % of WEGA's intrinsic error field for the $t = 1/5$ resonance under consideration. Keeping the phase constant during compensation is necessary to discriminate between effects related to the island width

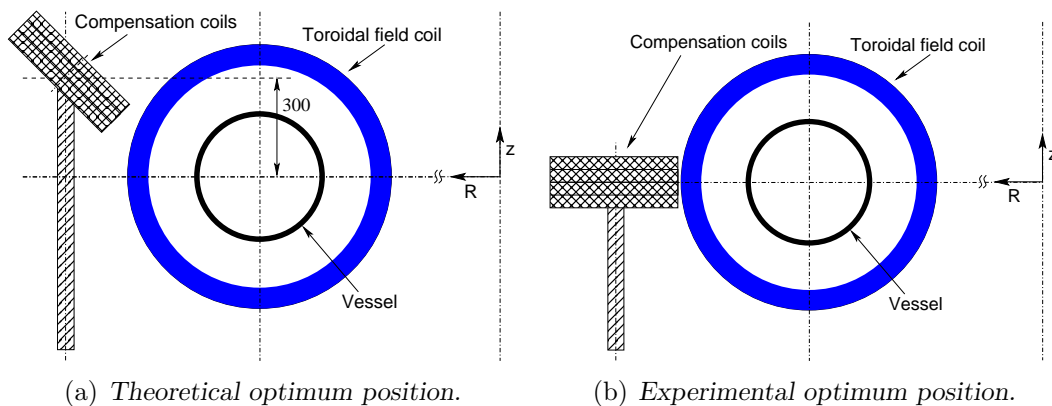


Figure 4.2.4: Placement of the EFCC relative to the plasma vessel. a) Simulations predicted the compensation to be most effective in the shown position, shifted vertically and tilted with respect to the horizontal plane. b) Experimentally it was found that the compensation is most effective when the EFCC is placed at $z = 0$ without tilting.

and those related to different positions of the island chain, e.g. O- and X-point of the island. The discrepancy between theory and experiment shows that the error producing the islands is not fully explained in the code by the displacement as described above.

4.3 Langmuir Probes

Electrostatic probes are one of the fundamental, and in fact one of the oldest, diagnostic techniques for measuring the properties of plasmas. The technique was developed by Langmuir in the 1920's [Lan23; LMS24]. Basically, an electrostatic probe is merely a small electrode inserted into the plasma. Biasing the probe to different voltages and measuring the current-voltage characteristic can provide information about the plasma. The characteristic carries information about density, temperature, electrostatic potential and even the energy distribution function of the electrons (EEDF). Despite the simplicity of the diagnostic principle and the amount of information that can be obtained, probes have a number of disadvantages. Firstly, probes are an invasive diagnostic since material conductors together with a support structure have to be immersed into the plasma. The interaction of the probe with the plasma generally disturbs the plasma. Fortunately the disturbance is typically only local. A further problem, arising mostly in hot plasmas such as in fusion devices, is the high heat load from the plasma which the probe is exposed to. In devices with fusion relevant plasma parameters, probes can in general only be used in the far edge region, because they would immediately be destroyed when entering the hot plasma core. Regardless of, a rather small experiment like WEGA has many advantages. The plasma parameters are moderate enough to allow access of the probes to the whole plasma cross section.

Apart from these more technical aspects the theoretical understanding of Langmuir probes, especially in magnetised plasmas, is a science of its own. The interpretation of probe characteristics and the extraction of plasma parameters from the latter is a rather complicated topic. The difficulty stems from the fact that probes are boundaries to a plasma, and near the boundary the equations governing the motion of the plasma change their character [Che65a].

In the following a brief overview of the interpretation of Langmuir probe characteristics will be given. The principle of operation of Langmuir probes will be explained assuming a non-magnetised plasma with a Maxwellian electron energy distribution function as a simplification. In section 4.3.2 some aspects which are of specific interest for the application of probes in WEGA will be highlighted. For a detailed overview of probe theory see contributions in textbooks (e.g. [Che65a] or [Her89]) or review articles (e.g. [DRR02]).

4.3.1 Principle of Operation

The experimental simplicity of the operation of a Langmuir probe is depicted in fig. 4.3.1. The probe tip, which is in general small compared to the plasma dimensions, is biased to a certain voltage with respect to a reference electrode. The probe characteristic is constructed from the measurement of the probe current at different biasing voltages. In general three voltage levels have to be considered when thinking about the current drawn by a probe in a plasma. The probe tip is biased to the potential U_p with respect to the counter electrode in the electric circuit. This counter electrode is typically the metallic vacuum vessel. Its potential is taken as reference.

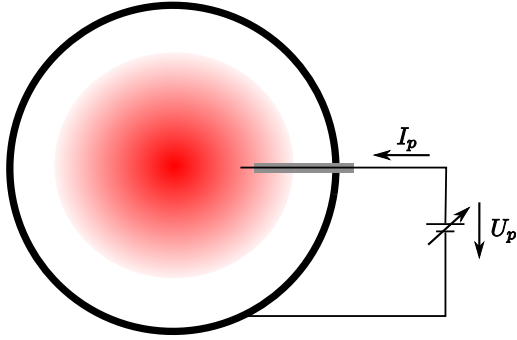


Figure 4.3.1: Simple electric circuit for probe measurements. The probe tip is immersed into the plasma (red). A voltage is applied between the probe tip and the metallic plasma container and the current is measured.

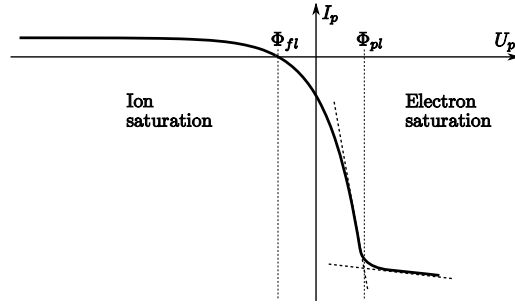


Figure 4.3.2: Ideal IU -characteristic of a cylindrical Langmuir probe in a non-magnetised plasma with Maxwellian energy distribution. An ion current onto the probe is counted positively.

The circuit is closed by the plasma, having itself a certain space potential Φ_{pl} with respect to the reference. The typical shape of a current-voltage characteristic of a Langmuir probe is shown in fig. 4.3.2. If the probe is biased to $U_p = \Phi_{pl}$, there is no electric field surrounding the probe and the charged plasma particles migrate towards the probe because of their thermal velocity. Since electrons move much faster than ions it is predominantly an electron current that is collected by the probe. For $U_p > \Phi_{pl}$ electrons are accelerated towards the probe and ions are repelled. Near the probe there is an excess of negative charge, building up until the positive charge of the probe tip is balanced and the system appears electrically neutral for the rest of the plasma. The layer of charge, called sheath, is typically small compared to the plasma dimensions and therefore, the bulk plasma is undisturbed by the biased probe. The amount of electron current is determined by the number of electrons entering the sheath by thermal motions. The actual shape of the current for positive biasing depends on the sheath thickness which determines the effective collection area A_{eff} of the probe. The relation between A_{eff} and U_p depends on the probe geometry and on external conditions, e.g. magnetised or non-magnetised plasma. In the special case of a planar probe in an non-magnetised plasma A_{eff} is constant, and hence the electron current saturates above Φ_{pl} .

For $U_p < \Phi_{pl}$ ions are accelerated towards the probe and electrons are repelled. Down to a distinct voltage level electrons are still able to overcome the repulsive Coulomb force with their kinetic energy (thermal velocity) and the probe current is a combination of electron and ion current. The voltage at which the total current vanishes, i.e. $I_e = I_i$, is called floating potential Φ_{fl} :

$$\Phi_{fl} = \Phi_{pl} - \frac{k_B T_e}{2e} \ln \left(\frac{2m_i}{\pi m_e} \right). \quad (4.2)$$

In the voltage range $\Phi_{fl} < U_p < \Phi_{pl}$ the current grows exponentially in the cases of

a Maxwellian EEDF:

$$I_p(U_p) = I_{sat,e} e^{\frac{e(U_p - \Phi_{pl})}{k_B T_e}}, \quad (4.3)$$

where

$$I_{sat,e} = en_e A \sqrt{\frac{k_B T_e}{2\pi m_e}} \quad (4.4)$$

is called electron saturation current. $I_{sat,e}$ is the probe current drawn at $U_p = \Phi_{pl}$. A is the probe surface, which in this case equals the effective collection area A_{eff} , because the sheath formation sets on for $U_p > \Phi_{pl}$. From eqn. (4.3) it can be seen, that the slope of a $\log I_p - U_p$ -plot determines the electron temperature of the plasma. At Φ_{pl} the characteristic shows a knee, ($d^2 I_p / dU_p^2 = 0$), which can be used to determine the plasma potential. Φ_{fl} is the potential an insulated electrode would assume in a plasma. For large negative voltages an ion sheath forms around the probe, determining the amount of ion current collected by the probe. The most simple case is again a constant sheath thickness leading to a saturation of the ion current. Due to the much lower thermal velocity of ions the saturated ion current is in general much smaller than the electron saturation current. If the probe is large compared to the ion sheath, the ion saturation current at large negative voltages ($U_p \ll \Phi_{fl}$) is given by:

$$I_{sat,i} = \xi e Z n A \sqrt{\frac{T_e}{m_i}}. \quad (4.5)$$

Z is the charge state of the ions. The factor $\xi \approx 1/2$ accounts for the decreased ion density at the sheath edge due to their acceleration in the presheath [Boh49a]. The exact value of ξ depends on the conditions in the presheath, which can cause the 'saturation' current to increase with U_p [Che01]. $I_{sat,i}$ is typically used to determine the undisturbed plasma density.

4.3.2 A brief Summary of Probe Theory

Probe theory is a complicated topic and the interpretation of probe characteristics is typically not as straightforward as described above. A number of factors have to be taken into account which may alter the probe characteristics and therefore give rise for probe theory modifications. These include amongst others:

- Presence of electric and magnetic fields,
- EEDF deviating from a Maxwellian distribution,
- secondary electron emission,
- probe geometry,
- probe dimensions with respect to plasma scales.

Some aspects of probe theory, which are relevant for measurements in WEGA shall be explained here.

The complicated heating mechanism in the low field operation of WEGA leads to a non Maxwellian EEDF. Mostly in the edge region, where the heating power is deposited, a small fraction of supra-thermal electrons exists. These hot electrons can reach the probe even for large negative voltages where a pure ion current is expected because all thermal electrons are repelled. This leads to a non saturation of the probe current for voltages far below the floating potential. A probe theory, which allows the handling of non Maxwellian EEDF with a small fraction of supra-thermal electrons has been provided by Stangeby [Sta95] (two-temperature model). Evidence for the effect of fast electrons on probe measurements in WEGA has been given by Horvath [Hor+04; Hor05]. The application of Stangeby's theory is valid, if the ion sheath thickness is negligible compared to the probe dimensions. A rough estimation for the sheath thickness h is the Debye shielding length, $\lambda_D = \sqrt{\epsilon_0 k_B T_e / 2n_e e^2}$. But this approximation can underestimate the sheath thickness, which becomes larger for large negative bias. For a collisionless plane sheath h is given by: $h \approx \lambda_D (e(\Phi_{pl} - U_p) / T_e)^{3/4}$ [DRR02].

For WEGA plasmas the Debye length is typically in the order of some 10 μm and the sheath thickness at $U_p = -100$ V is roughly $10\lambda_D$. If the sheath is small compared to the probe dimensions, the effective collection area of the probe is determined by the probe surface. This has actually been the case for the probe diagnostics used in WEGA, which were designed for the measurement of average parameters. Horvath used cylindrical probes with radii $r_p \gtrsim 0.5$ mm [Hor05]. However, for spatially resolved fluctuation measurements the probe construction, including the mandatory support structure for the probe tip, need to be constructed as small as possible, in order to not disturb the plasma significantly. The probe construction specifically designed for this work, ended in cylindrical probe tips with a radius of $r_p = 50$ μm (see sec. 4.4.1). Hence, the probe dimensions are in the order of the sheath thickness. In this case the effective collection area of the probe needs to be corrected for the sheath dimension, which varies with the probe voltage.

The effect of the probe geometry on the shape of characteristics is shown in fig. 4.3.3, where characteristics from cylindrical probes of different radius (0.05 mm and 0.45 mm, respectively) measured in equivalent discharges are compared. The current is normalised to the probe surface. The data is taken from a low field discharge in Argon (Ar). Especially in the plasma centre, where no fast electrons are present, it can be clearly seen how the ion current is affected by the sheath formation. The current density for $U_p > \Phi_f$ is equal for both probe types. In the ion branch, the slope of the current density is much steeper for the small probe. This is because for large negative voltages the probe surface is not the effective collection area anymore. In the edge region, where the heating power is deposited and the fast electron fraction is present, the influence of the probe geometry is less pronounced, because the slope of the ion current density is additionally effected by the fast electrons for both probes.

The ion collection theory in the case of thick sheaths needs to take into account that not all ions entering the sheath are collected by the probe. They undergo orbital motions, similar to a satellite entering the gravitational field of a planet. Depending

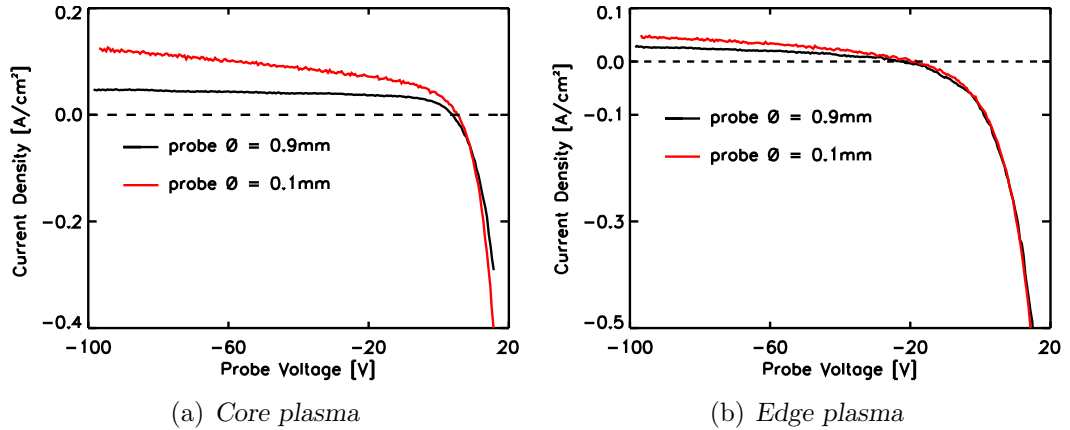


Figure 4.3.3: Current density on different probe geometries in the plasma centre (a) and in the power deposition region (b). Data was measured in Ar discharges at low magnetic field by cylindrical probes of equal length but different probe radius.

on the impact parameter and the kinetic energy ions may pass the sheath or hit the probe. The corresponding theory called orbital motion limit theory (OML) has been developed by Mott-Smith and Langmuir [MSL26]. OML is an oversimplification of the problem of sheath formation, since it is based on assumptions that hold true for only a few rare cases.

For a comprehensive sheath theory, one has to solve Poisson's equations for the local space potential $\Phi(\mathbf{r})$ everywhere from the probe surface to infinity. Allen, Boyd and Reynolds (ABR theory) provided equations to solve the problem self-consistently assuming cold ions ($T_i = 0$) as a simplification [ABR57]. ABR theory is suited for spherical probes, but has been expanded to cylindrical probes by Chen [Che65b]. The assumption of cold ions does not allow orbital motions. All ions are accelerated radially towards the probe. A generalisation for ions of finite temperatures including a proper sheath theory and orbital motions has been provided by Bernstein, Rabinowitz and Laframboise (BRL theory) [BR59; Laf66]. A common result of both ABR and BRL theory is that a saturating ion current can only be expected for probe dimensions, which are large compared to the Debye length ($r_p \gg \lambda_D$).

In order to determine, which probe theory is best suited for the evaluation of probe data measured with small probes in WEGA, the data shown in fig. 4.3.3 has been analysed using ABR, BRL and the Stangeby two-temperature model. Stangeby provides an analytical expression for the probe current $I_p(U_p)$ which can be fitted to experimental data. ABR and BRL theory are based on differential equations, whose solutions have been parametrised by Chen resulting in analytical expressions for the probe current [Che01]. The plasma parameters n , T_e and Φ_{pl} are fit parameters. The two-temperature model has two more fit parameters, reflecting the density and temperature of fast electrons. The quality of the fits does not provide a good benchmark for the validity of a probe theory. All theories provide a reasonably good fit qual-

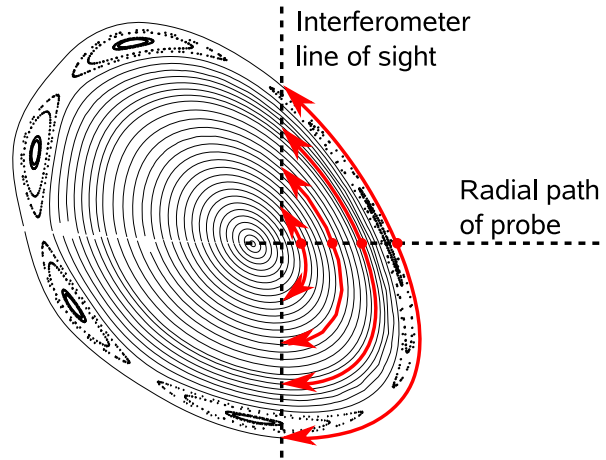


Figure 4.3.4: *The interferometer integrates the plasma density along a vertical line of sight (LOS). The data points of the radial density profiles measured by Langmuir probes are mapped along flux surfaces to the interferometer’s LOS. The line integration of the mapped datapoints should yield the same integrated density in case of correct data.*

ity for data from different regions of the plasma, but result in completely different plasma parameters. The electron temperature is a rather stable fit parameter, since it does not depend on any sheath formation. Radial electron temperature profiles obtained from different probe theories and different probe types agree quite satisfactorily, however strong differences have been found in the plasma density. Using the line integrated density measured by a microwave interferometer (see sec. 4.4.5), density profiles obtained from Langmuir probes can be benchmarked against an independent diagnostic. To this end, density profiles are mapped along flux surfaces to the line of sight of the interferometer and integrated afterwards. The principle of the mapping technique is shown in fig. 4.3.4. It is based on the existence of flux surfaces as isosurfaces for the plasma parameters. All points in the half profile measured by probes can be mapped to the intersection point of the interferometer’s line of sight with the flux surface under consideration.

Assuming the line integrated density measured by the interferometer to be correct, a correction factor γ for the density measured by Langmuir probes can be derived by this technique:

$$\left(\int n dl\right)_{interferometer} = \gamma \left(\int n dl\right)_{probe}. \quad (4.6)$$

The comparison of different probe theories and geometries leads to correction factors, which are summarised in the following table:

	ABR	BRL	Stangeby
$r_p = 0.05$ mm	$\gamma = 2.3$	0.67	0.01
$r_p = 0.45$ mm	1.75	0.63	0.24

The most striking result is, that, the two-temperature model applied to the small probe with the comparable thick sheath leads to an overestimation of the density by about two orders of magnitude. This can be accounted for by the underestimation of the effective collection area of the probe by the model, as it does not consider any finite sheath thickness. The ABR fits lead to the most reasonable results. Here, $\int n dl$ from the probes is actually smaller than the interferometer signals. This is reasonable, because probe measurements generally disturb the plasma. The perturbation can be seen as a drop in the interferometer's signal, when the probe penetrates the plasma. Since γ is derived from a comparison to the undisturbed plasma, it has to be greater than unity. From this comparison it can be concluded that ABR theory provides reasonable results for density and electron temperature. Caution is advised concerning the plasma potential. Here, not only the absolute values from different theories differ, but also the overall shape of the profile. Even the sign of the radial electric field, which is derived from $E_r = -d\Phi_{pl}/dr$, is not unique. Horvath has shown that the two-temperature model leads to reasonable results for Φ_{pl} with thick probes. However, for the thin probes, designed for fluctuation studies, Φ_{pl} is an unstable fit parameter. The sheath models lead to stable fits, but they don't pass a simple crosscheck with another method to derive Φ_{pl} , namely from eqn. (4.2): $\Phi_{pl} = \Phi_{fl} + \frac{k_B T_e}{2e} \ln\left(\frac{2m_i}{\pi m_e}\right)$. Φ_{fl} can be directly measured and T_e is a robust fit parameter. There is a striking qualitative discrepancy between Φ_{pl} profiles obtained from the two methods, at least for the low field case. In high field operation, the two methods agree quite well, except for a constant offset in the plasma potential.

The following conclusions can be drawn from the conducted comparison of different probes and theories:

- Fluctuation measurements necessitate the construction of small probes, with dimensions in the order of the sheath thickness for ion collection.
- T_e can easily be obtained from probe characteristics. The results are more or less independent of the probe geometry and the applied probe theory, because T_e is derived mainly from the exponential part of the $I_p - U_p$ -curve between Φ_{fl} and Φ_{pl} .
- n is derived from the ion collecting part of the characteristic, which is strongly affected by fast electron populations and sheath formation. The results from the ABR theory agree satisfactorily with the line integrated density measured independently by an interferometer.
- For low field operation it is not reliable to obtain the plasma potential from a fit of probe characteristics. An estimation from Φ_{fl} and T_e can be used to get an idea about the profile shape, but not for absolute values.
- For high field operation it is reasonable to treat the plasma potential as a fit parameter.

4.3.3 Fluctuation Measurements using Langmuir Probes

Using Langmuir probes it is possible to measure fluctuations in density, temperature and plasma potential simultaneously with high spatial resolution. To this end, probe characteristics have to be measured on time scales, which are much smaller than the shortest fluctuation time scales of interest. However this is a technical challenge. On the time scales of interest (see sec. 4.4.3) measurements may be strongly affected by parasitic capacitive loads giving rise to displacement currents limiting the bandwidth of the system [Gia+94]. A technical solution to overcome this problem is placing the amplifier in close proximity to the probe tips [Pfe+98; SET07]. A common simple approach to measure fluctuations with Langmuir probes is to operate the probes only at two working points, namely to measure I_{sat} at large negative biasing voltages and Φ_{fl} . In this approach temperature fluctuations are assumed to be negligibly small ($\tilde{T}_e \approx 0$). The fluctuating parts of eqn. (4.2) and (4.5) are then a measure for $\tilde{\Phi}_{pl}$ and \tilde{n} , respectively:

$$\tilde{I}_{sat} \propto \tilde{n} \quad \text{and} \quad \tilde{\Phi}_{fl} \propto \tilde{\Phi}_{pl}. \quad (4.7)$$

This is in general an erroneous approach, which is in first principle motivated by a lack of better knowledge. The error, which is introduced by this method has been studied by comparison with results from fast swept Langmuir probes and independent diagnostics, where many of the results from statically biased probes have been confirmed [End99]. The statistical properties of fluctuations and their spatio-temporal structure are especially well reproduced. Concerning absolute values of turbulent transport, Schubert has shown, that a phase shift between temperature and density or potential fluctuations significantly contributes to turbulent particle as well as energy flux [Sch05].

In this work, the simple approach of eqn. (4.7) has been chosen, since the object of the studies is mainly a qualitative characterisation of turbulence in WEGA.

4.4 Diagnostic Setup

A Langmuir probe system, suitable for spatio-temporally resolved fluctuation measurements, had to be designed and constructed for this work. The boundary conditions for the design are given mainly by the limited access to the plasma entering the vacuum vessel through circular ports with a diameter of ≈ 9 cm. The aim is to get diagnostic systems which provide a three-dimensional view into the structure of turbulent fluctuations. The required resolution of the system is estimated according to typical spatial and temporal scales resulting from drift wave theory for plasma parameters in WEGA.

4.4.1 Poloidal Probe Array

From a single Langmuir probe local information about fluctuations can be obtained. The spatial resolution is only limited by the dimension of the probe tip plus the sheath forming around the probe tip. Using multiple Langmuir probes one can obtain spatially resolved information about fluctuations. To this end, an array of probes has been designed for poloidally resolved measurements of fluctuations in WEGA. Poloidally resolved means that the probe tips are aligned to the flux surfaces in the plasma edge region around the LCFS, as can be seen in fig. 4.4.1. The array is constructed of 13 probes with a vertical distance of 0.5 cm. This probe distance has been chosen according to an estimation of the expected scale length of fluctuations in WEGA. Experiences from other experiments show that in wavenumber space most of the power is in the range below $k\rho_s \leq 0.15$ [Lie85]. For gyrotron heated hydrogen discharges at 0.5 T in WEGA the drift parameter is in the range of $\rho_s \approx 0.1$ cm. Following the Nyquist sampling theorem the highest wavenumber to be resolved is $k_{max} = \frac{\pi}{d}$ where d is the probe distance. In that case with the chosen distance of 0.5 cm the spectrum can be resolved up to $k\rho_s \approx 0.6$. Under all other discharge conditions but hydrogen at 0.5 T larger scales or smaller wavenumbers, respectively, are expected. The number of probe tips is limited by the width of the port that is used to insert the array into the plasma vessel. Fig. 4.4.2 shows a photo of the array. It is installed on a pneumatically driven fast reciprocating manipulator performing a radial scan within about 2 s. In a radial scan the blue shaded region shown in fig. 4.4.1 is covered by the array.

The probes tips are cylindrical tungsten wires with a diameter of $100 \mu\text{m}$ and a free length of 3 mm. To prevent crosstalk between neighbouring probes they are individually shielded by a grounded stainless steel tube ending a few mm before the probe tip. The shield is covered by ceramics preventing short circuits inside the plasma and ensuring survival of the heat load when penetrating into the plasma. Fig. 4.4.3 shows details of the probe construction.

4.4.2 Toroidally Resolved Measurements

In order to characterise the dynamics of fluctuations parallel to the magnetic field, toroidally resolved measurements are necessary. To this end at least two probes

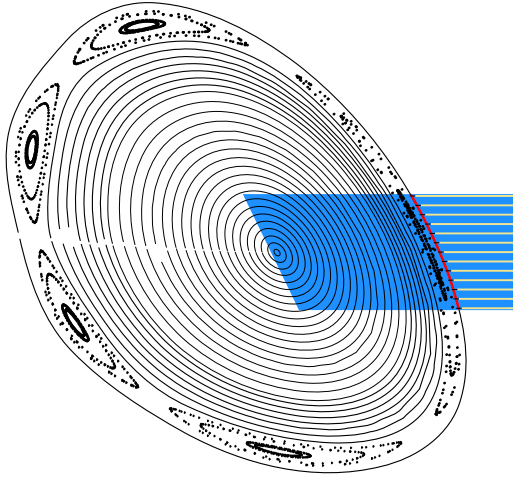


Figure 4.4.1: Sketch of the poloidal probe array. The probe tips are aligned to the magnetic flux surfaces for low t ($t_0 \lesssim 0.3$) in the edge region. The blue shaded region is accessible with the array in a radial scan.

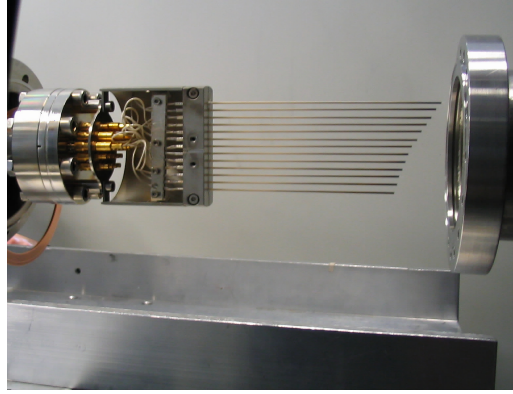


Figure 4.4.2: Photo of the poloidal array mounted on a fast reciprocating manipulator taken outside the vacuum vessel. The probe shafts made of ceramics are designed long enough for the massive metallic probe holder not to enter the plasma column.

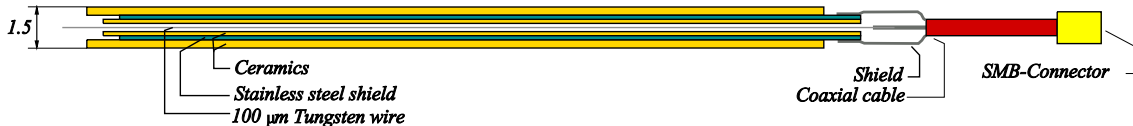


Figure 4.4.3: Schematic drawing of the probe construction used for fluctuation measurements. The outer diameter of the probe shaft is only 1.5 mm. The whole construction is a set up of three nested tubes with the tungsten wire forming the probe tips fed through the innermost ceramics tube. A stainless steel tube acting as an electrostatic shield is connected to the ground potential (shield of connecting coaxial cables). The probe tip may not be in contact with the outer ceramics, because this will be coated with conducting material after some time of plasma operation. To prevent a direct contact of the coated ceramics with the probe tip, the ends of the tubes are displaced against each other by a few mm in order to form a kind of labyrinth for the coating material.

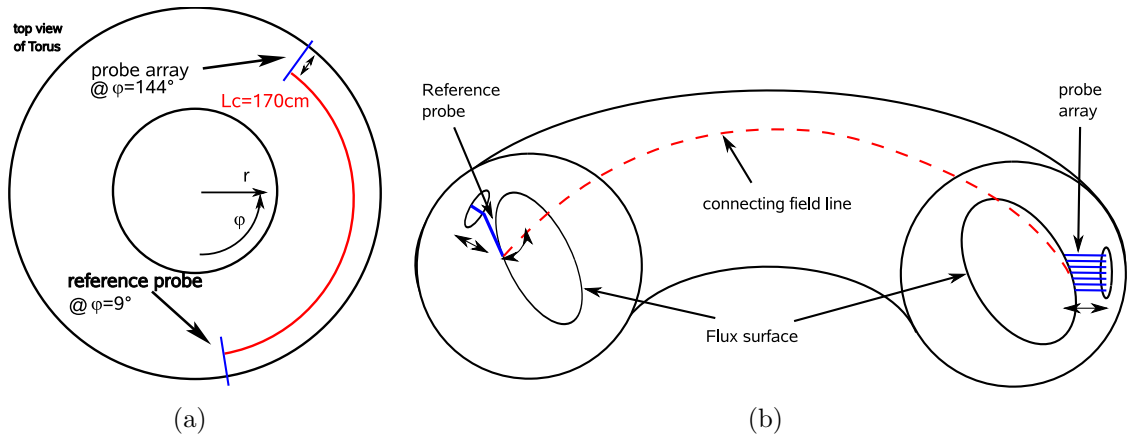


Figure 4.4.4: Geometry of the probe setup for toroidally resolved measurements. a) Topview of the WEGA torus showing the toroidal position of the two probe diagnostics. Reference probe and array are separated from each other by $\Delta\varphi = 135^\circ$. b) A field line starting at the reference probe intersects one of the array's probe tips at a certain radial position. The shaft of the reference probe has to be tilted after entering the vessel in order to find such connecting field lines.

must be placed on one field line with a distance parallel to \mathbf{B} in the range of the toroidal scale length which is expected to be much longer than the perpendicular scale length ($k_\perp \gg k_\parallel$). This expectation could be confirmed in other experiments where correlation lengths in the range of several meters have been found ([Rud90; Ble98; Tho02]). In WEGA for toroidally resolved measurements the probe array is used together with an additional reference probe which is separated from the array by $\Delta\varphi = 135^\circ$ in toroidal direction. The reference probe is installed on a slowly moving radial manipulator. For more flexibility in the positioning of the reference probe, a mechanism has been installed which allows the whole probe to be tilted after inserting it into the vacuum vessel. Together with the radial motion this allows a two dimensional scan in the poloidal plane. Fig. 4.4.4 (a) shows the toroidal position of the two diagnostics in a top view of the torus. The challenge now is to find a position, where a field line starting at the reference probe intersects the path of the array after a toroidal distance which will be referred to as connection length L_c in the following. The geometry is illustrated in fig. 4.4.4 (b). The three-dimensionality of the magnetic topology in a stellarator introduces strong limitations to the number of configurations and positions where such connecting field lines can be found. Field line tracing calculations predicted their existence for the short connection length of $L_c = 170 \text{ cm}$ as shown in fig. 4.4.4 (a). In section 5.3.2 the experimental evidence for these predictions will be given.

4.4.3 Data Conditioning and Acquisition

As described in section 4.3.3 a common technique to measure electrostatic fluctuations with Langmuir probes is to operate them at two stationary working points

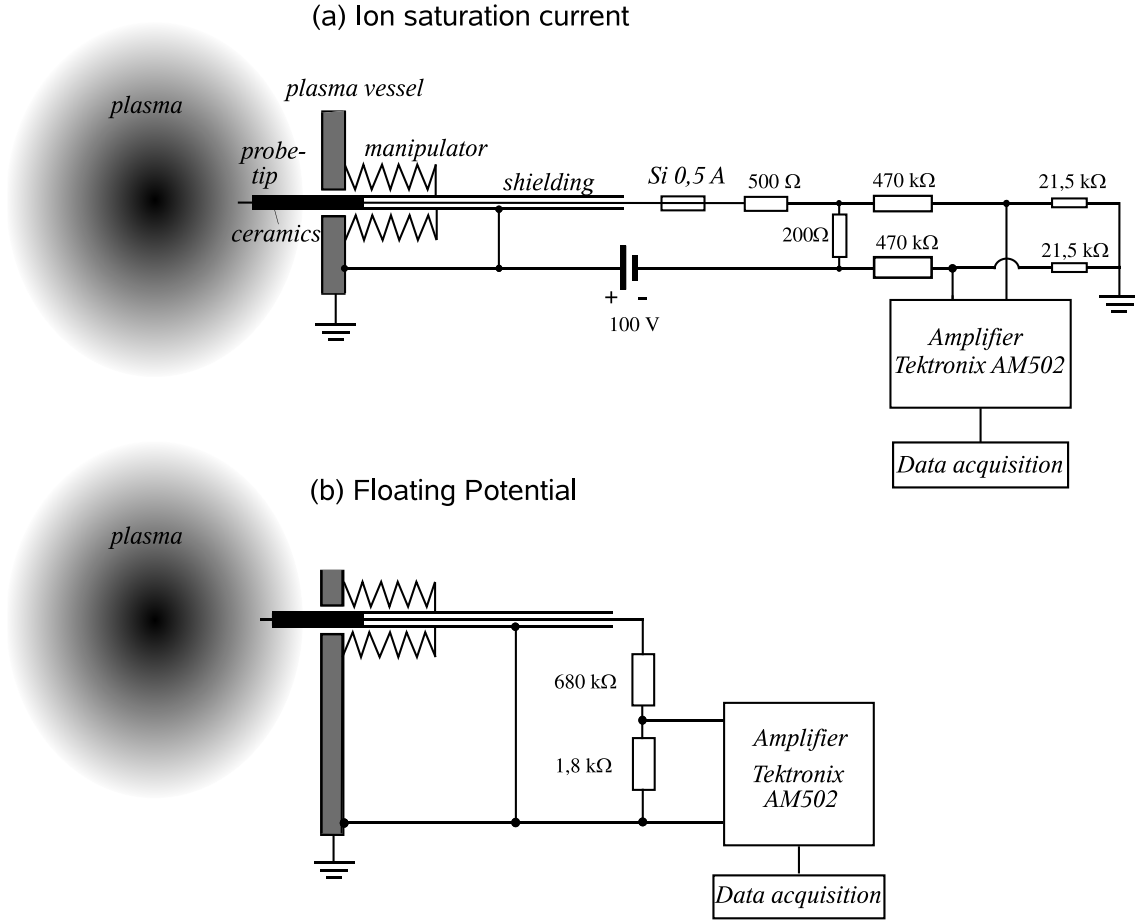


Figure 4.4.5: Electrical circuits for measuring I_{sat} (a) and Φ_{fl} (b), respectively.

only and to measure \tilde{I}_{sat} and $\tilde{\Phi}_{\text{fl}}$, respectively. To measure I_{sat} the probes are stationary biased at $U_B = -100\text{V}$ with respect to the vacuum vessel. The potential of the grounded vacuum vessel is taken as reference potential for all measurements. The current is measured by a $200\ \Omega$ resistor. Fig. 4.4.5 (a) shows the electrical circuit used to measure I_{sat} . The voltage dividers are necessary to get rid of the high common mode voltage at the input of the differential amplifiers used as amplifiers and anti-aliasing filters. Φ_{fl} is measured when the probes are terminated at a high-impedance and therefore cannot draw any significant currents. Again a voltage divider is used because $|\Phi_{\text{fl}}|$ can rise up to values that would destroy the amplifiers (fig. 4.4.5 (b)). All data are sampled synchronously by two PC-based data acquisition systems with eight 12 bit ADC channels each. The systems provide an analog bandwidth of 50 MHz and similar sampling rates. However, the temporal resolution of the diagnostic system is designed for frequencies up to some 100 kHz. From the dispersion relation of drift waves and typical WEGA parameters, the drift wave frequency at a spatial scale of $k_{\theta} = \rho_s^{-1}$ is in the order of about 50 kHz. The typical sampling rate for data in this work is $\nu_s = 1.5625\ \text{MHz}$. The -3 dB frequency of the

used anti-aliasing filters has been set to 300 kHz in order to reduce high frequency noise, because no fluctuating power above the noise levels is expected at such high frequencies.

4.4.4 Reconstruction of Turbulent Structures in the Poloidal Plane

As detailed in section 4.4.1 the probe array is mounted on a fast reciprocating manipulator. This manipulator performs a radial scan in about 1 s. Using the reference probe together with the array it is possible to reconstruct averaged turbulent structure in the region of the poloidal plane that is covered by the array. To this end the time traces taken in a radial scan are divided into subwindows to get a radial resolution. A scan is typically divided into 20-30 slices of 20-40 ms each, or 30000-60000 samples, respectively. During that time the manipulator moves by 2-4 mm giving a sufficient spatial resolution. Thus a grid of time traces is produced in the covered region. The grid will be referred to as the *matrix* in the following. Turbulent structures are now reconstructed by calculating the CCF between each subwindow of the matrix and simultaneously sampled subwindows of data from the reference probe. To make data from different regions along the pressure gradient comparable, all subwindows are normalised to their fluctuation amplitude prior to the correlation analysis.

4.4.5 Microwave Interferometer

A single channel Mach-Zehnder interferometer is used to measure the line-integrated electron density at WEGA. The interferometer measures the phase shift between a wave passing the plasma and a reference wave. This phase shift is introduced by the dependence of the refractive index of waves propagating in a plasma on the plasma frequency $\omega_p = \sqrt{(n_e e^2 / \epsilon_0 m_e)}$. Assuming zero phase shift without plasma the plasma introduces a total phase shift of

$$\phi = \frac{e^2}{4\pi\nu\epsilon_0 m_e} \int_{l_0}^{l_1} n dl, \quad (4.8)$$

where ν is the frequency of the probing wave and l is the path of the signal wave. At WEGA a microwave at a frequency of $\nu = 80.605$ GHz is launched into the vessel in O-mode along a vertical line of sight at $R = 73$ cm. The cutoff density for this frequency above which the wave cannot propagate in the plasma anymore is $n_c = 8 \cdot 10^{19} \text{m}^{-3}$. The interferometer is one of the standard diagnostics providing an immediate view of the discharge evolution. In this work it has also been used to crosscheck and calibrate equilibrium density profiles obtained from Langmuir probes (see section 4.3.2).

4.5 Equilibrium Profiles

To understand the results of fluctuation measurements, some understanding of the background equilibrium plasma parameters is necessary. To this end radial profiles of plasma parameters obtained from swept Langmuir probe measurements are presented in the following section. Detailed studies of WEGA plasmas have been performed in earlier works [Hor05], so only some examples for discharge conditions relevant for fluctuation studies are presented. Two different scenarios are considered:

Low field operation Magnetron operation at $B_0 = 57$ mT where the plasma is heated at the edge by electrostatic Bernstein waves at a frequency of 2.45 GHz.

High field operation Gyrotron operation at $B_0 = 500$ mT with ECRH at 28 GHz resulting in central power deposition.

The terms *low field* and *high field* will be used subsequently to distinguish the two operational regimes.

4.5.1 Magnetron Operation at 57 mT - Low Field

In this scenario most ECRH power is deposited near the LCFS as a result of the complex heating scenario described in section 4.1. The result is typically a hollow temperature profile. The hollow shape of the bulk electron temperature profiles is caused by a small fraction of supra-thermal electrons which are produced by the heating mechanism in the plasma edge heating the bulk electrons by collisions [Hor+06]. Fig. 4.5.1 shows some typical profiles of plasma parameters for He discharges at low field at a rotational transform of $t_0 = 0.182$. Data was measured with one probe of the array. The drop in floating potential near the LCFS is a typical feature of WEGA plasmas, besides the hollow temperature profile.

The individual graphs in fig. 4.5.1 represent the plasma response to a change in the neutral gas pressure. The neutral pressure has been varied from $p_n \approx (2 \dots 4) \cdot 10^{-3}$ Pa. The strongest effect of this variation can be seen in the plasma density. With decreasing neutral pressure the density profiles are getting steeper as the core density increases. As shown in figure 4.5.2 the effect of increasing density can also be seen in the line integrated density measured by the interferometer. This can be explained by a better heating efficiency at lower neutral pressure due to the higher ionisation degree going together with a reduced plasma resistivity. At the same time the density increases and higher electron temperatures are observed. The response to a change in neutral pressure may affect turbulence in two ways. First, collisionality plays a role for the stability of drift waves. As explained in section 2.3.2 every dissipative mechanism leads to a phase shift between density and potential fluctuations. Second, the density gradients in the edge region are significantly different during this neutral pressure scan. A reduction of neutral pressure leads to a steepening of gradients. This can be described by the density gradient length $L_n = \frac{\nabla n_e}{n_e}$. Looking at a radial position of about 5 mm inside the

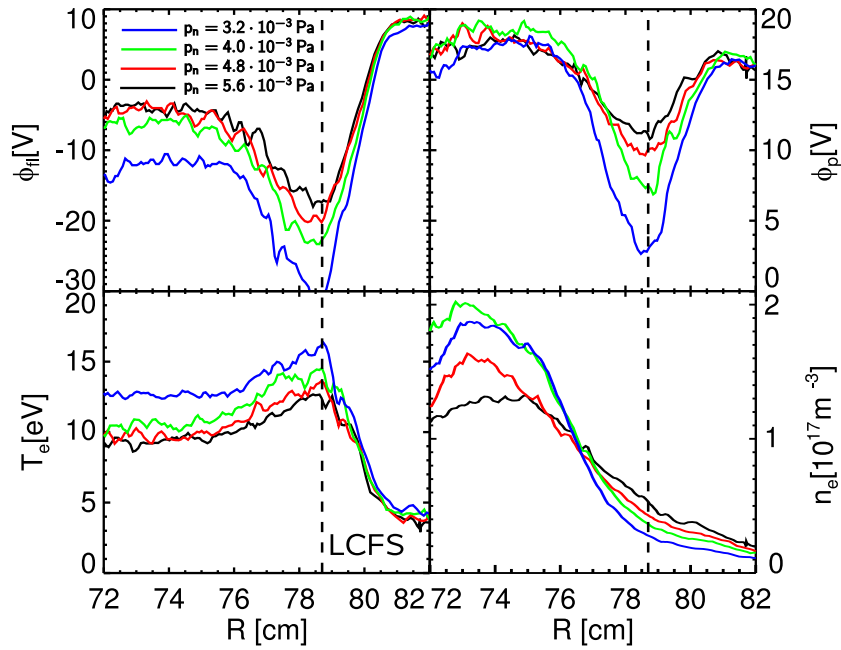


Figure 4.5.1: Typical profiles of equilibrium plasma parameters obtained from swept Langmuir probes measurements in low field operation. Data was measured in He discharges at $t_0 = 0.182$. The individual lines correspond to different neutral pressures during the discharge. The density drop in the centre is due to the plasma perturbation from the probe penetration.

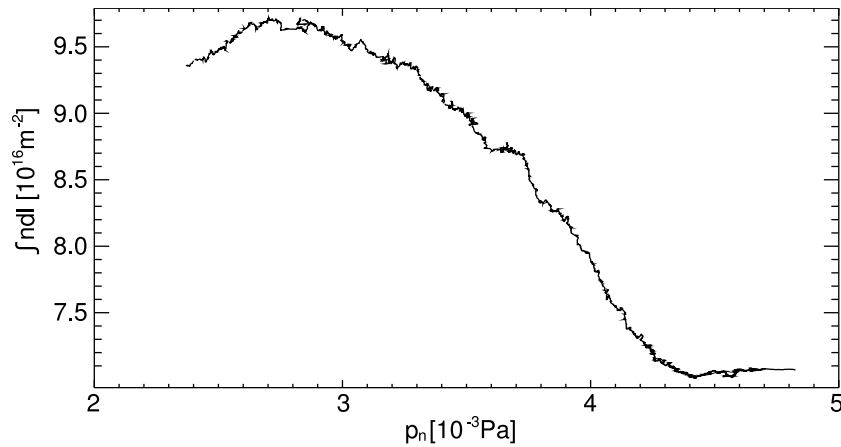


Figure 4.5.2: Plasma response to a variation in the neutral pressure in the low field operation. In a certain range the line integrated density decreases with increasing neutral pressure.

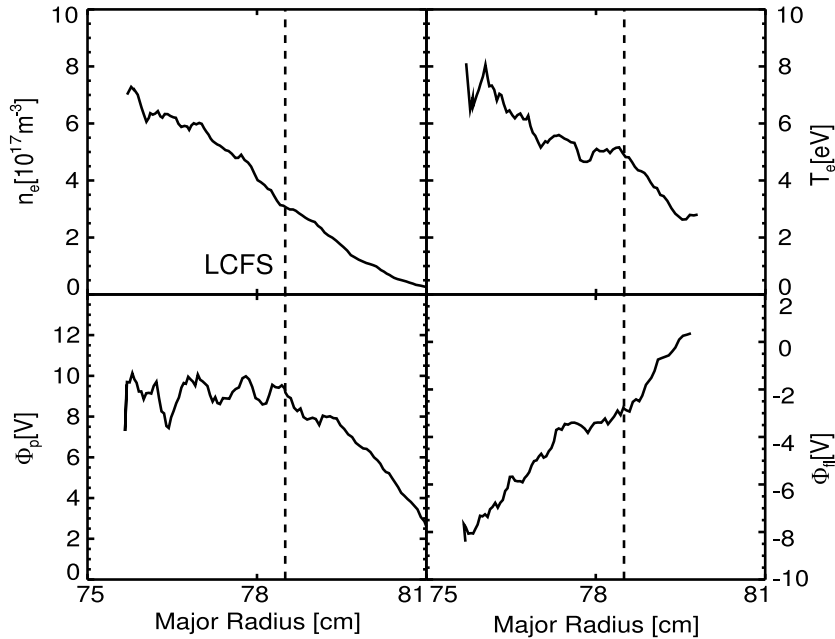


Figure 4.5.3: *Equilibrium profiles of plasma parameters obtained from Langmuir probes in high field operation. Data was measured in He discharges at $t_0 = 0.182$. The plasma centre is not accessible with Langmuir probes because they start emitting electrons due to the high heat load.*

LCFS L_n is varied from 2 cm to 4 cm during the neutral pressure scan shown in figure 4.5.1.

4.5.2 Gyrotron Operation at 500 mT - High Field

A different operational regime is obtained at $B_0 = 500$ mT where the plasma is heated by ECRH at 28 GHz. The short wavelength in comparison to the plasma dimensions allows a local resonant power deposition in this regime. The beam waist of the launched X2 mode is located near the magnetic axis. Adjusting the magnetic field strength to match the resonance condition for electrons at the magnetic axis, the heating power can be deposited centrally. An example of plasma parameter profiles obtained from swept Langmuir probe measurements in a He discharge is shown in fig. 4.5.3. The plasma centre was not accessible with the installed probe systems for the discharge conditions considered here. When entering the plasma centre the probe tips were heated by the plasma up to temperatures where they started emitting electrons rendering the data unusable. However, for more moderate conditions in Ar discharges, centrally peaked profiles were obtained [Ott+07b]. Since the heating scenario is not sensitive to changes in parameters like heating power or discharge gas but only to the magnetic field configuration, centrally peaked profiles are assumed to be a general feature of plasmas in the high field case. Maximum

achievable plasma parameters were estimated based on scaling laws, leading to expected peak temperatures up to $T_e < 100$ eV in low density H₂ plasmas [Laq+07] and peak densities up to the cut-off density, $n \lesssim 5 \cdot 10^{18} \text{ m}^{-3}$, at lower temperatures.

The plasma density in the high field operational regime is typically by about one order of magnitude higher than in the low field case at comparable neutral pressures. Hence, the ionisation degree of the plasma is much higher at high field. The plasma at high field is almost fully ionised resulting in negligible neutral collisions.

4.5.3 Typical Plasma Parameters

A list of typical plasma parameters for the two operational regimes is given in the subsequent table. All values are estimated for the plasma edge, where fluctuations are studied. The list does not give any accurate absolute values but only some typical orders of magnitude, in order to get a feeling for the boundary conditions, under which fluctuations are investigated.

	low field	high field
B_0 [mT]	57	500
n [m^{-3}]	$10^{16} \dots 10^{17}$	$10^{17} \dots 10^{18}$
T_e [eV]	10 ... 15	5 ... 10
T_i [eV]	1	
$v_{Dia,e}$ [m/s]	10^3	10^2
v_A [m/s]	10^6	$10^6 \dots 10^7$
$v_{th,e}$ [m/s]	10^6	10^6
c_s [m/s]	10^4	10^4
$\nu_{e,i}$ [s^{-1}]	$10^4 \dots 10^5$	$10^5 \dots 10^6$
$\nu_{e,n}$ [s^{-1}]	$10^4 \dots 10^5$	10^4
α	0.1	0.5 ... 1
β	10^{-4}	10^{-5}
$R_{L,e}$ [m]	10^{-4}	10^{-5}
$R_{L,i}$ [m]	$5 \cdot 10^{-3} \dots 10^{-2}$	10^{-3}
L_n [m]	10^{-2}	10^{-2}
λ_D [μm]	10	10

Chapter 5

Characterisation of Fluctuations

The following chapter gives a characterisation of electrostatic fluctuations in the WEGA stellarator. Raw data from turbulent plasmas is analysed by statistical methods and systematically scanned for properties that can identify the driving instability mechanism. Step by step the view into the structure of turbulence will be expanded starting with temporally resolved measurements at fixed positions, and ending with a three-dimensional picture describing the dynamics of turbulence perpendicular and parallel to the magnetic field.

5.1 Characterisation of Fluctuations in the Temporal Domain

5.1.1 Dependence of Fluctuation Properties on the Magnetic Topology

Since this is the first work dealing with fluctuations in WEGA, no prior knowledge about fluctuation levels and the grade of turbulence under various discharge conditions was available. The very first step in the characterisation process was to find working points where plasmas with fully developed turbulence can be studied, which is actually the intention of this work. Despite the rather common observation of plasmas in toroidal magnetic confinement devices being in a state of fully developed turbulence, it was found that this is not generally the case in WEGA. Fully developed turbulence means, that fluctuations appear in a broad range of spatial and temporal scales. This state will be labelled high grade of turbulence in the following. In Fourier space A high grade of turbulence becomes manifest as a broad distribution of power in wavenumber and frequency. Wavenumber and frequency spectra are related to each other by the dispersion relation of the underlying instability. Because of technical constraints in the experimental setup, frequency spectra are much easier to obtain and with a much higher spectral resolution than wavenumber spectra. As described in section 3.3.1 the spectral resolution is limited by the number of points in the raw dataset to be analysed, which is in case of spatially re-

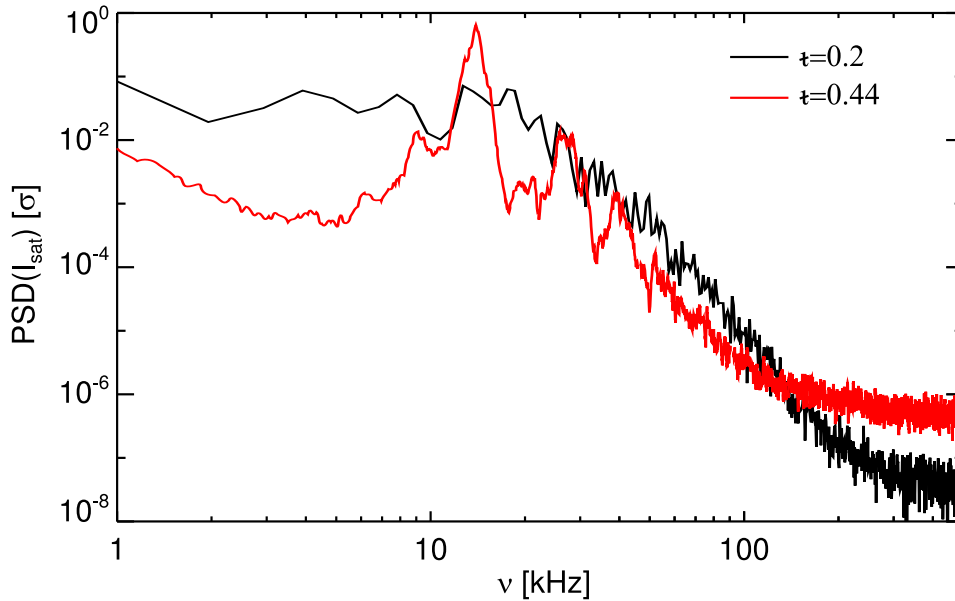


Figure 5.1.1: Autopower spectrum of density fluctuations for a He discharge at low magnetic field for different t configurations. At $t_0 \approx 0.44$ the spectrum is dominated by distinct peaks reflecting coherent modes. At $t_0 \approx 0.2$ fully developed turbulence is found. The spectrum is flat up to some 10 kHz and decays following a power law for higher frequencies. The signal power is in both cases normalised to the corresponding fluctuation amplitude.

solved data the number of channels available. For time traces it is in principle only limited by the memory depth of the acquisition system and is therefore typically several orders of magnitude higher than for spatially resolved signals. This is the reason why frequency spectra are analysed in order to find turbulent plasmas.

The great flexibility of WEGA's magnetic configuration has been described in section 4.2. A scan through this dimension of the parameter range is the first approach to identify plasmas with a high grade of turbulence. The rotational transform t can be varied in a wide range from $t \approx 0.1 \dots 1$ in the low field case because there is in principle no technical limitation for the helical field coil current, which determines t at a given toroidal field following eqn. (4.1). $t = 1$ is taken as upper limit because of the destruction of closed magnetic surfaces by error fields¹. Typical values are in a range of $t \approx 0.2 \dots 0.6$. In this range frequency spectra are compared with the attention to the shape of the spectrum. Eqn. (3.11) was applied to time traces of \tilde{I}_{sat} measured by a single probe located in the plasma edge about 1 cm inside the LCFS. Averaging was realised by splitting time traces of typically 2^{16} samples in 16 sub-windows. The result of this scan was that turbulent broad band spectra are generally found for $t < 0.3$ at low field. An example for a power spectrum of density

¹At $t = 1$ multiple resonances coexist (1/1, 2/2, 3/3,...) and thus lead to destruction of magnetic surfaces.

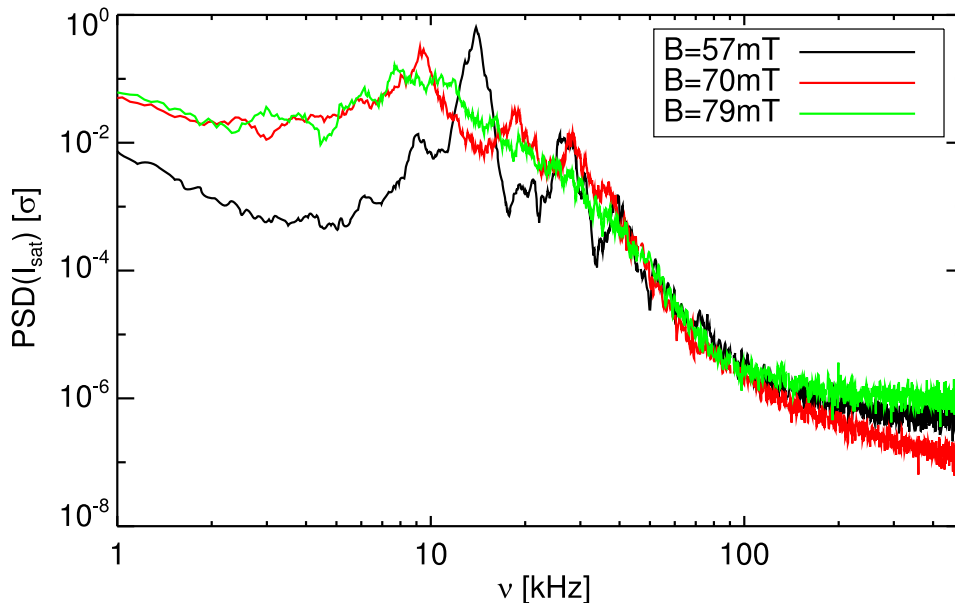


Figure 5.1.2: *The coherent modes observed in low field operation at $t_0 \approx 0.44$ can be destabilised by increasing the magnetic field strength. Increasing B from 57 mT to 79 mT the spectrum becomes broader and the peaks are less pronounced. The t configuration was kept fixed for the different field strengths. The signal power is in all cases normalised to the corresponding fluctuation amplitude.*

fluctuations at low field and $t_0 = 0.182$ can be seen in fig. 5.1.1 (black line). In this case no distinct lines marking coherent modes can be found in the spectrum. The shape of the spectrum is flat up to about 20 kHz and decays following a power law for higher frequencies as expected for turbulence. The flattening in the spectrum above 100 kHz is due to noise, dominating the signal for such high frequencies. The fluctuation power is too low to be detectable in this region. The red line in fig. 5.1.1 shows an example for an increased helical field at $t = 0.44$. It can be clearly seen that the spectrum is dominated by a coherent mode at $\nu \approx 15$ kHz with a small bandwidth of $\Delta\nu/\nu \ll 1$. Additionally, the first and second harmonic of this mode appear in the spectrum. The turbulent broadband background is still present for high t but its intensity compared to the coherent mode is much smaller than for low t . Both signals are normalised to their standard deviation in order to make the amplitudes comparable. In case of high t it was also possible to reach turbulent states as shown in fig. 5.1.2. Here, the development of the spectrum shape for $t = 0.44$ is shown when the magnetic field strength is increased. In this scan the toroidal magnetic field was increased from 57 mT which is the default value, up to 79 mT. The ratio I_H/I_T , and hence the rotational transform was kept constant. With increasing field stronger developed turbulence was observed.

The character of the observed coherent modes has not been further investigated. The transition from coherent drift modes to turbulence and the control of turbu-

lence has been studied elsewhere [Kli+97; Gra+99]. However, an important control parameter for the destabilisation of drift waves and the transition to turbulence is the ratio of the perpendicular density gradient length to the drift scale, L_{\perp}/ρ_s [W GK06]. This is consistent with the results presented here.

Magnetic configurations with rotational transform $t < 0.3$ were chosen as working point for all further turbulence studies. To be more specific two special configurations were selected. A configuration with $t_0 = 0.182$ is one of WEGA's default limiter configurations. For this configuration flux surface measurements with error field compensation have been undertaken (see sec. 4.2.1). The second configuration with $t_0 = 0.224$ was used for toroidally resolved measurements because here connecting field lines between reference probe and the matrix could be found.

5.1.2 Radial Profiles of Fluctuation Amplitude

The turbulent plasma states identified before were characterised starting with the relatively simple analysis of the fluctuation amplitude.

The amplitude of fluctuations σ is defined as the integral spectral power and is equivalent to the standard deviation of a signal. Radial profiles of σ were compared to equilibrium profiles in order to get an idea about the source of free energy driving turbulence. In order to limit the number of free parameters this was done under the well-founded assumption that drift waves are driving turbulence. Drift waves are driven by the density gradient and thus it was expected to find strongest fluctuations in the region of the gradient. This could be checked by comparing profiles of density fluctuations to mean density profiles. The result of such an experiment is shown in fig. 5.1.3. Standard deviation σ and mean value μ of I_{sat} are plotted against the effective radius. I_{sat} was chosen instead of n_e because mean and fluctuating part can then be evaluated from the same dataset. This approach is justified because the shape of the density profile is not altered significantly when the electron temperature is additionally taken into account ($I_{\text{sat}} \propto n_e \sqrt{T_e}$). In case of a flat density profile (red squares) it is obvious that density fluctuations are strongest at the plasma edge where the density gradient is located. This statement is of course not strong enough to identify the density gradient as free energy to drive turbulence in WEGA. To confirm this another configuration was chosen, where for similar boundary conditions a different shape of equilibrium profiles was found. For the observed low field case this could be done by changing the neutral pressure p_n during the discharge. A reduction of p_n leads to an increased plasma density as shown in section 4.5.1. This goes together with more peaked density profiles as shown in fig. 5.1.3 (black diamonds). In this case a high fluctuation amplitude was found in a broader radial range. This result shows that a significant density gradient is necessary to drive turbulence. But in case of the peaked density profile it could also be shown that ∇n_e is not the only source of free energy. For $r_{\text{eff}} \gtrsim 5$ cm the fluctuation amplitude continuously increased although the gradient was more or less constant. A reasonable explanation for this effect was found in the magnetic shear profile given by WEGA's magnetic configuration. It is known that magnetic shear is capable of stabilising drift waves

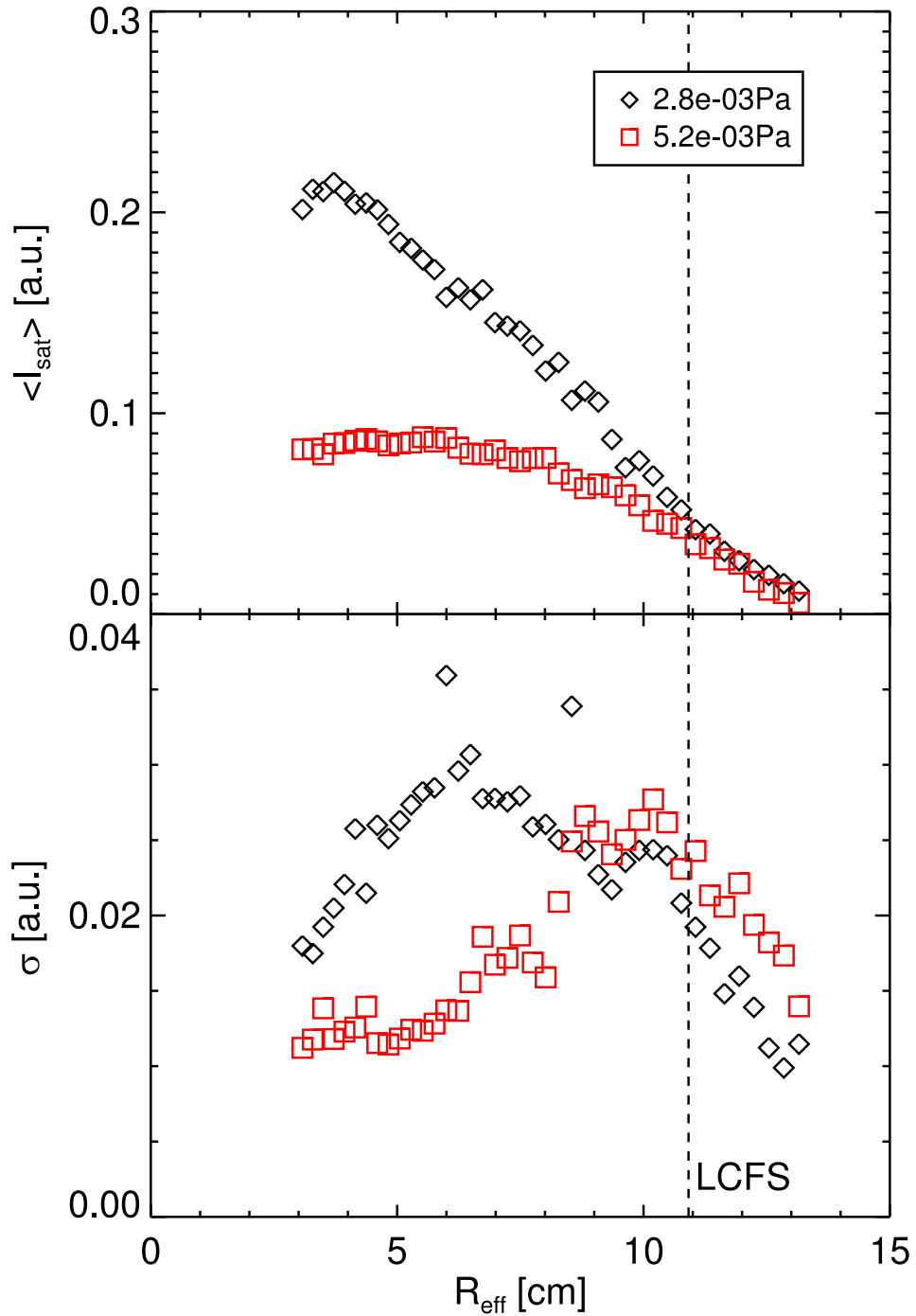


Figure 5.1.3: Radial profile of the mean value and the standard deviation (fluctuation amplitude) of I_{sat} for different neutral pressures, measured at low field. p_n is obviously an effective way to manipulate the density gradient.

[Tsa+78] and thus may lead to a reduced fluctuation amplitude. WEGA's field topology shows an increasing shear towards the plasma edge. The observation of increasing fluctuation amplitude deeper in the plasma was also found for high field operation. However, a comparison between different profile shapes under similar boundary conditions could not be performed here. The shape of density profiles was always more or less centrally peaked and experimental access is only given up to $r \approx a - 3$ cm. Deeper insertion increases the risk of damaging the probes by the high heat load from the plasma.

5.1.3 Cross-Phase Spectra

Important information about the underlying instability mechanism driving turbulence can be gained from the phase relation between density and potential fluctuations. To this end \tilde{I}_{sat} and $\tilde{\Phi}_{\text{fl}}$ were simultaneously measured by neighbouring probes. In case of turbulence the spectral distribution of the cross-phase has to be considered together with the coherence spectrum. For incoherent signals the cross-phase randomly jumps between $\pm\pi$. It is only of relevance on spectral scales of high coherence. Additionally one has to take into account that this is not a local measurement. A finite phase shift is always introduced by the poloidal separation of probes. This phase shift is given by the dispersion relation of the observed wave and depends on the frequency ν , the probe separation Δy and the phase velocity v :

$$\alpha'(\nu) = \frac{\Delta y}{v} \nu. \quad (5.1)$$

α' is negligible for probe separations far below the poloidal correlation length, $\Delta y \ll d_\theta$. To what extent the phase spectrum was tampered by the finite probe separation can be checked by looking at results for different Δy . For WEGA this was done by using the triple probe combination used for transport measurements (fig. 5.1.6). The two potential probes reflect a distance of ± 5 mm in poloidal direction compared to the I_{sat} probe. The result is shown in fig. 5.1.4. Data was taken from a He discharge at low magnetic field. The artificial phase shift α' was negligible in this case. Neither in the coherence nor in the phase spectrum a difference between the two opposed probe separations was found. A clear shape of $\alpha(\nu)$ was observed in the low frequency range up to $\nu \approx 50$ kHz. For higher frequencies, where the coherence was weak, the expected random phase appeared. The important finding that can be taken from this analysis is that at low frequencies the phase shift between density and potential fluctuations was close to zero. This is a strong indicator that we are dealing with drift wave turbulence following the list of characteristic features given in section 2.3.2. The cross-power weighted averaged cross-phase defined in eqn. (3.18) was $\bar{\alpha} \approx 0.1\pi$ for the plotted data. The radial profile of $\bar{\alpha}$ is shown in fig. 5.1.5. In this representation the dominance of drift waves both in the core plasma as well as in the SOL can be seen. $\bar{\alpha}$ was below 0.25π both inside and outside the LCFS. The fact that $\bar{\alpha}$ was finite at all is due to the non adiabatic electron response introduced by some dissipative effect. As shown in section 2.3.2 a finite phase shift is a prerequisite for the destabilisation of drift waves and hence for the development

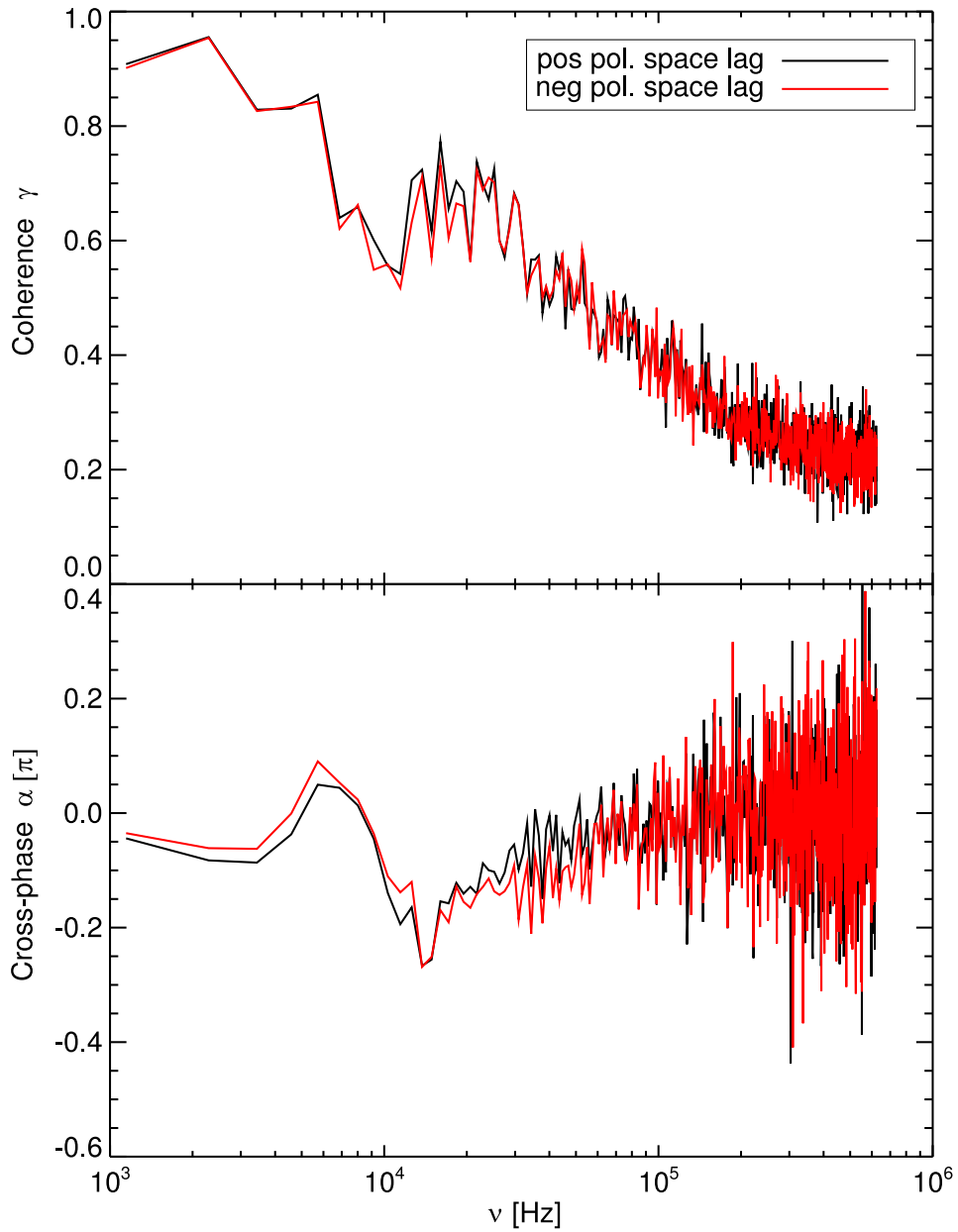


Figure 5.1.4: Coherence and cross-phase spectrum between \tilde{I}_{sat} and $\tilde{\Phi}_{\text{fl}}$. Data was taken by three neighbouring probes of the array. The outer probes measured $\tilde{\Phi}_{\text{fl}}$, the central one \tilde{I}_{sat} . The red and black lines were calculated from the cross spectrum of the \tilde{I}_{sat} -probe with one of the $\tilde{\Phi}_{\text{fl}}$ -probes each. The poloidal separation between the probes has no significant influence on the phase spectrum, since both lines coincide satisfactorily. Data was taken in a He discharge at low field about 1 cm inside the LCFS.

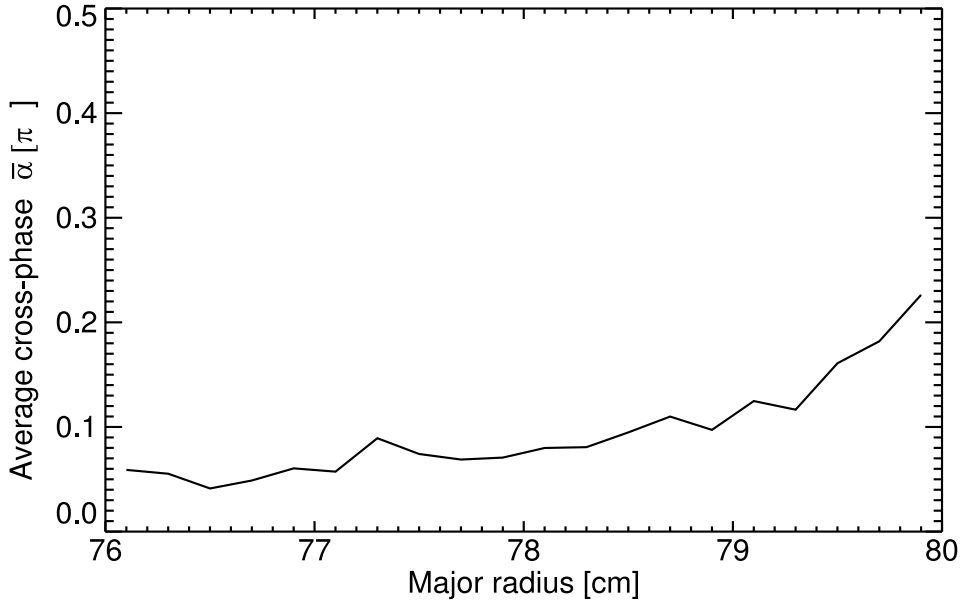


Figure 5.1.5: Radial profile of the averaged cross-phase $\bar{\alpha}$ between potential and density fluctuations for a He discharge at low field. $\bar{\alpha}$ is close to 0 over the whole cross section.

of turbulence. In the observed case of weakly ionised edge plasmas at low field in WEGA electron collisions with ions and neutrals, hence resistivity, is responsible for the nonadiabatic electron response. With respect to this it is obvious that $\bar{\alpha}$ was continuously increasing going towards the plasma edge because the resistivity due to neutral collisions in a weakly ionised plasma is $\eta \propto \frac{n_n T_e}{n_e}$ and thus increasing with increasing radius.

5.1.4 A Qualitative Treatment of Turbulent Transport

The probe array can be used to measure radial particle flux caused by turbulence. To this end probes are connected to measure \tilde{I}_{sat} and $\tilde{\Phi}_{\text{fl}}$ in alternation. Three neighbouring probes can then be used to determine the local flux. The principle of such a triple probe is indicated in fig. 5.1.6. It is capable of measuring radial flux caused by $\mathbf{E} \times \mathbf{B}$ convection according to eqn. (2.18). The poloidal electric field in this setup is calculated from the difference in $\tilde{\Phi}_{\text{fl}}$ between the two outer probes with a poloidal distance of $\Delta y = 1$ cm, $\tilde{E}_{\theta} = \frac{\tilde{\Phi}_{\text{fl},1} - \tilde{\Phi}_{\text{fl},2}}{\Delta y}$. \tilde{E}_{θ} is the poloidal electric field, where poloidal means perpendicular to \mathbf{B} on a flux surface, Since probes are aligned on a flux surface \tilde{E}_{θ} is the poloidal electric field on a flux surface causing radial $\mathbf{E} \times \mathbf{B}$ drift perpendicular to a flux surface. Due to the finite probe separation E_{θ} is not a local value but an average over the probe separation. One has to keep this in mind when dealing with turbulence, where the total amount of transport is distributed over a broad spectrum of spatial scales. Transport on scales smaller

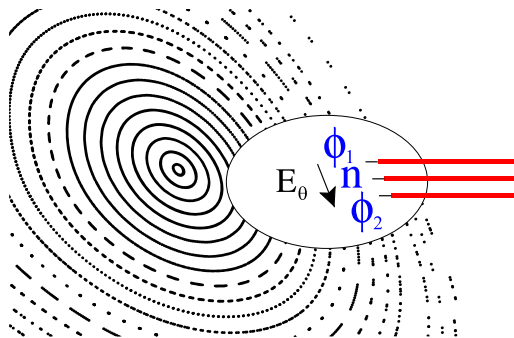


Figure 5.1.6: Arrangement of probes to measure radial $\mathbf{E} \times \mathbf{B}$ flux. The poloidal electric field E_θ is deduced from the potential difference between the outer probes. Due to the finite probe separation the calculated particle flux generally represents an average over ≈ 1 cm in poloidal direction.

than Δy cannot be resolved by the array.

Radial profiles of the net radial transport can be seen in fig. 5.1.7. The figure shows a comparison between He discharges at high (a) and low (b) field with $t \approx 0.2$. Two major differences between the two operation modes can be seen. Γ was not analysed quantitatively, but it is plotted in equal units in both cases. For low field Γ was about one order of magnitude higher than for high field. Since the fluctuation amplitudes of both \tilde{I}_{sat} and \tilde{E}_θ were found to be of the same order for both cases, the scaling is mostly related to the $1/B$ dependence of the $\mathbf{E} \times \mathbf{B}$ velocity. The turbulent particle flux is determined by

$$\langle \Gamma \rangle = \langle \tilde{n} \tilde{v}_r \rangle \propto \frac{\tilde{I}_{\text{sat}} \tilde{E}_\theta}{B}.$$

The second striking difference between transport in low and high field case was a fundamental difference in the shape of the flux profile. For low field Γ continually increased going radially outwards showing a maximum outside the LCFS at $R \approx 79$ cm. This is consistent with experimental diffusion coefficients obtained from a global particle balance [Hor05]. Here, also an increase with radius has been found for low field. For high field just the opposite behaviour is observed. Γ continuously increases going radially inwards.

Transport profiles from both, low and high field coincided qualitatively with the results on the fluctuation amplitude presented above. As shown in section 2.2.2 turbulent transport is determined by the fluctuation amplitude as well as the cross-phase between density and potential fluctuations. Maximum transport at low field occurred at the edges where fluctuations were at their strongest, although the peak in the profile was further outside than the peak in the fluctuation amplitude (5.1.3). This is due to the increasing cross-phase outside the LCFS. For high field the transport as well as the fluctuation amplitude (see fig. 5.1.8 (a)) continuously increased going towards the plasma centre.

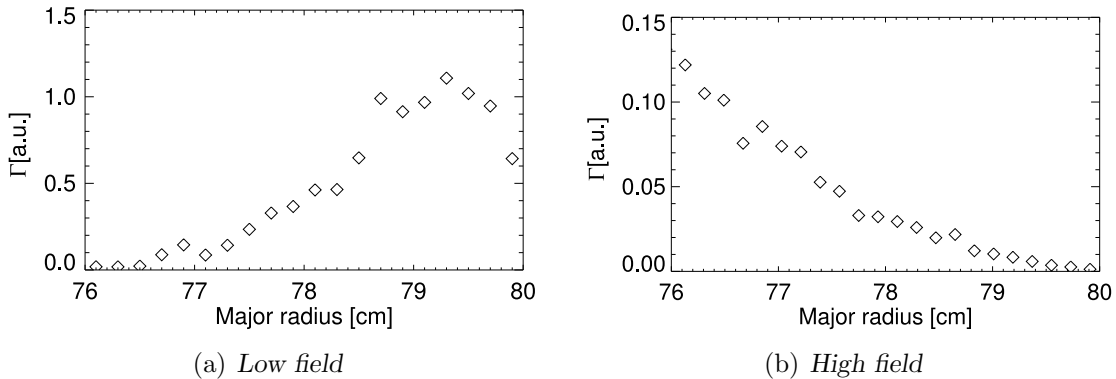


Figure 5.1.7: Radial profiles of particle flux caused by turbulent $\mathbf{E} \times \mathbf{B}$ convection. There is a fundamental difference between the profile shape for low (a) and high (b) field operation. The magnitude of Γ is plotted in arbitrary, but equal units for both cases.

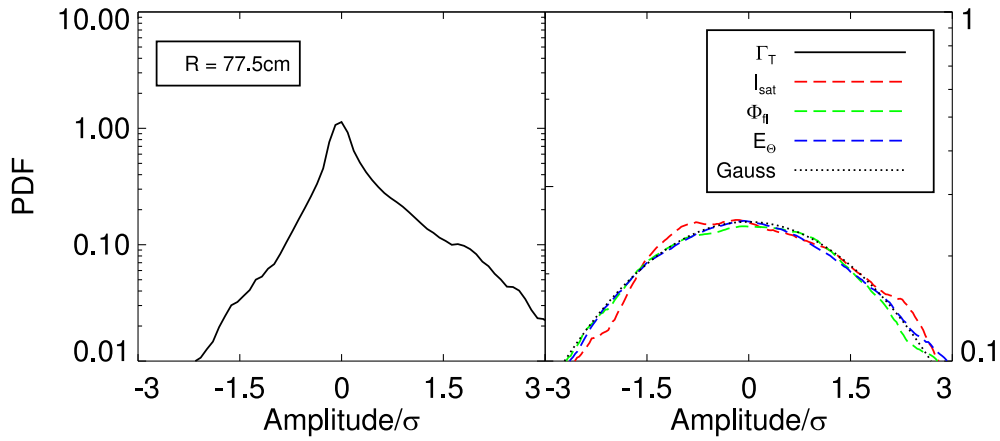
5.1.5 Statistical Properties of Fluctuations

A universal observation in magnetised plasmas is that the PDF of fluctuation induced transport shows a significant deviation from a Gaussian distribution [Hid95]. A significant fraction of the total flux can be attributed to large sporadic bursts revealing an intermittent character of the transport. The universality of this intermittent nature of turbulent transport is widely accepted because it is observed in different types of experiments as stellarators [Car+96; Ble98], tokamaks [End94; Fil+95; Car+96; Boe+03; Ant04] and linear devices without confinement [Hul+91; WGK06]. Less universality is found in the statistical properties of density and potential fluctuations which lead to turbulent transport. Non Gaussian PDF of transport may be caused by non Gaussian density and potential fluctuations [Jha+92]. However, more commonly observed is that \tilde{n}_e and $\tilde{\Phi}_f$ have a PDF close to a Gaussian inside the LCFS and more intermittent in the SOL [Car+96; San+00].

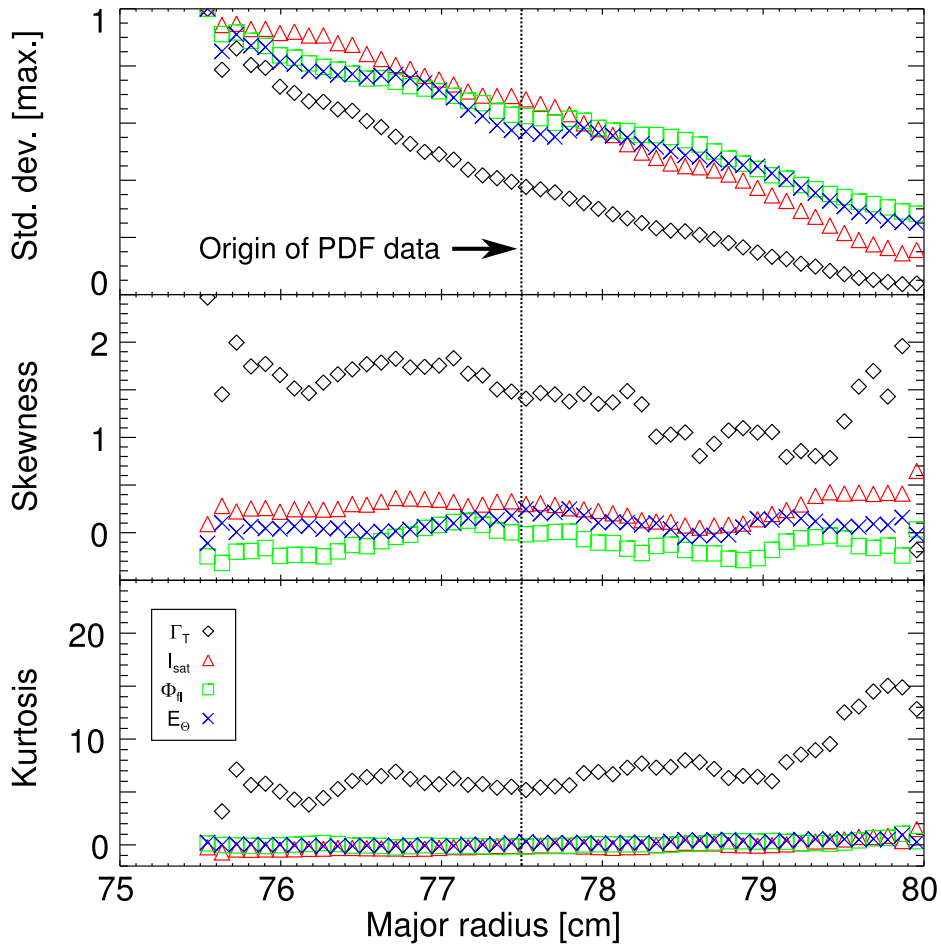
The PDF of time series of data taken with the array connected as transport probes have been analysed. The results for high and low field are shown on the left and on the right hand side of fig. 5.1.8, respectively. Data was taken from a subwindow in the core plasma ≈ 1 cm inside the LCFS. All graphs are normalised to an integral value of 1. A Gaussian distribution with unit standard deviation is plotted for comparison. \tilde{I}_{sat} , $\tilde{\Phi}_f$ as well as \tilde{E}_θ show a PDF looking quite similar to a Gaussian distribution for amplitudes between $\pm 3\sigma$, especially in the high field case. In contrast the radial particle flux has a much steeper maximum and an asymmetry leading to a net mean value. The difference in the statistical properties can be further quantified by looking at the statistical moments of data. Fig. 5.1.8 (b) shows radial profiles of standard deviation, skewness and kurtosis of plasma parameters as well as transport. Skewness and kurtosis of fluctuating plasma parameters at the observed position are close to zero as for a Gaussian PDF, which can be described only by the first moment, the standard deviation. The flux shows a positive skewness of

$S \approx 1.4$ which stands for a net radial transport directed outwards. The intermittent character of transport becomes manifest in a positive kurtosis of $K \approx 5$ yielding a steeper maximum and broader wings than that of a Gaussian distribution. The transport is carried by a minor fraction of large transport events. This general nature of turbulence is conserved over the whole observed plasma cross section. No deviation from a Gaussian distribution of plasma parameters was observed, either in the core or in the SOL. The shape of the flux PDF also did not change significantly in the observed region. The changes in the profiles of net radial transport shown in sec. 5.1.4 are carried only by a higher fluctuation amplitude as can be seen from the profiles of the standard deviation.

The results from low field operation look different (5.1.8 (c), (d)). Density fluctuations still show a skewness and kurtosis close to zero. However, potential fluctuations show a negative skewness in the region of high corresponding fluctuation amplitude. This is not the case for electric field fluctuations, which show a negligible skewness. The skewness of the flux is positive in the edge plasma, where a significant amount of transport is observed. The erratic behaviour for $R < 77$ cm is not relevant because the net transport nearly vanishes in this region. Kurtosis of potential and electric field fluctuations has positive values of $K \approx 2 \dots 5$ along the density gradient region from $R \approx 77 \dots 80$ cm. $\tilde{\Gamma}$ has an even higher kurtosis than for high field: $K > 10$.

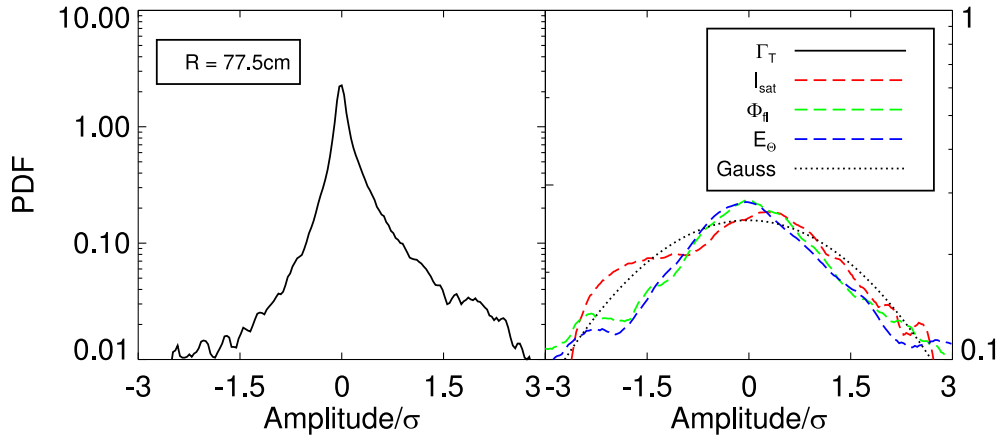


(a) PDF (high field)

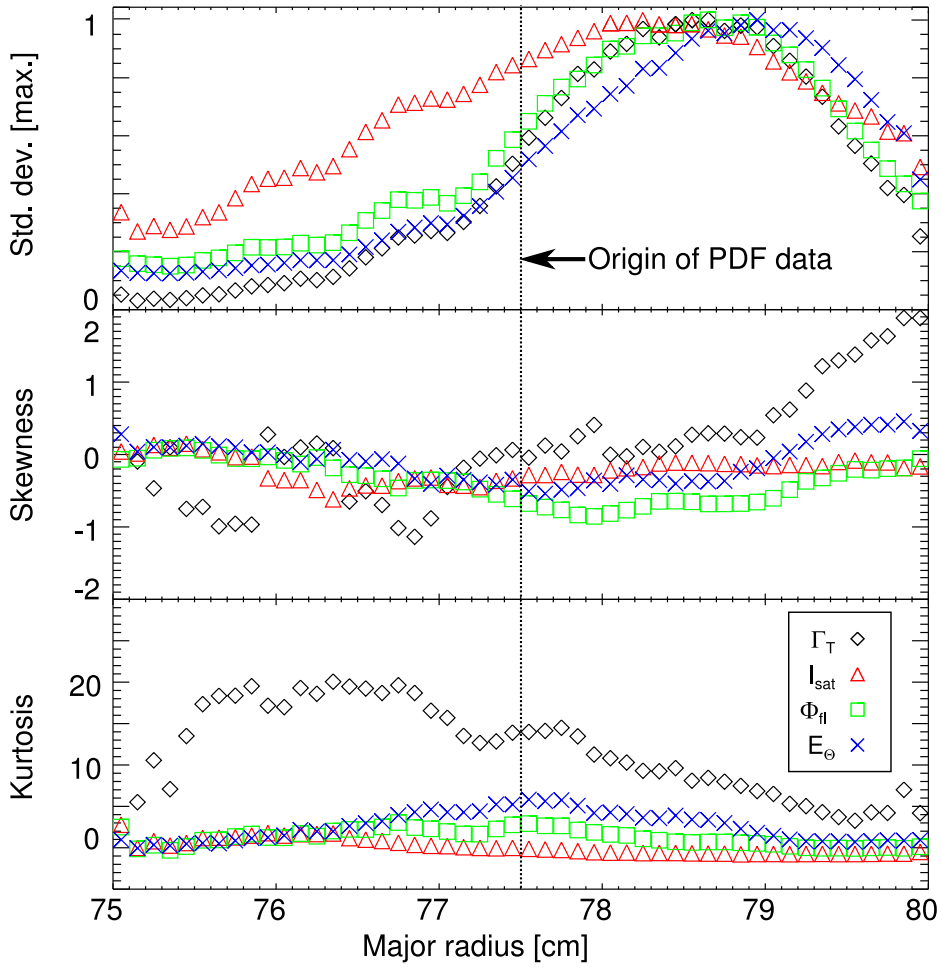


(b) Statistical moments (high field)

Figure 5.1.8: Statistical properties of fluctuations at high field (a, b) and low field (c, d). a, c) PDF of flux, density, potential and electric field fluctuations obtained from data measured at $R = 77.5 \text{ cm}$. The signal amplitude is given in units of the standard deviation, the curves are normalised to an integral value of 1.



(c) PDF (low field)



(d) Statistical moments (low field)

On the r.h.s. a Gaussian PDF with the same normalisation is plotted for comparison (dotted). b, d) Radial profiles of standard deviation, skewness and kurtosis of the fluctuating quantities. The standard deviation is in all cases normalised to a maximum of 1 in the profile.

5.2 Perpendicular Dynamics of Turbulence

The results presented so far do not give any information about the spatial structure of turbulence. The initial step in spatially and temporally resolved experiments is the use of the probe array described in section 4.4.1. The resolution in space is limited to one dimension, namely the poloidal direction. This may lead to artefacts in the results of correlation analysis which is applied to the raw data as explained in section 3.2. But a comparison with the three-dimensional view presented in section 5.3 will show that the results are plausible. The following section gives insight into the dynamics of fluctuations perpendicular to the magnetic field on a flux surface.

5.2.1 Turbulent Structures in Raw Data

Plasma turbulence is generally associated with the picture of sporadically occurring events with a certain spatial extent and lifetime. This goes together with the general picture of turbulent flows as large scale vortices losing their shape by breaking up into finer and finer structures. Some information about the spatio-temporal structure and the poloidal dynamics of fluctuation events can already be gained from the visualisation of raw data. Fig. 5.2.1 shows a contour plot of poloidally and temporally resolved raw data of \tilde{I}_{sat} from a He discharge at high field. Data from individual probe tips were normalised to their standard deviation in order to equilibrate effects coming from different sensitivity due to small differences in the probe geometry. Data was taken from a position inside the LCFS. Fluctuations in form of sporadically appearing events of high fluctuation amplitude could already be seen in the raw data. These events appeared randomly at any position in the inspected poloidal window, propagated along the array and disappear after a certain lifetime. Fluctuations moved along the observed window predominantly in the poloidal direction from the upper to the lower end with an apparently well defined velocity. The poloidal velocity of the majority of structures in this case pointed in electron diamagnetic drift direction. Amplitude, size and lifetime of structures scattered as expected for turbulence. This necessitates statistical methods to extract averaged event informations.

5.2.2 Poloidal-Temporal Correlation Function

The spatio-temporal cross correlation function (CCF) introduced in section 3.2 was used to extract averaged information about turbulent structures. It can be used to extract averaged fluctuation parameters like lifetime, structure size and velocity from turbulent rawdata. The method to extract fluctuation parameters from the CCF has been introduced in [End94]. The spatio-temporal correlation function postulates fluctuations which are distributed homogeneously both in space and time. This requirement was met in the window under observation as can be seen in the raw data. Fig. 5.2.2 shows the normalised CCF calculated from raw data in fig. 5.2.1. The relative correlation amplitude is plotted against the time lag τ on the abscissa and the space lag d on the ordinate. d corresponds to the poloidal probe distance.

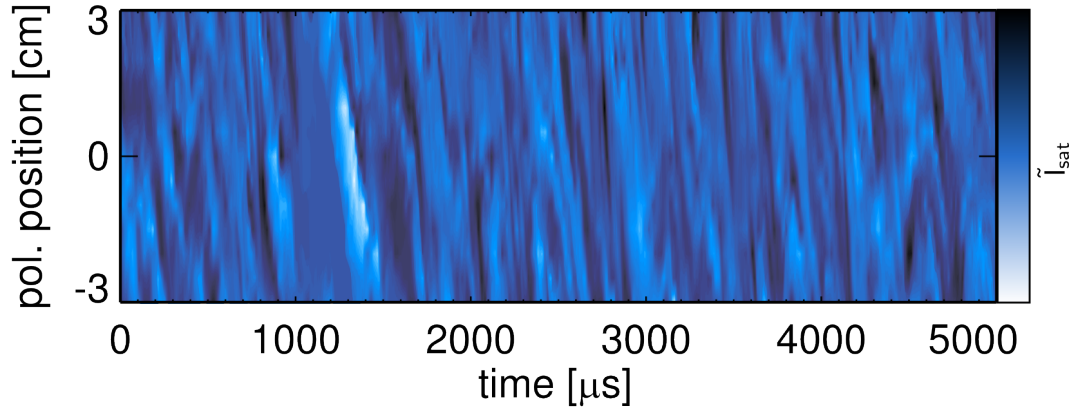


Figure 5.2.1: Poloidally and temporally resolved rawdata of \tilde{I}_{sat} from a He discharge at high field. The data was taken from a subwindow measured about 1 cm inside the LCFS. The given poloidal position corresponds to the distance from the equatorial plan ($z=0$). The amplitude of \tilde{I}_{sat} is colour-coded.

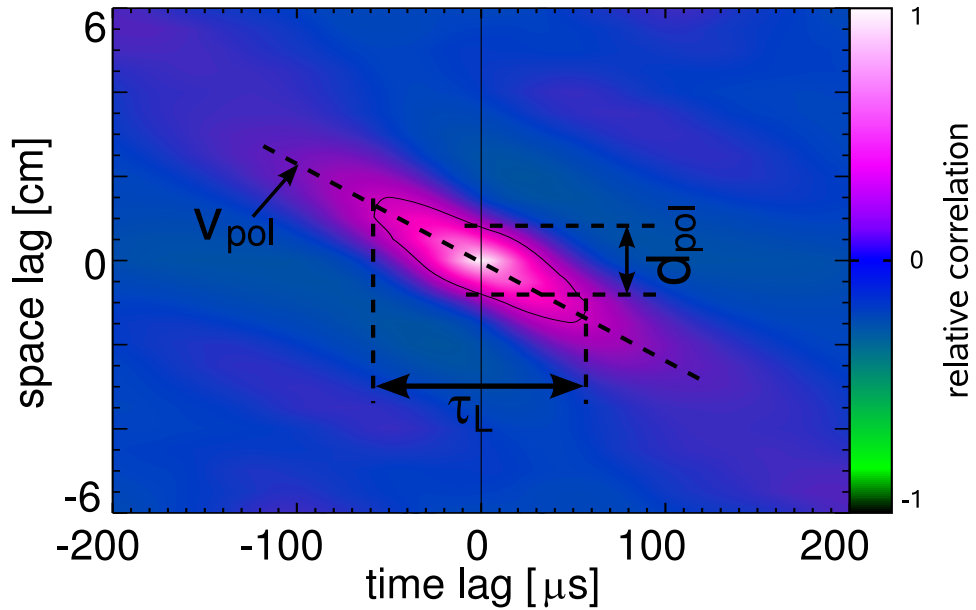


Figure 5.2.2: Poloidal-temporal correlation function of \tilde{I}_{sat} from a He discharge at $B=500$ mT (rawdata from fig. 5.2.1). The space lag corresponds to the poloidal probe separation. Colour coded is the relative correlation (normalised to 1). The fluctuation parameters can be extracted from the inclination and the width of the structure at a certain correlation level ($1/e$ in this case).

To explain step by step what information can be deduced from such a picture we start at zero time lag ($\tau = 0$). Here, a continuous loss of correlation can be seen with increasing space lag. The width of the CCF at $\tau = 0$ is called poloidal correlation length d_θ and reflects the average poloidal size of turbulent structures [Ram+05]. d_θ is the width of $\psi(d, \tau = 0)$ at a given amplitude. The definition of the amplitude at which d_θ is taken is arbitrary. In this work the full width at the points where the correlation has dropped to a value of $1/e \approx 0.37$ is used as definition for d_θ . The correlation length in fig. 5.2.2 is: $d_\theta = (2 \pm 0.5)$ cm. The error is given by the probe separation of 5 mm, i.e. the spatial resolution of the diagnostic. The spatial shape of the CCF is approximately conserved for non zero time lags, but the maximum is found at finite space lags. This means that the whole structure is propagating in poloidal direction. The direction of motion is the electron diamagnetic drift direction as could already be seen in the raw data. The correlation maxima for different time lags can be well fitted by a straight line. The inclination of this line reflects the averaged poloidal velocity of structures, $v_\theta = \frac{\partial d_{max}(\tau)}{\partial \tau}$. In the given example the poloidal velocity is $|v_\theta| \approx 200$ m/s. The collapsing of structures after a finite lifetime, which has already been seen in the raw data, appears in the CCF as a loss of correlation for increasing time lag. The correlation time of structures is defined as the temporal $1/e$ -width of the CCF, corresponding to the definition of d_θ . But, to relate the correlation time to a lifetime τ_L of structures it has to be evaluated in the co-moving frame of the structure as indicated in fig. 5.2.2. The $1/e$ width of $\psi(d = 0, \tau)$ is called auto-correlation time and reflects only the time a structure needs to pass a single probe. But, even in the co-moving frame the extracted lifetime has to be treated under the restrictions detailed in section 3.2, that no radial motion of structures is visible in this limited pure poloidal perspective. From the data presented in fig. 5.2.2 a lifetime of $\tau_L \approx 100 \mu\text{s}$ can be evaluated. A parameter study of fluctuation parameters will be presented later in this section.

5.2.3 $k_\theta\nu$ -Spectrum

According to the Wiener-Khintchine theorem CCF and power spectrum represent the same information. This was applied to the poloidal temporal CCF in order to show the spectral distribution of power in terms of the poloidal wavenumber k_θ and the frequency ν . The outcome of this analysis is a $k_\theta\nu$ -spectrum as shown in fig. 5.2.3 derived from the dataset of density fluctuations presented previously. The spectral power is colour coded logarithmically in this contour plot. The turbulent nature is represented by a broad distribution of power in Fourier space. Most power was located in the low frequency range below 10 kHz and for small wavenumbers below 2 cm^{-1} . It should be noted that the resolution in wavenumber space was rather poor in this range with a separation of points of $\Delta k_\theta \approx 0.5 \text{ cm}^{-1}$ as a consequence of the array geometry. Looking at the data fig. 5.2.3 as a dispersion relation, a good agreement with predictions from drift wave theory can be seen. The dashed line represents the dispersion relation of a drift wave calculated following eqn. (2.25). Based on measurements of equilibrium plasma parameters, $T_e = 5 \text{ eV}$, $L_\perp = 2.5 \text{ cm}$

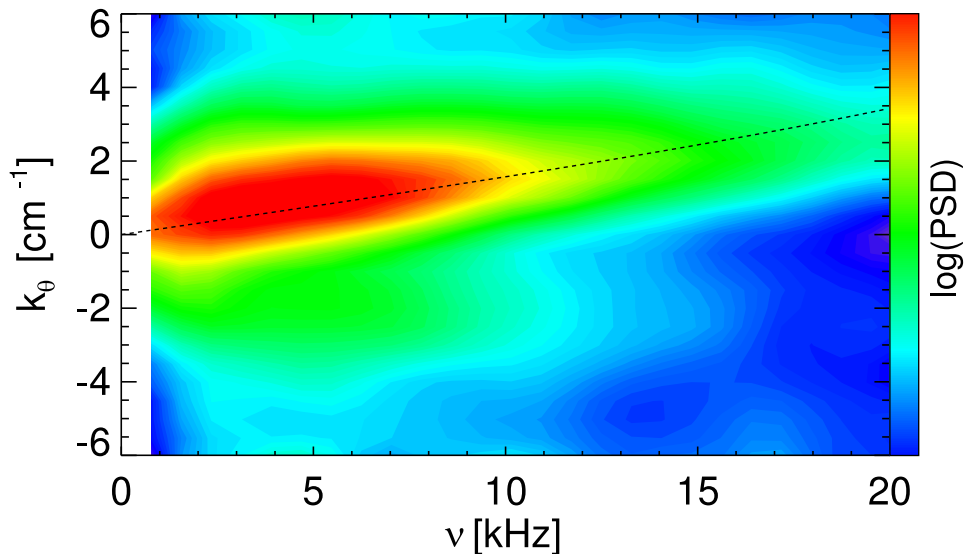


Figure 5.2.3: $k\nu$ power spectrum of density fluctuations calculated from the raw data shown in fig. 5.2.1. The signal power is scaled logarithmically. The dashed line corresponds to the linear dispersion relation of a drift wave calculated from measured stationary plasma and discharge parameters. Most power in the turbulent broad band spectrum is distributed around the linear dispersion relation.

and $\rho_s = 1$ mm have been used for the calculation of $\nu(k_\theta)$. This result suggests the description of turbulent fluctuation events as a superposition of modes with a common poloidal phase velocity given by $2\pi\nu/k_\theta$. The importance of this finding will become clear in section 5.3, where a three-dimensional picture is constructed based on two point measurements in toroidal direction. The observed collapse of structures after a finite lifetime cannot be explained by dispersion but by dissipation occurring on small scales.

5.2.4 Wavenumber Spectrum

The overall distribution of power over spatial scales becomes clear in wavenumber spectra. These were calculated from the $k_\theta\nu$ -spectrum by summing up all points in frequency space for each wavenumber. Fig. 5.2.4 shows the k_θ -spectrum for the dataset discussed above. The shape of the spectrum has the expected broad band character of fully developed turbulence. For small wavenumbers the spectrum is flat, but this region may not be rated to high. The low k_θ end of the spectrum results from the outermost probes of the array. To avoid spectral leakage this region was weakly weighted in the Fourier transform as explained in section 3.3.4. However, the inertial range of the spectrum ($1.5 \text{ cm}^{-1} \lesssim k_\theta \lesssim 4 \text{ cm}^{-1}$) was well resolved by the array. The turbulent energy cascade manifests itself as a linear decay of fluctuation power in the double logarithmic plot. Mathematically this region was described by a power law, $S(k) \propto k^m$, where m is called spectral index. In the given example a

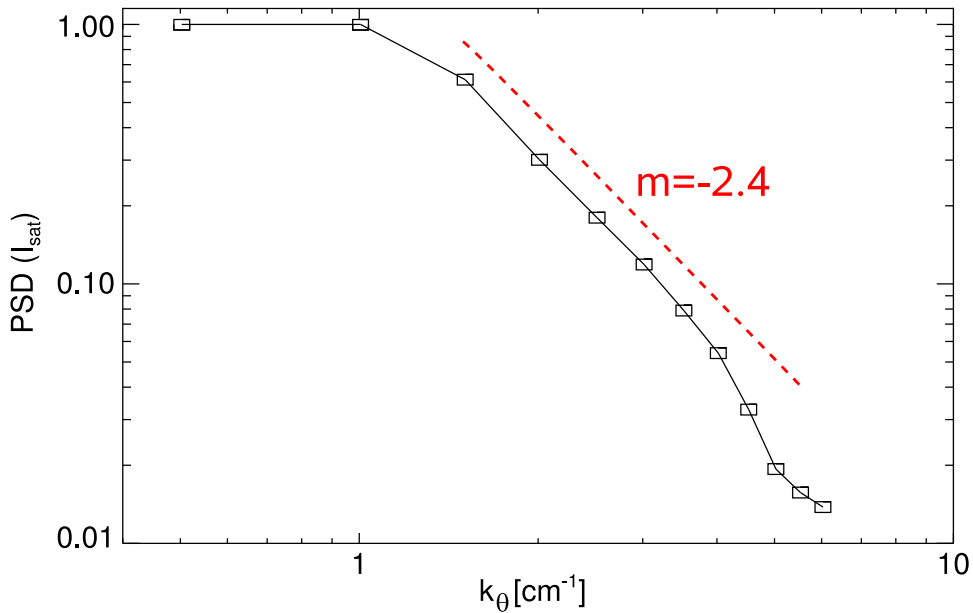


Figure 5.2.4: Wavenumber spectrum calculated by integrating in frequency space for each wavenumber component in fig. 5.2.3. The inertial range between $1.5 \text{ cm}^{-1} \lesssim k_\theta \lesssim 4 \text{ cm}^{-1}$ follows a power law with a spectral index of $m \approx -2.4$.

spectral index of $m \approx -2.4$ was found, as indicated by the dashed line in fig. 5.2.4.

5.2.5 Poloidal Velocity Profiles

The velocity deduced from the CCF as described in section 5.2.2 is measured in the stationary laboratory frame. v_θ is thus not necessarily equal to the phase velocity of the observed structure. Stationary radial electric fields E_r lead to a poloidal rotation of the whole plasma column within a flux surface. The resulting $\mathbf{E} \times \mathbf{B}$ velocity is equal for all species in the plasma since it does neither depend on the charge nor on the mass. The detected poloidal velocity is the sum of phase velocity and $\mathbf{E} \times \mathbf{B}$ velocity:

$$v_\theta = v_{ph} + \frac{\mathbf{E}_r}{B} \quad (5.2)$$

The phase velocity of drift waves is the electron diamagnetic drift velocity $v_{dia,e}$. The contribution of the $\mathbf{E} \times \mathbf{B}$ drift to the observed radial velocity profiles of v_θ was deduced from equilibrium profiles of plasma parameters. A comparison of v_θ with steady-state plasma flow components ($v_{\mathbf{E} \times \mathbf{B}}$ and $v_{dia,e}$) is shown in fig. 5.2.5. Data was again taken from the dataset which has been treated in the previous sections. The black crosses are v_θ correspond to the poloidal velocity of turbulent structures deduced from the CCF. The plot shows a typical feature which was observed for high field discharges in WEGA. v_θ changed sign close to the LCFS. It pointed in electron diamagnetic drift direction inside the LCFS and in ion diamagnetic drift direction in

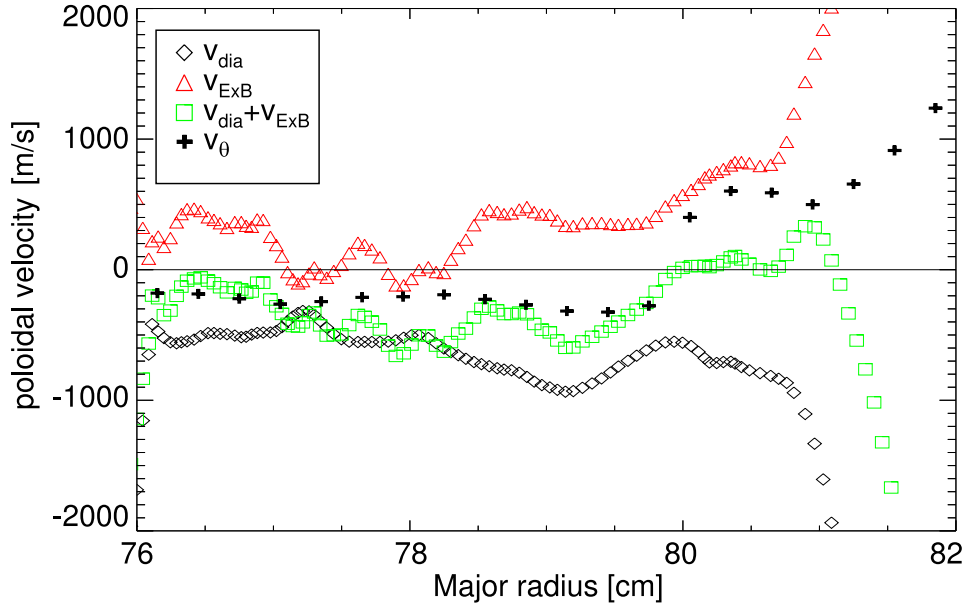


Figure 5.2.5: Profiles of poloidal velocity components for a He discharge at high field. $v_{dia,e}$ and $v_{\mathbf{E} \times \mathbf{B}}$ deduced from swept Langmuir probe measurements are compared to the poloidal velocity of turbulent structures. The change of sign in $v_{structure}$ is qualitatively reproduced by the stationary plasma flow.

the SOL. Inside the LCFS radial electric fields for the high field case were found to be quite small and v_θ was governed by $v_{dia,e}$. The contribution from the steady-state $\mathbf{E} \times \mathbf{B}$ plasma flow to the structure velocity was negligible. This can be seen in fig. 5.2.5. Outside the LCFS the $\mathbf{E} \times \mathbf{B}$ affects the turbulence dynamics leading to a reversal of v_θ . The point where v_θ changes sign will be referred to as reversal point subsequently. It was caused by a sheared profile of the poloidal $\mathbf{E} \times \mathbf{B}$ velocity. The region around the reversal point, where v_θ undergoes a rapid radial change, is called the velocity shear layer. The formation of a velocity shear layer is an intrinsic feature at the transition from closed flux surfaces to open field lines intersecting material surfaces [Tsu92]. The sum of both contributing components agreed satisfactorily with the measured v_θ . The strong contribution of the diamagnetic term to v_θ confirms again the expectation of drift wave turbulence being dominant in WEGA.

5.2.6 Differences in High and Low Field Operation

In section 5.1.4 it was shown that the difference between the two operation regimes of WEGA, i.e. low and high field case, has more of the character of essentially different regimes than simply reflects a scaling of parameters from low to high field. The following section elucidates these differences in more detail.

The most striking difference in perpendicular dynamics between the two cases was the general absence of a velocity shear layer in the low field case. Fluctuations

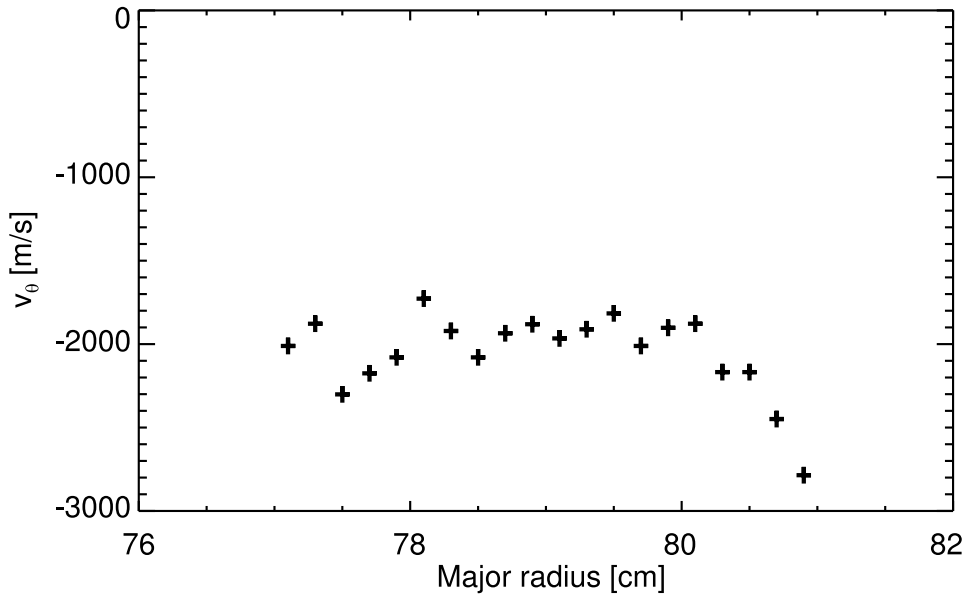


Figure 5.2.6: Radial profile of v_θ of turbulent structures for a He discharge at low field. The velocity components deduced from equilibrium profiles is not given for comparison, because the scatter in the data is too large.

propagated in electron diamagnetic drift direction at all radial positions in this case. An example for a He discharge at $\mathbf{B} = 57$ mT and $t_0 = 0.182$ is shown in fig. 5.2.6, where the typical flat profile of v_θ in the low field case can be seen. Inside the LCFS the propagation velocity of structures was in electron diamagnetic direction in both cases, but v_θ was typically higher by almost one order of magnitude at low than at high field. This difference is obvious because in both cases v_θ was governed by $v_{dia,e}$. As the perpendicular density gradient length did not change significantly for the two cases, the observed change in v_θ was related to: $v_{dia,e} \propto B^{-1}$.

The change in dynamics is depicted in fig. 5.2.7 where the poloidal-temporal correlation function is shown in a contour plot for high and low field. The lifetime of structures remained unchanged at $\tau_L \approx 100 \mu\text{s}$. This value seems to be rather universal for WEGA. It was at a comparable level in all observed discharges. No systematic variation with discharge parameters could be found. Changes in lifetime revealed more a statistical scatter than a systematic variation. Unlike the lifetime of structures, a strong variability of the poloidal correlation length d_θ and therefore the structure size was observed. At high field the correlation length was $d_\theta = 2$ cm as mentioned above. At low field d_θ exceeded the poloidal width of the correlation window of 12 cm. A tentative explanation for the strong magnetic field dependence of d_θ could be found in the dispersion scale ρ_s , which is a typical scaling length for drift waves. Since this scaling would be another indicator for drift waves, the effect was highlighted in a broader parameter scan than the two field cases compared up to now.

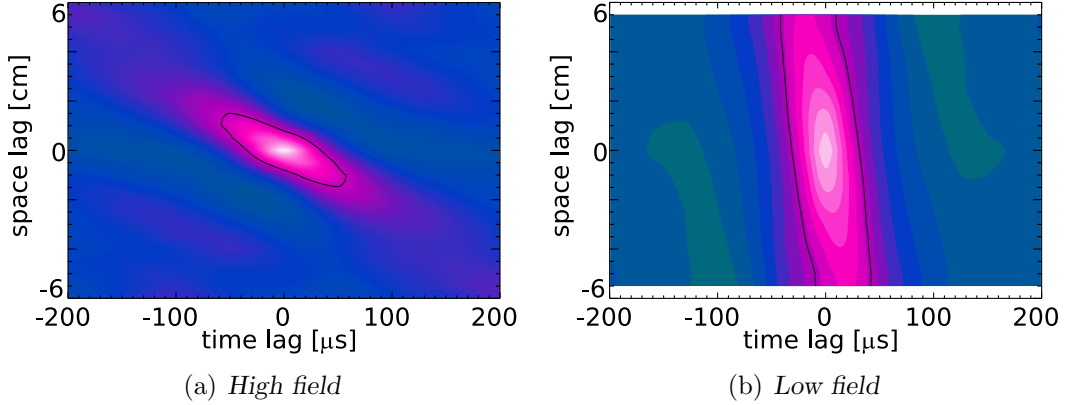


Figure 5.2.7: Poloidal-temporal correlation function of \tilde{I}_{sat} compared for the low (a) and the high (b) field case. Data was both taken about 1 cm inside the LCFS in a He discharge at $t_0 = 0.182$.

5.2.7 Scaling of Structure Size

Changing the magnetic field is one way to investigate the influence of ρ_s on d_θ . The strong dependence of d_θ on B is apparent from fig. 5.2.7. Fig. 5.2.8 depicts the effect more clearly in a cut through the CCF at $\tau = 0$. To come around with the problem of d_θ being greater than the window width a two-dimensional fit function introduced by Endler [End94] was applied to the data. A simplified version of the original fit function was used:

$$\psi_{fit}(d, \tau) = A \left(\cosh \left(\frac{\tau}{\tau_1} \right) \right)^{-1} \left(\cosh \left(\frac{d - v_\theta \tau}{l_1} \right) \right)^{-1} + c \quad (5.3)$$

The fit parameters τ_1 and l_1 are a characteristic width in temporal and spatial direction, respectively. v_θ is the poloidal velocity. A is the amplitude and c is a constant offset. A and c are necessary because only a part of the complete correlation function is fitted. A low frequency periodic part, which is typically present, will therefore appear as an offset. A fit of eqn. (5.3) to the CCF of the low field case (fig. 5.2.7 b) resulted in a correlation length of $d_\theta = 14$ cm. The variation of d_θ is nearly linear with B^{-1} and thus also linear with ρ_s since T_e in the plasma edge did not differ significantly between the two cases, $\frac{d_{\theta,low}}{d_{\theta,high}} = \frac{14 \text{ cm}}{2 \text{ cm}} = 7 \approx \frac{500 \text{ mT}}{57 \text{ mT}}$. In order to clarify if this variation can be related to the dispersion scale, ρ_s was varied at a constant magnetic field. T_e cannot be actively controlled in WEGA, and can therefore be excluded as control parameter for a ρ_s scan. The relevant control parameter was the ion mass which could be varied by using different discharge gases. Using H_2 , He, Ne and Ar as discharge gas, respectively, ρ_s could be varied in a range of $\rho_s \approx 0.5 \dots 3$ mm at a constant magnetic field strength. The given values correspond to the high field case where structures can be fully resolved without exceeding the length of the array. The behaviour of d_θ during this scan is shown in fig. 5.2.8 b). The shape of the correlation function at zero time lag remained nearly unchanged

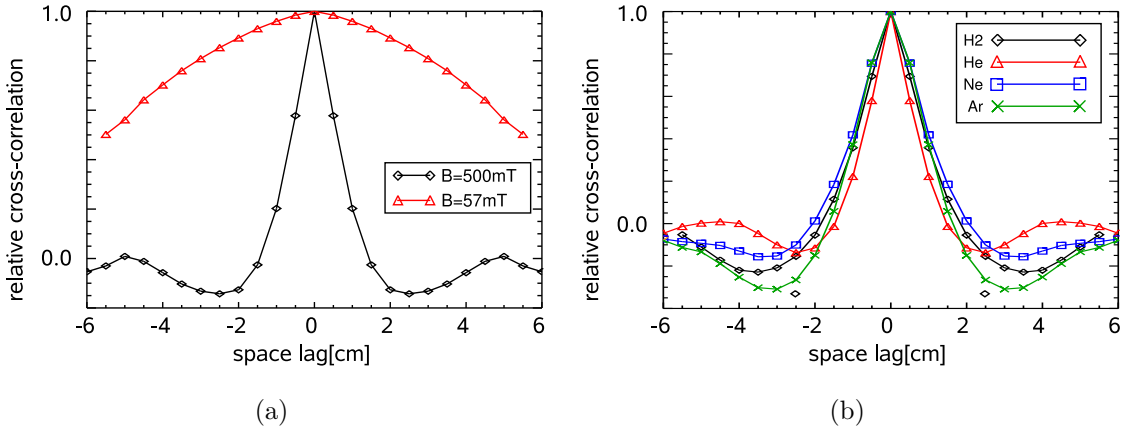


Figure 5.2.8: Snapshots of the poloidal-temporal correlation function of \tilde{I}_{sat} at $\tau = 0$. a) Comparison of low and high field case at equal ion mass (He). b) Variation of m_i by using different discharge gases at constant $B = 500\text{ mT}$ (high field).

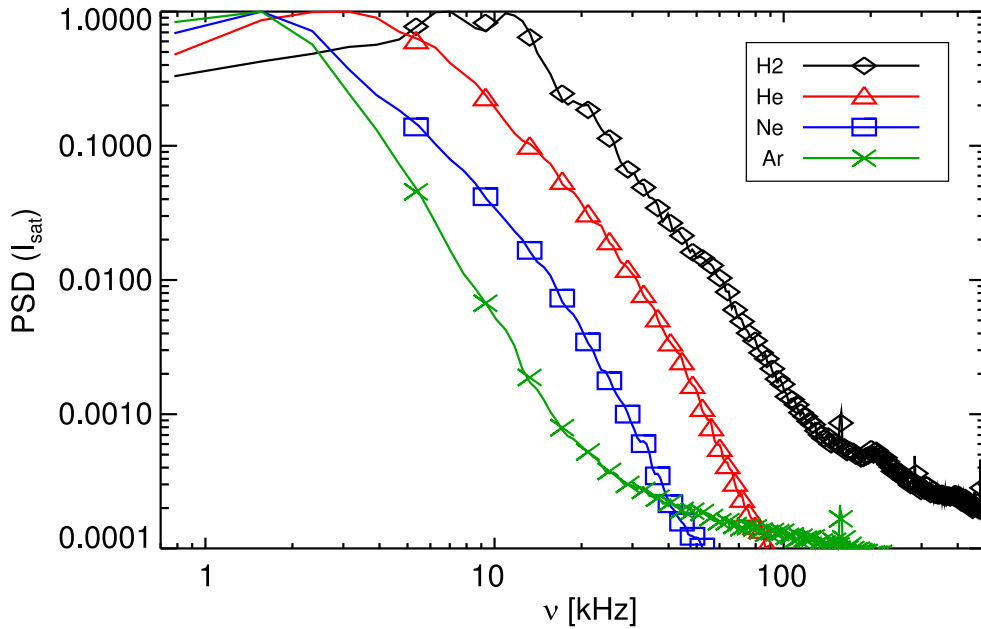


Figure 5.2.9: Scaling of frequency spectra of \tilde{I}_{sat} during the m_i scan at high field shown in fig. 5.2.8 (b). All spectra are normalised to a maximum power of 1.

and d_θ was also preserved. The same behaviour was observed for low field, although here only H_2 and He have been used. The preserved correlation at $\tau = 0$ does not imply, however, that the turbulence dynamics did not change at all. As mentioned above the lifetime was found to be more or less constant. What changed systematically in the ion mass scan was the poloidal velocity. v_θ continuously decreased with increasing ion mass, following approximately the relation: $v_\theta \propto m_i^{-1/2}$. This could be explained by an experimentally observed reduction of the density gradient length which goes together with a reduction of $v_{dia,e}$. The contribution of the $\mathbf{E} \times \mathbf{B}$ drift was negligible inside the LCFS where data has been analysed, as shown in section 5.2.5. The variation of v_θ could not be fully reproduced by steady-state flow measurements, but at least a general trend to smaller diamagnetic drift velocities with increasing ion mass was observed. The two observations, i.e. the preserved spatial scales together with a strong change in v_θ , can be treated in terms of the linear dispersion relation found in the $k_\theta \nu$ -spectra (see section 5.2.3). The preserved shape of the poloidal CCF is equivalent to coinciding wavenumber spectra during the m_i scan. If the linear dispersion relation holds in all cases the inertial range of frequency spectra should shift to lower frequencies with increasing ion mass. Fig. 5.2.9 shows that it is actually the case.

5.3 Parallel Dynamics of Turbulence

So far the perspective has been limited to only one dimension in space, namely the poloidal direction. The next step was to use a more sophisticated experimental setup in order to construct a three-dimensional picture of turbulent structures. The motivation to study turbulence in three dimensions is given by the strong coupling of dynamics parallel and perpendicular to the magnetic field in the drift wave mechanism. The results presented so far strongly suggested drift wave turbulence to be dominant in WEGA. Therefore, a three-dimensional character of turbulence with a finite wavenumber parallel to \mathbf{B} was expected to be found.

Experimental results presenting details of the three-dimensional structure of plasma turbulence in toroidal magnetic confinement devices are very rare in literature. The results from different experiments don't reveal a unique picture, whether turbulence has a three-dimensional character with a finite parallel wavenumber (k_{\parallel}) or not. A two-dimensional character of turbulence with vanishing k_{\parallel} (within the error bars) has been observed at the tokamaks ASDEX [Rud90] and JET [Tho+02] and the stellarator W7-AS [Ble98]. A finite k_{\parallel} has been reported for the tokamaks TEXT [Rit+88] and TEXT-U [BWR98]. However, the observed values of k_{\parallel} in TEXT and TEXT-U differ by about one order of magnitude, what has been related to a better knowledge of the magnetic field topology in TEXT-U [Win+97; BWR98]. A common result from all experiments is that structures are strongly elongated in toroidal direction. Parallel correlation lengths are typically larger by at least two orders of magnitude than in the poloidal direction. A very detailed study of the parallel dynamics of drift wave turbulence has been performed at the TJ-K torsatron [Mah07; Mah+07].

For all experiments the spatial resolution in toroidal direction has been limited to two points due to the complex magnetic topology and limited experimental access to the machines.

The scope of toroidally resolved experiments presented in this work is to provide a detailed view into the three-dimensional structure of turbulence. However, the spatial resolution in toroidal direction was still limited to two points, reference probe and matrix. This limitation allows a proper interpretation of the results only on the basis of appropriate models. Heuristic models for the parallel properties of fluctuations have been introduced by Thomsen [Tho02]. A part of these models is discussed in the following to show which information about the three-dimensional structure of turbulence can be gained from the toroidally resolved experiments. The discussion is based on the assumption that drift waves are the underlying instability mechanism. As further limitations only drift wave theory for large scales ($k_{\theta}\rho_s \ll 1$) is considered, where the dispersion relation is linear, and no electromagnetic effects are expected (no Alfvénic activity).

5.3.1 Heuristic Model of Three-dimensional Drift-Wave Turbulence

For simplification the two-dimensional picture (toroidal-poloidal plane) of a coherent drift wave is considered first (see section 2.3.2). The plane is sampled at two toroidal positions. In the poloidal direction it is sampled once at the toroidal location of the reference probe and at multiple locations by the probe array. The geometry is depicted in fig. 5.3.1 (a). Using the matrix decomposition of a radial scan of the array (see section 4.4.4) an additional radial resolution would be given perpendicular to the viewing plane on the right hand side of the figure. This dimension is ignored for the sake of clarity. The position P_0 marks the point where a field line starting at the reference probe (P_{ref}) intersects the matrix. The data is now analysed by cross-correlating the reference probe with individual points in the matrix. The position where the highest correlation is found within the matrix is of particular interest. This may in general be shifted with respect to the intersection point P_0 by a certain length δ_θ . The highest cross-correlation for zero time lag occurs at P_1 which is aligned on the wave front crossing P_{ref} . Due to the finite parallel wavenumber, P_1 is displaced by a distance of $\delta_{\theta,0}$ against the intersection point of the field line (P_0). The method to derive information about the parallel wavenumber from this two point measurement in toroidal direction has been introduced by Ritz et al. [Rit+88]. The ratio k_{\parallel}/k_θ is given by the inclination angle ϑ , and can thus be derived from the knowledge of $\delta_{\theta,0}$ and the connection length L_c :

$$\frac{k_{\parallel}}{k_\theta} = \frac{\delta_{\theta,0}}{L_c} = \tan \vartheta. \quad (5.4)$$

A possibility for the direct measurement of k_{\parallel} is to determine the phase shift between P_{ref} and P_0 :

$$k_{\parallel} = \frac{\Delta\alpha}{L_c} \quad (5.5)$$

A simple estimation of k_{\parallel} can be given for the high field case from a fundamental assumption which underlies the Wakatani-Hasegawa drift wave turbulence model [WH84]. k_{\parallel} is assumed to be in the order of t/R where R is the major plasma radius². For WEGA parameters this estimation leads to $k_{\parallel} \approx t/R \approx 0.3 \text{ m}^{-1}$ and an expected perpendicular displacement of $\delta_{\theta,0} = \frac{k_{\parallel}}{k_\theta} L_c \approx 0.5 \text{ cm}$ with $k_\theta \approx 1 \text{ cm}^{-1}$. For low field a prerequisite of this model given by $\lambda_e < R/t$ is not fulfilled, where λ_e is the mean free path of the electrons.

Furthermore it is possible to derive the parallel phase velocity v_{\parallel} of the wave. v_{\parallel} is given from the time a wave front needs to propagate along \mathbf{B} from P_{ref} to P_0 . In the CCF between the two points this is the time lag of maximum cross-correlation τ_1 :

$$v_{\parallel} = \frac{L_c}{\tau_1}. \quad (5.6)$$

² $2\pi R/t$ is called field line connection length. One can visualise the meaning of this value for a resonant surfaces with $m = 1$. $2\pi R/t$ is in this case the length of a field line before it closes upon itself. The parallel wavelength cannot be longer than a the length of the closed field line.

For drift waves at large scales ($k\rho_s \ll 1$) the intrinsic parallel propagation velocity of drift waves is the ion sound velocity $c_s = \sqrt{T_e/m_i}$. Due to the finite inclination ϑ , v_{\parallel} is additionally affected by the poloidal phase velocity. The wavefront covers the distance L_c in parallel direction in the same time it covers $\delta_{\theta,0}$ in poloidal direction. The parallel velocity component owing from the projection of v_{θ} is given by:

$$v'_{\parallel} = \frac{L_c}{\delta_{\theta,0}} v_{\theta}. \quad (5.7)$$

For drift waves v_{θ} is given by the electron diamagnetic velocity. It has been found to be about 300 m/s for high field and some km/s for low field operation. Together with the estimated value of $\delta_{\theta,0} \approx 1$ cm a parallel phase velocity in the order of $v'_{\parallel} \approx 10^5$ m/s is to be expected. Hence, v'_{\parallel} is much higher than the ion sound velocity ($c_s \leq 1.5 \cdot 10^4$ m/s), yielding $v_{\parallel} \approx v'_{\parallel}$. At small scales ($k\rho_s \approx 1$) the parallel dynamics of drift waves is altered by coupling to Alfvén-waves. In this case v_{\parallel} may increase up to the Alfvén velocity given by $v_A = B/(\mu_0 n m_i)$.

The implications above are given for a planar wave at a certain frequency and wavenumber. However, they are also valid for turbulent fluctuations. Given that a clear dispersion relation is found, turbulence can be interpreted as an interaction of multiple waves in the broad band spectrum. In this case fluctuations appear as localised events with a finite correlation length in all three dimensions. The toroidal correlation length is expected to be about two orders of magnitude longer than in poloidal direction ($k_{\parallel}/k_{\theta} \approx 10^{-2}$). Hence, the structures are strongly elongated in parallel direction. This so called 'blob' representation of fluctuation events is illustrated in fig.5.3.1 (b). In this representation v_{\parallel} is an averaged phase velocity of structures, but can still be calculated from the time lag τ_1 of maximum correlation at P_0 . Eqn. (5.5) becomes the parallel dispersion relation $k_{\parallel}(\nu)$ with the cross-phase spectrum $\alpha(\nu)$ between P_{ref} and P_0 . Using eqn. (3.18) an average parallel wavenumber \bar{k}_{\parallel} can be specified from the average cross-phase. Assuming the wavefront of all contributing Fourier components to point in the same direction ($k_{\parallel}/k_{\theta} \neq f(\nu)$), the complete structure is tilted by ϑ with respect to the magnetic field. Evidence for the validity of this representation can be given from the cross-phase spectra in the triangle defined by P_{ref} , P_0 and P_1 . P_{ref} and P_1 are assumed to be aligned on the same wave front for all scales $\mathbf{k}(\nu)$. Therefore, the cross-phase $\alpha(\nu)$ is expected to tend to zero. A finite phase shift is expected for P_0 which is displaced normal to the wavefront. The normal distance from the wavefront is equal for the pathes $\overrightarrow{P_{\text{ref}}, P_0}$ and $\overrightarrow{P_1, P_0}$. Hence, similar cross-phases are expected along the legs of the triangle in fig. 5.3.1.

In this representation two cases have to be distinguished considering the statistical distribution of structures in space. A preferred toroidal phase velocity is inherent in this representation because all k_{\parallel} components of the spectrum point in the same direction. An additional component of the parallel dynamics is the growth of structures in time and thus a spatial expansion. The correlation maximum within the matrix undergoes a temporal evolution giving information about this statistical distribution. For fluctuations arising randomly at any point in toroidal direction the

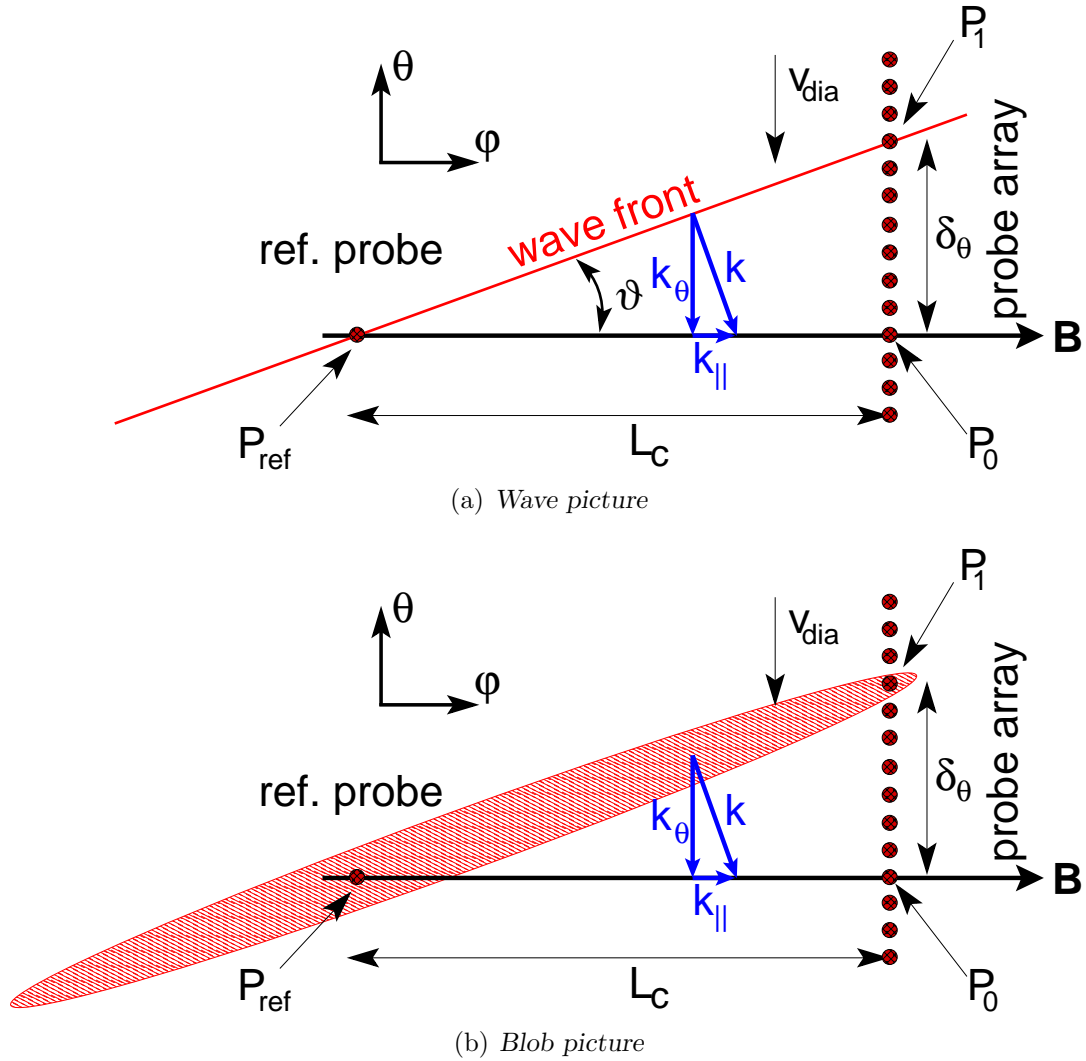


Figure 5.3.1: a) A coherent drift wave, with a wavefront slightly tilted with respect to \mathbf{B} is sampled by probes at two toroidal positions separated by the connection length L_c . P_{ref} and P_0 are aligned on a connecting field line. P_{ref} and P_1 are aligned on a wavefront. b) In case of turbulence no clear wave front exists, but structures elongated along \mathbf{B} (blob). Correlation cross spectral analysis yields information about the average dynamics of turbulence.

correlation function would on average see a structure which appears between the two toroidal positions under observation. The highest correlation in the matrix would in this case occur at zero time lag at P_1 . A different concept is that fluctuations appear preferably in a certain region along the magnetic field line. This assumption is not unrealistic because a strong poloidal asymmetry of fluctuation properties is a common observation in fusion devices [LL87; Fen+00; Kir+05; Mah07]. Poloidal asymmetries are always linked to asymmetries along the magnetic field line by the rotational transform which leads to a connection of different poloidal regions along the magnetic field line. However, a preferred occurrence of fluctuations at a certain point, and an expansion from this point would lead to a finite time lag of maximum cross-correlation between reference and matrix. This time lag (called τ_2 subsequently) occurs at any position in the matrix along the path of the structure.

A more complicated picture results if the assumption of the ratio k_{\parallel}/k_{θ} being constant for all frequency components does not hold. An example is an equally distributed spectrum of parallel wavenumbers without a preferred direction. This may result in vanishing values of $\delta_{\theta,0}$ and τ_1 . In this case no detailed information about the parallel dynamics of turbulence can be retrieved from the correlation function. The broad spectrum of k_{\parallel} would lead to a broadening of the cross-correlation function between P_{ref} and P_0 .

5.3.2 Field Line Tracing

A prerequisite for the construction of a three-dimensional picture of turbulence is a precise knowledge of the magnetic topology. The statistical analysis of raw data is based on a two point measurement with probes aligned on a connecting line. The expected effect is a small shift of turbulent structures with respect to the connecting field line. A field line tracing code was used to find magnetic configurations where a magnetic field line starting at the reference probe should intersect the path of the array. However, these calculations were not taken as the basis for toroidally resolved experiments. Relying on these calculation introduces an error which is hard to quantify. The absolute positions of both, reference probe and array, would need to be known exactly with respect to the magnetic field coil system. Additionally the absolute currents in the coil systems had to be known precisely. The effect of small misalignments of probes on the results of toroidally resolved measurements has been discussed by Thomsen et al. [Tho+01] for the case of a time dependent field perturbation in a tokamak. However, in a low β stellarator like WEGA³ it is possible to determine connecting field lines experimentally. Due to the low plasma pressure in WEGA, which can be assumed to be negligible compared to the magnetic pressure, the vacuum magnetic configuration is assumed to be equal to the situation with plasma. Determining connecting field lines experimentally has the great advantage that only the relative positions of the probe tips have to be known. These positions just have to be reproducible, what actually is the case for the manipulators used in WEGA to move probes into the plasma. The same holds for the coil currents. Small

³ β was below 10^{-4} for the experimental conditions considered here.

deviations between experimental currents and those used for code calculations would immediately introduce a systematic misalignment of probes. Using experimental field line mapping technology as reference only the relative error of the measured current and its reproducibility are important. The very accurate reproducibility of coil currents in WEGA is known from the experience of more than 25000 discharges.

Experimental field line mapping is based on the electron beam technique which has also been used for flux surface measurements. To this end the reference probe was replaced by an electron gun. The latter injected an electron beam into the vacuum magnetic field parallel or antiparallel to \mathbf{B} . The gun was placed roughly where calculations predicted the existence of a connecting field line to the matrix. The beam with a width of ≈ 2 mm followed a field line and could be detected by the array. The mapping was done in two steps. First the beam path was visualised in a background gas at a low neutral pressure. (Ar at a pressure of $p_N \approx 10^{-3}$ Pa). The beam energy was set to 40 eV with a total beam current of some 10 μA . The beam current was estimated from the total emission current of the filament. The interaction of the electron beam with the background gas leads to a collisional excitation of the background gas in the vicinity of the beam. The consequence is the emission of visible light along the path of the beam which can be monitored with a standard video camera. The parameters were set in a manner that only one single toroidal turn of the beam was visible. A sample snapshot of the beam taken with a camera looking tangentially into the vessel onto the array is shown in fig. 5.3.2. The picture is quite noisy due to the small amount of light available. But the path of the beam is clearly visible. If the gun is positioned properly the beam intersects the path of the array. The photograph in fig. 5.3.2 was taken with the array fully inserted into the vessel. In this case the electron beam was cut by the probe shaft as indicated in the picture. Since the gun was mounted on a slowly moving manipulator controlled by a stepping motor its position could be kept fixed at this location. In this phase it was still unknown at what position the beam intersects the matrix. So the next step was to detect the beam on the matrix. To this end the beam intensity was reduced in order to get a better focussing by reducing space charge effects in the beam. With the probes of the array connected to the ground potential the electron current on the probes could be measured in a radial scan. Fig. 5.3.3 shows the beam intensity as it was detected by the probes. The intersection point of the electron beam can be clearly seen as a strong local increase of the signal intensity. These experiments provided the information necessary to undertake toroidally resolved measurements. The electron gun was replaced by a Langmuir probe again acting as reference probe for correlation analysis. The tip of the reference probe could be placed at the position determined before with high accuracy of about ± 1 mm. A field line starting at the reference probe intersects the matrix at the coordinates where the electron beam was detected. With the help of this field line mapping technique different connecting field lines were determined. Two of the field lines lying approximately on the same flux surface were selected for the plasma experiments. The first one intersects the matrix in the equatorial plane at $z = 0$, the second one near the lower end of the matrix at $z = -2.5$ cm. The considered

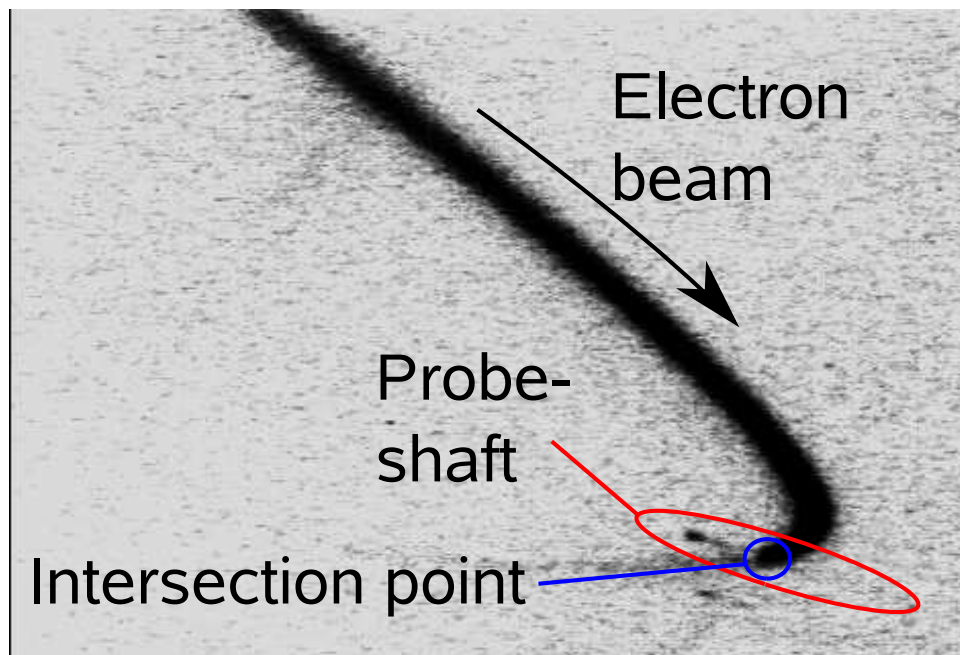


Figure 5.3.2: Snapshot of the electron beam used to determine connecting field lines experimentally. The beam starting at the reference probe intersects one of the probe shaft in the array. The picture shows a tangential view into the vacuum vessel taken from the low field side.

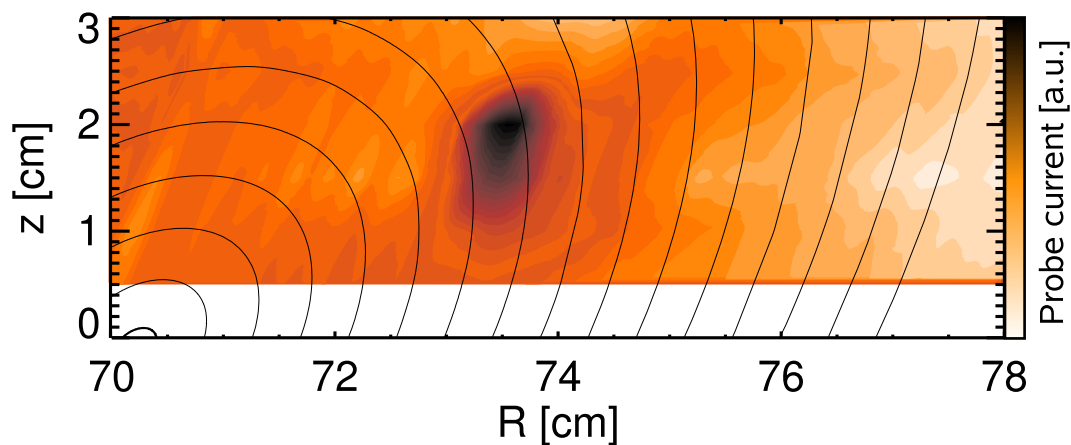


Figure 5.3.3: Visualisation of the electron beam detected by the probe array. Only the part of the matrix is shown, where the beam was found. The intensity of the current detected by the probes is colour coded. The dark region marks the highest intensity where the beam intersects poloidal plane covered by the array. The picture shows an example, where the intersection point is deep in the plasma core.

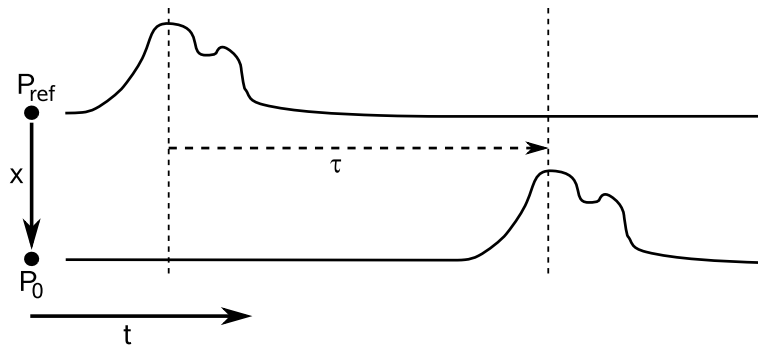


Figure 5.3.4: Definition of positive propagation direction if the maximum in the CCF is found for positive time lag. An arbitrary signal shape is assumed to propagate in space from P_{ref} to P_0 .

flux surface is about 5 mm inside the LCFS. All experiments are undertaken at a magnetic configuration with $t_0 = 0.224$ on axis. The resonant $t = 1/4$ surface with the corresponding island chain is outside the LCFS for this configuration (verified by flux surface measurements). A comparison between experimental mapping and calculations shows a discrepancy of $\gtrsim 5$ mm for the intersection point. The reason for this discrepancy is probably a sum of several small systematic errors. The absolute positioning of the reference probe and the array as well as an erroneous absolute coil current contribute to this error. Simulations have shown, that a relative error of only $\approx 2\%$ in one magnetic field component (i.e. toroidal or helical field) can explain the observed discrepancy. This shows the importance of the experimental field line mapping because the perpendicular shift of turbulent structures versus the intersection point of the connecting field line, $\delta_{\theta,0}$, is expected to be in the order of the discrepancy.

5.3.3 Results from High Field Operation

In the following, results from toroidally resolved experiments in He at high field are presented. All experiments were conducted with the results from the field line mapping as the basis for the quantitative analysis. The magnetic configuration was fixed at a rotational transform of $t_0 = 0.224$ and the two positions of the reference probe given above were used. A technical detail relating the correlation analysis needs to be explained before presenting the results. The CCF is not sensitive to any absolute times but only to the relative time lag which may be positive or negative. The time lag of maximum correlation between data sets from different points in space reflects the propagation of fluctuations from one point to another. It is a matter of definition which propagation direction yields a positive time lag. Fig. 5.3.4 explains the definition used for the toroidally resolved measurements presented below. A structure which is first observed in time at the reference probe and later at the matrix leads to a positive time lag of highest correlation and vice versa. In units

of the toroidal angle coordinate φ , the positive direction is counter clockwise. This definition is independent of the direction of the magnetic field vector.

5.3.3.1 Temporal Evolution of Turbulent Structures

The matrix decomposition of a radial scan was used to reconstruct average fluctuation events in the poloidal plane covered by the array as explained in sec. 4.4.4. Fig. 5.3.5 shows the CCF between the reference probe and individual points in the matrix. Each plot is a snapshot for a fixed time lag. The black star at $R = 78.9$ cm, $z = -2.5$ cm marks the intersection point of the field line starting at P_{ref} . The correlation function was evaluated for two identical discharges and averaged in order to get a slightly smoother result. Information about the dynamics of turbulence in the poloidal plane can be gained from the series of snapshots for increasing time lags in fig. 5.3.5. At $\tau < -80 \mu\text{s}$ a structure enters the observed window at the upper end. With increasing time lag the correlation amplitude in the centre of the structure continuously increases until a certain point and finally decreases again, reflecting the lifetime of the structure. During its lifetime the structure propagates in poloidal direction following the flux surface shape. This was the deferred verification for the lifetimes given in section 5.2. No radial velocity component was observed which could affect poloidally resolved measurements. The poloidal correlation length of $d_\theta \approx 2$ cm was also verified. In radial direction the correlation length was shorter, $d_r \approx 1$ cm. Hence, structures were elongated in poloidal direction by a factor of about 2.

The colour coding in fig. 5.3.5 yields the time lag of maximum correlation between $\tau = -20 \dots 0 \mu\text{s}$. A different representation of the temporal evolution of structures is shown in fig. 5.3.6. It shows the highest correlation amplitude within the matrix as a function of the time lag. Additionally, the poloidal distance of this maximum from the intersection point of the connecting field line is plotted. The temporal evolution of the correlation maximum clearly shows the growth of structures up to a relative correlation of about 60% and the following decay. The inclination of $\delta_\theta(\tau)$ reflects the poloidal velocity of structures. v_θ was constant in the observed window. A linear fit resulted in $v_\theta \approx 300$ m/s. This value is $\approx 50\%$ higher than the value given in section 5.2.2 for a He discharge at high field, what could be accounted for the different magnetic configuration (t was higher here). A higher t typically leads to steeper density gradients in WEGA, and hence to a larger diamagnetic drift velocity.

The most interesting information that can be gained from fig. 5.3.6 comes from the time lag of maximum correlation, labelled τ_2 following the definition given in section 5.3.1. τ_2 clearly deviated from zero. The maximum was found at: $\tau_2 = (-12 \pm 2.2) \mu\text{s}$. The given error is the standard deviation of τ_2 deduced from individual discharges and thus a measure for the statistical scatter of data. Following the definition given above the negative value means that structures were on average first observed at the matrix and delayed by τ_2 at P_{ref} . This result gives evidence that fluctuation events did not arise randomly at any position. They preferably appeared at the toroidal position of the matrix and expanded from there. No infor-

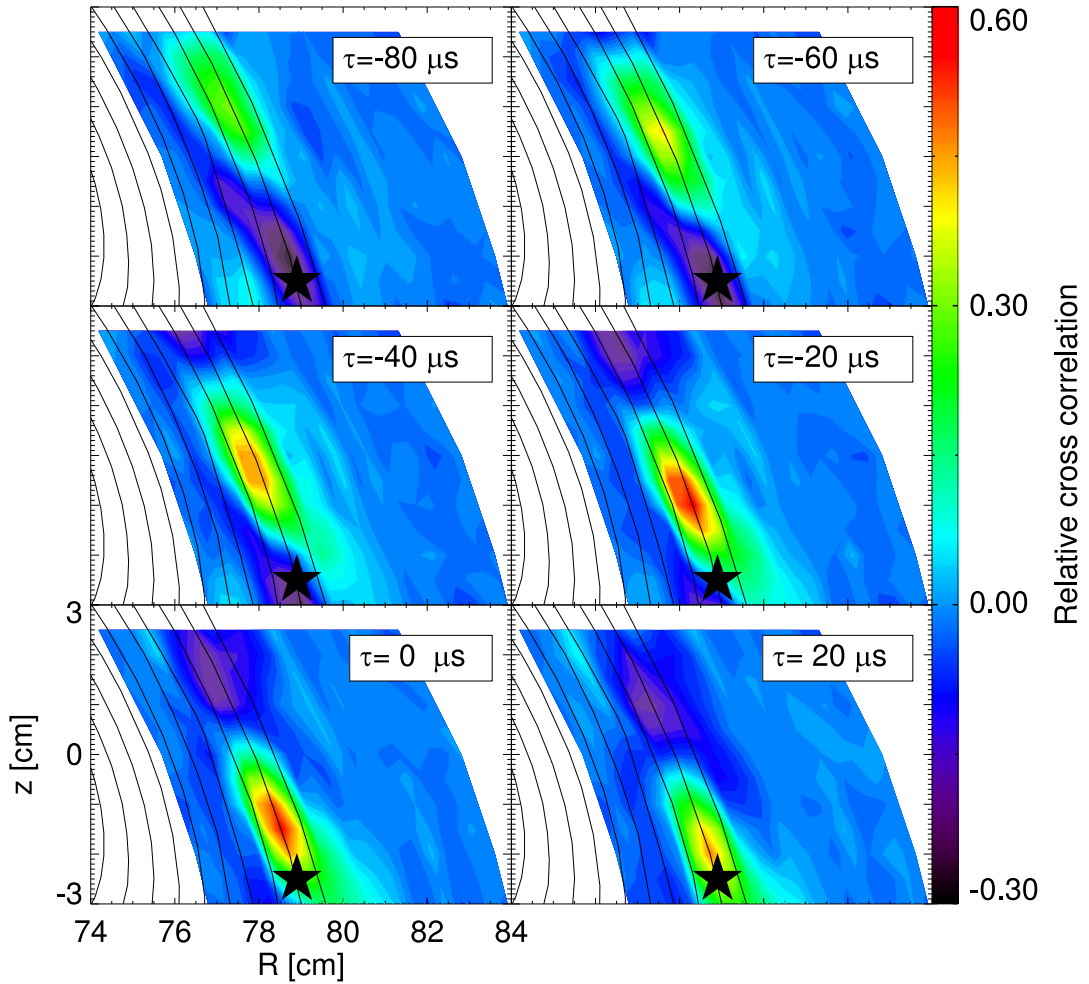


Figure 5.3.5: Cross-correlation function between the data from the ref. probe and individual subwindows in the matrix. The black star marks the intersection point of the connecting field line starting at the ref. probe with the matrix. The temporal evolution of the observed structures is illustrated as a series of snapshots in the $R - \theta$ -plane for different time lags τ . The structure propagates along a flux surface (black lines) in electron diamagnetic drift direction. The figure does not represent the dynamics of an individual blob but a statistical average.

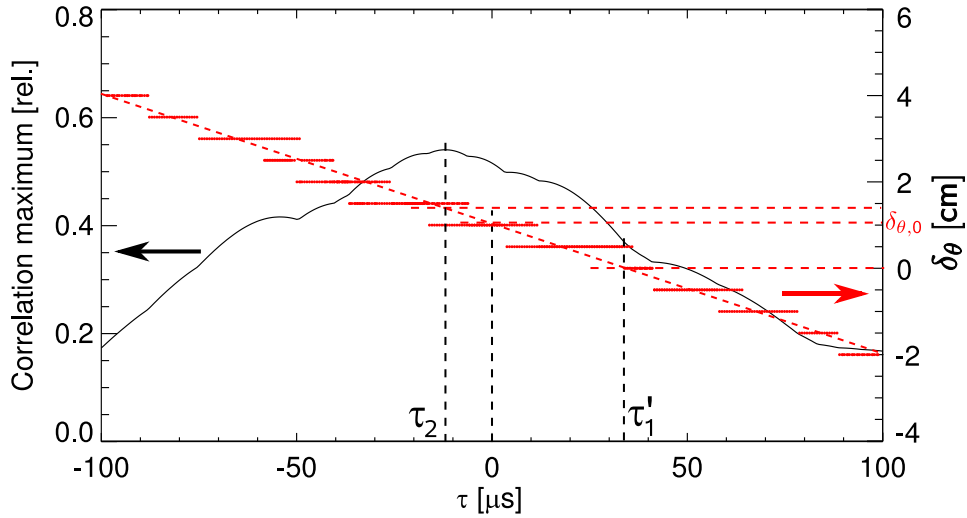


Figure 5.3.6: Temporal evolution of the correlation maximum in fig. 5.3.5. The black curve shows the correlation maximum in the centre of the structure, in red the position of the maximum is shown. The graphs represent an average over four discharges, two for each positions of the reference probe. The black line is averaged over the four discharges, in red datapoints all datapoints from the individual discharges are plotted. The given value δ_θ is the distance between the correlation maximum and the intersection point of the connecting field line along a flux surface. The highest correlation is observed at τ_2 . At $\tau = 0$ the centre of the structure is displaced from the intersection point by $\delta_{\theta,0} \approx 1$ cm.

mation about the symmetry of expansion could be gained from these experiments because no further measurement points but the reference probe were available. The spatial homogeneity observed in poloidally resolved measurements (see section 5.2.1) was obviously valid only in a limited section like the sampling region of the array and not for a complete poloidal turn. The observation of a finite τ_2 , however, does not allow to give quantitative information about the expansion time of structures. It only shows that there was an asymmetry and fluctuations arose on average closer to the array than to the reference probe.

Information about the average parallel wavenumber can be gained from both fig. 5.3.5 and 5.3.6. We consider now the centre of the structure at zero time lag. It was found to be displaced from the intersection point by $\delta_{\theta,0} = (1.1 \pm 0.3)$ cm. The error results from the spatial resolution which was 0.5 cm and 0.3 cm in poloidal and radial direction, respectively. Hence, in the blob representation presented above the structure was tilted with respect to the connecting field line by a small angle ϑ . Following eqn. (5.4) the ratio between the average parallel and perpendicular wavenumber was:

$$\frac{\bar{k}_{\parallel}}{\bar{k}_{\theta}} = \tan \vartheta = \frac{\delta_{\theta,0}}{L_c} = \frac{(1.1 \pm 0.3)}{170} = (0.6 \pm 0.17) \cdot 10^{-2}.$$

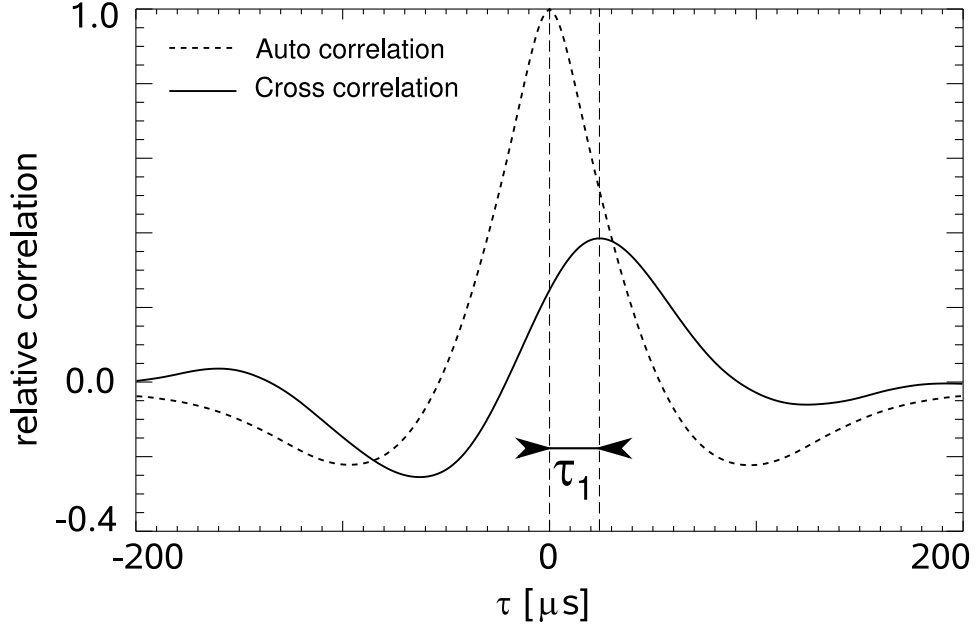


Figure 5.3.7: Temporal cross-correlation function between data from P_{ref} and P_0 (solid line). The dashed line reflects the averaged auto-correlation function for both points. The results were again averaged over four discharges, two for each position of the reference probe. The maximum in the CCF is observed at a finite time lag of τ_1 , corresponding to a finite parallel phase velocity of structures.

A quantitative evaluation of absolute values of k_{\parallel} from cross spectral analysis is given in the subsequent section.

The next step was to look at the cross-correlation function between P_{ref} and P_0 which were aligned on the same field line. Fig. 5.3.7 shows the cross-correlation together with their auto-correlation function. Auto- and cross-correlation function show nearly the same width. The cross-correlation maximum was relatively small ($\approx 40\%$) because the structure was already collapsing when it passed P_0 at a time lag of $\tau_1 = (24.3 \pm 2.6) \mu\text{s}$. τ_1 determines the averaged parallel phase velocity of structures:

$$v_{\parallel} = \frac{L_c}{\tau_1} = \frac{170 \text{ cm}}{(24.3 \pm 2.6) \mu\text{s}} = (7 \pm 0.74) \cdot 10^4 \text{ m/s}.$$

Hence, the parallel phase velocity of structures has a preferred direction, which points from P_{ref} towards P_0 . The contribution of the poloidal phase velocity to the parallel phase velocity was:

$$v'_{\parallel} = v_{\theta} \frac{L_c}{\delta_{\theta,0}} = 300 \frac{\text{m}}{\text{s}} \frac{170}{1.1 \pm 0.3} = (4.6 \pm 1.3) \cdot 10^4 \text{ m/s}.$$

Within the error bars the difference between v_{\parallel} and v'_{\parallel} was in the order of the ion sound velocity $c_s \approx 1.5 \cdot 10^4 \text{ m/s}$, which additionally affects the parallel propagation of structures. Due to the parallel dynamics of structures τ_1 is not necessarily the

time when the centre of the structure passes P_0 as assumed in eqn. (5.7). In fig. 5.3.6 it can be seen that the structure passes the intersection point at a time lag of $\tau'_1 \approx 34 \mu\text{s}$. This results in $v'_\parallel = L_c/\tau'_1 = 5 \cdot 10^4 \text{ m/s}$, in good agreement with the estimation from $v_\theta L_c/\delta_{\theta,0}$. As expected for the large scales under consideration ($\bar{k}_\theta \rho_s \ll 1$) the parallel phase velocity is far below the Alfvén velocity, which is given as the upper limit of v_\parallel for small scales. For the given discharge conditions the Alfvén velocity was in the order of $v_A \approx 10^6 \text{ m/s} \gg v_\parallel$.

5.3.3.2 Parallel and Perpendicular Dispersion Relation

More quantitative results on k_\parallel and about the validity of the model description of three-dimensional turbulence could be derived from cross spectral analysis. In section 3.3.4 it was shown that the spectral power of turbulence in $k_\theta \nu$ -space was distributed around a well defined dispersion relation, which was in agreement with drift wave theory. This allows the interpretation of cross-phase spectra from poloidally separated points as dispersion relation following $k_\theta(\nu) = \alpha(\nu)/\Delta y$, where Δy is the spatial separation of measurement points. This relation can be generalised to any spatial direction. In the triangle $\{P_{\text{ref}}, P_0, P_1\}$ in fig. 5.3.1 the cross-phase between P_{ref} and P_0 then reflects the parallel dispersion relation, $k_\parallel(\nu) = \alpha_\parallel(\nu)/L_c$. k_θ is derived from P_1 and P_0 . If the assumptions made in the description of the blob representation are valid, $k_\theta(\nu)$ and $k_\parallel(\nu)$ should coincide. Furthermore the phase shift between P_{ref} and P_1 should vanish because both points are assumed to be aligned on the same wavefront for all Fourier components contributing to the turbulent spectrum. Fig. 5.3.8 shows the cross-phase spectrum, together with the corresponding coherence spectrum for all three legs of the triangle. For the given probe distance, a significant coherence for this type of discharge was observed only for frequencies up to $\nu \approx 8 \text{ kHz}$. In this range the good agreement between poloidal and parallel cross-phase is apparent. Both show a similar shape. The vanishing cross-phase between P_{ref} and P_0 verifies the assumption that in the given frequency range of significant coherence both probe tips are aligned along a wavefront. The ratio k_\parallel/k_θ was independent of the frequency. This allows the interpretation of the results in a manner that turbulent structures can be explained as the interaction of modes with parallel wavefronts. A small phase shift along the line, claimed to be a wavefront, was remanent. This was on the one hand due to the typical jitter in turbulent spectra. On the other hand the limited spatial resolution did not allow a perfect alignment of two probes an a wavefront. P_1 was solely the point of highest correlation in the matrix at $\tau = 0$.

To come to a quantification of k_\parallel the cross-power weighted average parallel wavenumber was calculated using eqn. (5.5). The parallel phase spectrum from fig. 5.3.8 yields an average cross-phase of $\bar{\alpha} = 0.869 \pm 0.067$, corresponding to an average parallel wavenumber of

$$\bar{k}_\parallel = \bar{\alpha}/L_c = (0.51 \pm 0.04) \text{ m}^{-1}.$$

This result is in the order of $t/R \approx 0.3 \text{ m}^{-1}$, implying that the averaged parallel

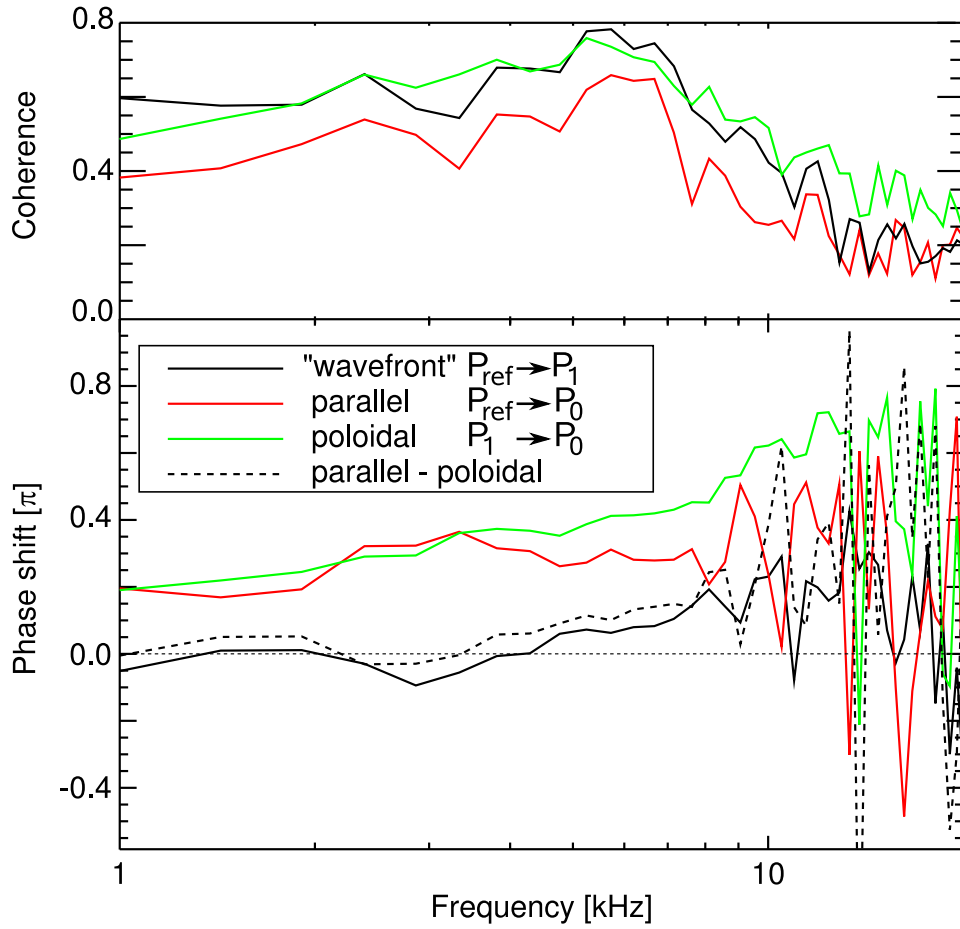


Figure 5.3.8: Cross-phase spectra of probes in the triangle defined by P_{ref} , P_0 and P_1 . All three phase spectra show a well defined shape in the frequency range below $\nu \approx 10$ kHz. P_{ref} and P_1 are obviously aligned on a wavefront for all frequency components, since their cross-phase vanishes. The legs in the triangle aligned parallel and perpendicular to \mathbf{B} show similar phase behaviour.

wavelength is in the order of the system size defined by the field line connection length.

5.3.4 Results from Low Field Operation

The parallel turbulence dynamics was also studied for the low field case. The ratio I_H/I_T could be kept constant in order to achieve the same connecting field lines as in the high field case. A strong difference of the turbulence dynamics compared to the high field case was found in section 5.2. The following section shall answer, whether the linear scaling observed for poloidal wavenumbers at different magnetic field strengths also holds for the parallel component. Furthermore it is to be answered whether the turbulence with poloidal structure sizes comparable to the machine

dimensions can be described by the same model as in the high field case.

5.3.4.1 Temporal Evolution of Turbulent Structures

The general information about the temporal evolution of structures that can be gained from the CCF between the reference probe and the matrix was, at first sight, comparable to the results from high field discharges. Structures, propagating in the electron diamagnetic drift direction during the process of growth and decay were observed. Fig. 5.3.9 shows a snapshot of the CCF at $\tau = 0$. Due to the large poloidal correlation length, which was already observed in poloidally resolved measurements, the structure could not be fully resolved in the observation window. The structure was more strongly elongated in the poloidal direction than at high field. The evaluation of τ_2 from the maximum of the CCF in the matrix showed as a universal feature of WEGA that fluctuation events preferably arise closer to the array. τ_2 was of the same order as in the high field case and also negative. Identical experiments were undertaken at an inverted magnetic field to give evidence for the universal character of this observation, . The magnetic topology remains constant if both, I_T and I_H are inverted. The result of these experiments was that τ_2 remained negative. Hence, structures arose on average first at the matrix and expanded towards the reference probe, independently of the orientation of the magnetic field vector. This effect is very likely linked to the magnetic field line curvature, which is unfavourable at the position of the matrix. Field lines departing from the matrix pass the reference probe on their way to regions of favourable curvature regions. Hence, turbulent structures in WEGA preferably arise in the region of unfavourable curvature.

The centre of the structure in fig. 5.3.9 is shifted versus the intersection point by $\delta_{\theta,0} = (2.2 \pm 0.7)$ cm, yielding a ratio between average parallel and poloidal wavenumber of $\bar{k}_{\parallel}/\bar{k}_{\theta} = (1.3 \pm 0.4) \cdot 10^{-2}$. Taking the scaling of k_{θ} observed in section 5.2 into account, this leads to contradictory results:

- The ratio $\bar{k}_{\parallel}/\bar{k}_{\theta}$ was in the same order for low and high field.
- The inverse poloidal structure size, and therefore also \bar{k}_{θ} was found to scale approximately linearly with B .
- This yields an estimated average parallel wavenumber of about $\bar{k}_{\parallel} \approx 0.06 \text{ m}^{-1}$.

The latter would yield an average parallel wavelength of $\bar{\lambda}_{\parallel} \approx 100$ m, covering about 20 toroidal turns. The contradiction is that - roughly speaking - when $\bar{\lambda}_{\parallel}$ is related to the parallel extent of structures, such a huge structure could not fit into the machine. Due to the poloidal structure size at low field, which was large compared to the plasma size ($d_{\theta} \approx 14$ cm), the structure would interfere in a poloidal plane several times. The effect of the self-interference of structures is indicated in fig. 5.3.10.

The flux surface under consideration is simplified to a circle with a radius of $r_{eff} \approx 10$ cm. The hump labelled *1* indicates a turbulent structure with a poloidal

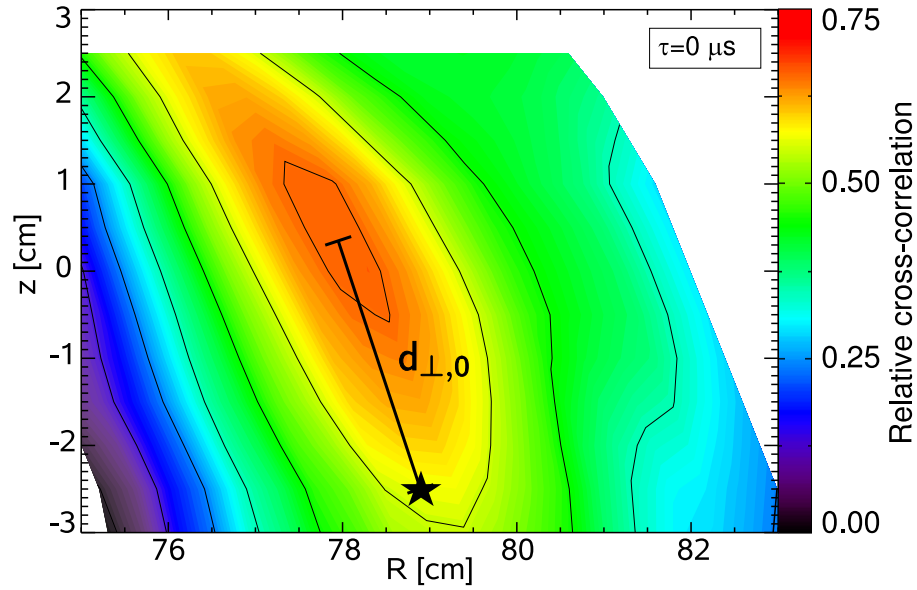


Figure 5.3.9: Snapshot of the cross-correlation function between the reference probe and the matrix at $\tau = 0$ for a He discharge at low field

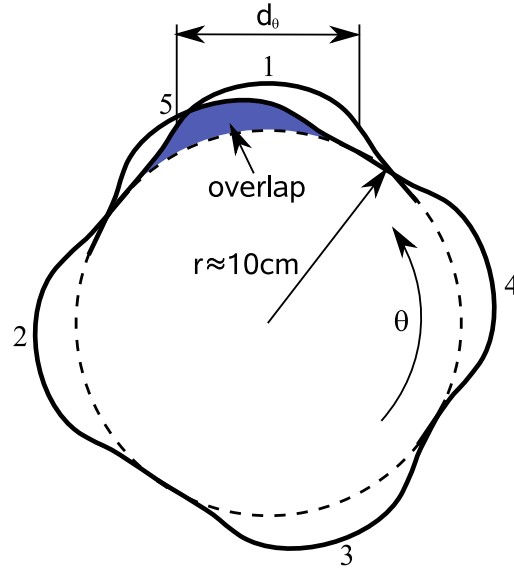


Figure 5.3.10: The problem of structures overlapping in a poloidal plane. A simplified circular flux surface with $r_{eff} \approx 10$ cm is indicated by the dashed line. Turbulent structures are indicated by the humps on the flux surface. At low field the poloidal structure size is about $1/4$ of a poloidal circumference. A structure being strongly elongated along \mathbf{B} will cross the same poloidal plane at a poloidal angle distance of about $2\pi t$. Hence, at $t \approx 1/4$ a structure with a toroidal extent $> 2\pi R/t$ would intersect itself after 5 toroidal turns.

width of $d_\theta \approx 14$ cm. Due to the strong parallel elongation, the rotational transform of $t \lesssim 0.25$, and the finite inclination of the structure with respect to a magnetic field line, the structure would reappear in the same plane shifted in poloidal direction by $\theta \gtrsim 45^\circ$ (structure labelled 2). The structure crosses the poloidal plane several times until an overlap appears already at the fifth intersection. Besides this pictorial description of self-interfering structures, turbulence with parallel wavenumbers larger than the magnetic field line connection length ($\bar{k}_\parallel > t/R_0$) leads to conflicts in the equations governing the turbulence dynamics if there is not enough space in the poloidal direction [Sco97a]. Larger values of \bar{k}_\parallel which fit into the system without an overlap would yield a perpendicular shift of structures in the order of $\delta_{\theta,0} \approx 10$ cm, and would therefore not be detectable anymore.

5.3.4.2 Parallel and Perpendicular Dispersion Relation

The relation of cross-phase spectra in the triangle P_{ref}, P_0, P_1 should clarify, whether the same model description is valid for both low and high field, despite the problem of self-interfering structures. Fig. 5.3.11 shows the result of the cross spectral analysis. The phase shift in poloidal direction is rather small, as expected since the poloidal separation of the probes under consideration ($\delta_{\theta,0} \approx 2$ cm) was much smaller than the poloidal correlation length ($d_\theta \approx 14$ cm). This is also reflected by the high coherence, which was close to unity in the observed frequency range. A completely different shape of both coherence and cross-phase spectrum was observed in the parallel direction. In striking contrast to the high field case the coherence between toroidally separated probes was almost completely lost for frequencies higher than $\nu \approx 4$ kHz, although both probes showed similar auto-power spectra, which were flat up to $\nu \gtrsim 10$ kHz. In the frequency range of high coherence the parallel cross-phase showed a well defined shape, but changed sign from negative values at very low frequencies to positive values at higher frequencies. By definition, a negative phase shift represents a wavenumber component pointing from the matrix to the reference probe and vice versa. The conclusion to be drawn from this result is that the observed turbulent structures at low field in WEGA cannot be described in the same manner as in the high field case. The blob representation, describing turbulence of an interaction of waves with parallel wavefronts, does not hold anymore. Fig. 5.3.12 shows a further heuristic model describing the observations better. The turbulent structure in the revised model is still interpreted as an interaction of waves. The inclination of the individual wavefronts with respect to the magnetic field vector is not constant anymore, but a function of the frequency ($\vartheta = f(\nu)$). The observed perpendicular shift of the structure at $\tau = 0$ shows that there is still a preferred direction for k_\parallel , i.e. the centre of mass of parallel wavenumber spectrum is not at $\bar{k}_\parallel = 0$.

The average parallel cross-phase, formally derived from eqn. (3.18) for the spectra shown in fig. 5.3.11, was rather small and corresponded quite well to the average poloidal cross-phase. The spectra yield average parallel and poloidal wavenumbers of

$$\bar{k}_\parallel = (0.085 \pm 0.035) \text{ m}^{-1} \quad \text{and} \quad \bar{k}_\theta = (0.08 \pm 0.009) \text{ cm}^{-1},$$

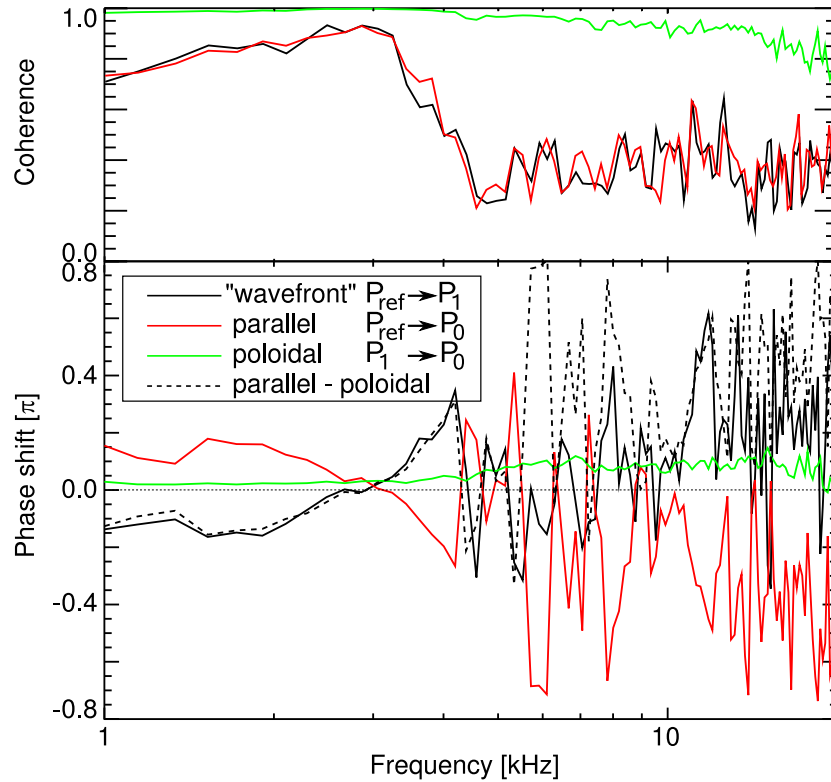


Figure 5.3.11: Results from cross spectral analysis in the same notation as in fig. 5.3.8. A significant coherence between toroidally separated probes is observed only for very low frequencies, whereas the poloidally separated probes are almost fully coherent over the whole observed frequency range. Furthermore the cross-phase between P_{ref} and P_1 does not vanish but show a shape crossing zero at $\nu \approx 3$ kHz.

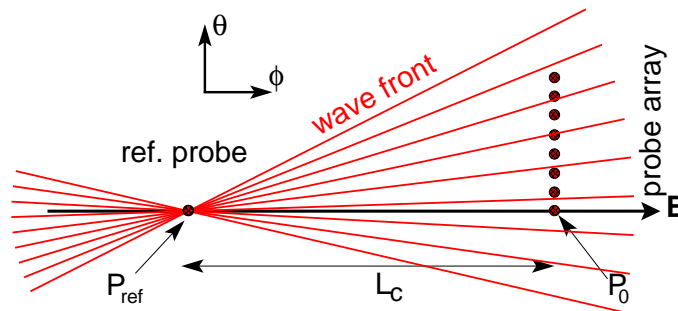


Figure 5.3.12: Modification of the previously presented heuristic models. A possible explanation for the observed phase spectra is a broad distribution of parallel wavenumbers with Fourier components parallel and antiparallel to \mathbf{B} . The observed structure is then the result of the interaction of wavepackets with wavefronts tilted by a varying angle $\vartheta = f(\nu)$ with respect to \mathbf{B} .

respectively. The ratio $\bar{k}_{\parallel}/\bar{k}_{\theta}$ agrees satisfactorily with the results from the correlation analysis ($\bar{k}_{\parallel}/\bar{k}_{\theta} = \delta_{\theta,0}/L_c$).

5.4 Summary of Major Results

The studies of turbulent plasmas in WEGA concentrated on magnetic configurations with low rotational transform ($t < 0.3$), where the plasma was generally found to be in a state of fully developed turbulence. The major results are listed in this section.

General Characterisation

- i. The PDF of fluctuations was found to be close to Gaussian distribution for density, potential and electric field fluctuations. The PDF of the radial $\mathbf{E} \times \mathbf{B}$ flux strongly deviated from Gaussian distribution. Skewness and kurtosis of the flux showed positive values indicating a net transport pointing radially outwards and an intermittent character of transport.
- ii. Fluctuations were found to be mainly driven by the density gradient. Under discharge conditions, where the gradient region covered almost the whole plasma cross section, the fluctuation amplitude was found to be higher in the centre, where the magnetic shear is lower than in the edge.
- iii. The cross-phase between density and potential fluctuations was found to be small ($\bar{\alpha} \lesssim \pi/4$) in the whole plasma cross section.

Perpendicular Dynamics

- iv. The poloidal phase velocity of structures was found to point in the electron diamagnetic drift direction inside the LCFS. In the high field case, v_θ changed sign close to or just outside the LCFS. The change in sign could be related to the poloidal $\mathbf{E} \times \mathbf{B}$ drift caused by stationary radial electric fields, which dominated the dynamics in the SOL. The absolute value of v_θ inside the LCFS was in the order of some 100 m/s for the high field case and some km/s for the low field case. Hence, it was nearly proportional to $1/B$.
- v. The lifetime of turbulent structures, i.e. the autocorrelation time in the co-moving frame, was in the order of $\tau_L \approx 100 \mu\text{s}$. This value was found to be rather universal for WEGA, as no systematic dependence on the plasma parameters was found.
- vi. The poloidal structure size, represented by the poloidal correlation length at zero time lag (d_θ), was found to scale nearly linearly with the inverted magnetic field strength. For high field small structures with $d_\theta = (2 \pm 0.25)$ cm were observed. In the low field case the structure size was $d_\theta \approx 14$ cm, hence, it was comparable to the plasma dimensions.
- vii. The correlation length remained constant when the ion mass was changed at constant magnetic field strength. This observation was made at low as well as at high field. The poloidal correlation function at zero time lag as well as the poloidal wavenumber spectra coincided for different m_i .

Parallel Dynamics

- viii. Very detailed studies of the parallel dynamics of turbulence were performed for the low and the high field case. The results were interpreted based on heuristic models. Magnetic field lines connecting two toroidally separated probes with a connection length of $L_c = 170$ cm were determined experimentally.
- ix. A finite average parallel wavenumber was found for both cases. The ratio between average parallel and poloidal wavenumber $\bar{k}_{\parallel}/\bar{k}_{\theta}$ was $(0.6 \pm 0.17)10^{-2}$ in the high field case and $(1.3 \pm 0.4)10^{-2}$ in the low field case. The given values were deduced from the inclination of the turbulent structure with respect to the magnetic field vector.
- x. Turbulent structures showed a three-dimensional character. The cross-correlation function between toroidally separated probes showed the maximum at finite time lag, indicating an anisotropy in the occurrence of fluctuation events. Fluctuations arose preferably on the high field side of the torus. The observation was found independent of the direction of the magnetic field vector, and for both low and high field.
- xi. The parallel phase velocity in the high field case was $v_{\parallel} = (7 \pm 0.74)$ m/s. This value is in-between the ion sound and the Alfvén velocity.
- xii. The average parallel wave number at high and low field was $\bar{k}_{\parallel} = 0.51 \pm 0.04$ m⁻¹ and $\bar{k}_{\parallel} = (0.085 \pm 0.035)$ m⁻¹, respectively. The values were derived from the cross-power weighted average cross-phase between signals from two spatially separated probes. The corresponding average poloidal wavenumbers yielded in both cases the same ratio $\bar{k}_{\parallel}/\bar{k}_{\theta}$ as derived from the cross-correlation function.
- xiii. The results from the high field case allowed an interpretation of turbulence according to the heuristic model introduced in sec. 5.3.1. As assumed in the underlying model, the cross-phase between the reference probe and the point of highest correlation at zero time lag in the matrix vanished within the errors for all frequency components of significant coherence. Hence, the observed turbulent structure may be described as an interaction of waves with parallel wavefronts. The ratio k_{\parallel}/k_{θ} was constant along the frequency spectrum.
- xiv. The same model could not be applied to the results from low field. A significant coherence between toroidally separated probes was found only in a rather narrow frequency band ($\nu \lesssim 4$ kHz), whereas poloidally separated probes were almost fully coherent up to some 10 kHz. Within the narrow coherent frequency band a systematic variation of the ratio k_{\parallel}/k_{θ} was found, indicating a broad spectrum of parallel wavenumbers with components pointing both parallel and antiparallel to the magnetic field vector.

5.5 Conclusions and Outlook

Confirmation of the 'Drift Wave Picture'

Drift waves have been expected to be the dominant instability driving turbulence in the WEGA stellarator. This assumption could be verified within this work. The main features of drift waves were observed, and the dynamics of turbulence may be explained based on the theory of drift wave turbulence.

The strongest individual indicator for drift waves was the observed small cross-phase between density and potential fluctuations. Assuming adiabatic electrons, density and potential fluctuations associated to the drift wave are in phase. However, any dissipative effect in the parallel electron dynamics introduces a finite phase shift. In WEGA these are mainly collisional effects: electron-ion collisions in the highly ionised plasmas at high field and additional electron-neutral collisions in the weakly ionised plasmas at low field.

Fluctuations were found to be mainly driven by the density gradient. However, a trend to higher fluctuation amplitudes in the plasma centre was observed. This effect is likely related to the magnetic shear which is known to be able to stabilise drift waves. The practical effect of magnetic shear is that the strong parallel dynamics causes the perpendicular vortices to be twisted along with the field lines and to be finally nonlinearly torn apart to smaller scales [KS03]. The magnetic shear in WEGA decreases going toward the plasma centre, hence, higher fluctuations were found in the absence of stabilising shear.

The observed dependence of the poloidal structure size (reflected by d_θ) agreed satisfactorily with the predictions from drift wave theory as well as results from other experiments. A scaling of the poloidal correlation length with the inverse magnetic field strength, or poloidal wavenumbers with B , respectively, has been observed in tokamaks [RRB93] and stellarators [Ble98; Mah07]. This variation would fit well with theoretical predictions of drift wave turbulence models [WD83; TD85]. These models predict most power in poloidal wavenumber spectra to be located at large wavelengths compared to the drift scale ρ_s . Spectra of k_θ should be peaked at about $k_\theta \rho_s \approx 0.3$.

For the He discharges under consideration at low and high field, respectively, an average poloidal wavenumber of $\bar{k}_\theta \rho_s \approx 0.1$ was found. However, when changing the ion mass, \bar{k}_θ was found to remain constant, although ρ_s was changed by a factor of about 6. Hence, energy in the turbulent broad band spectrum was shifted to somewhat smaller scales compared to ρ_s , but still in a range according to the theoretical expectations ($\bar{k}_\theta \rho_s \lesssim 0.3$). The interpretation of the observed shift of power is difficult because turbulence dynamics is determined by a number of parameters which could not be kept constant in the wide parameter range covered by the m_i scan. However, further confirmation for the drift wave assumption was found, when more parameters were taken into account. The poloidal phase velocity was found to be mainly determined by the electron diamagnetic drift velocity. Both phase velocity and diamagnetic drift were found to decrease with increasing ion mass due to a change in the density gradient length. The dispersion relation of drift waves in the

observed range of perpendicular scales ($k_{\theta}\rho_s \ll 1$) is linear. Accordingly frequency spectra shifted towards lower frequencies with increasing ion mass.

The parallel dynamics of turbulence was also found to be consistent with the predictions from drift wave theory, at least for the high field case. A finite parallel wavenumber inheres in the drift wave mechanism due to the coupling between parallel and perpendicular dynamics. The parallel phase velocity of drift waves is expected to be mainly a projection of the poloidal phase velocity caused by the finite inclination of the wavefront with respect to the magnetic field vector, $v_{\parallel} \approx v_{\theta} \cdot \bar{k}_{\theta} / \bar{k}_{\parallel}$. The projected velocity component and the actual parallel phase velocity were calculated individually, yielding a difference which coincided satisfactorily with the ion sound velocity. The ion sound velocity in turn is the intrinsic parallel velocity of density perturbations associated to drift waves. A higher parallel phase velocity may be expected for smaller spatial scales ($k_{\theta}\rho_s > 0.3$), where the coupling of density fluctuations to Alfvén waves plays a role. The increase of v_{\parallel} at small scales has been studied at the TJ-K torsatron [Mah+07].

The absolute value of the average parallel wavelength, $\bar{\lambda}_{\parallel} = 2\pi / \bar{k}_{\parallel}$, in the high field case was in the order of the magnetic field line connection length, $\bar{\lambda}_{\parallel} \gtrsim R/\tau$, which can be treated as an upper limit. However, this limitation is strictly only valid if a self-interference of structures in the $r - \theta$ -plane would occur due to a lack of space in the poloidal direction. For the high field case this limitation turned out not to be a problem, since the observed structure fitted into the system.

A gap in the consistency of the drift wave picture results from the observed spatial asymmetry in the occurrence of fluctuation events. The asymmetry was associated with a predominant arising of fluctuations on the low field side of the torus, i.e. in the region of unfavourable magnetic curvature. This might be an indicator that curvature driven instabilities play a role in WEGA. Curvature driven modes are intrinsic two-dimensional phenomena ($k_{\parallel} = 0$), but the plasma dynamics parallel to the magnetic field may become important if regions of unfavourable and favourable curvature are connected by the magnetic field. The connection of favourable and unfavourable curvature regions is induced by the rotational transform. Hence, the observation of a finite parallel wavenumber is not necessarily a contradiction to turbulence dominated by curvature driven modes. But on the other hand, the small cross-phase between density and potential fluctuations is in contrast to curvature driven activity. A similar asymmetry has been observed at the TJ-K torsatron in form of higher fluctuation amplitudes and transport on the low field side, although the turbulence dynamics in TJ-K is dominated by drift waves [Mah07].

Parallel Dynamics in Conflict with Theoretical Limits

A different situation appeared in the low field case. The average parallel wavelength, formally derived from the cross-phase spectrum between two probes aligned along a field line, exceeded the field line connection length by far. Since the poloidal correlation length was in the order of the plasma dimensions, this would result in the self-interference of structures. But, the actual shape of the parallel cross-phase spectrum showed, that the average wavelength in this case is not a good measure

for the structure size. The spectrum yielded energy in the turbulent spectrum of k_{\parallel} to be distributed over a wide range of wavenumber components pointing parallel and antiparallel to the magnetic field vector. The resulting average wavenumber simply represents a kind of skewness in the parallel wavenumber spectrum, i.e. the centre of mass is shifted to one side. The observed spectrum might as well yield a vanishing average wavenumber in case of a slightly different shape. The observed parallel phase spectrum is in contrast to the poloidal phase spectrum, which was found to be consistent with the drift wave dispersion relation without a significant influence of the $\mathbf{E} \times \mathbf{B}$ drift.

The question of the loss of coherence in toroidal direction at rather low frequencies in the low field case remains unanswered.

Outlook

The results presented in this chapter provide a rounded overall picture characterising turbulence in the WEGA stellarator. A deep insight into the three-dimensional structure of turbulence was provided. The number of details presented on the parallel dynamics of turbulence encourages further studies delving into this topic. It could be shown, that WEGA as the experimental framework in combination with the diagnostic techniques used in this work provide the possibility to gain the required information in a high quality. Further studies should concentrate mainly on the observed spatial asymmetry in the occurrence of fluctuation events. This might be relevant for the distribution of turbulent transport on a fluxsurface and thus for comparisons of turbulent transport, which is typically measured locally, with global confinement in fusion devices. An experimental approach to gain deeper insight into the parallel dynamics of turbulence would be to increase the spatial resolution in toroidal direction. However, this is a technical challenge but it should be possible in a flexible machine like WEGA. More sampling points in toroidal direction are also a promising approach to explain the quick loss of coherence for higher frequencies in toroidal direction for the low field case.

Chapter 6

On Magnetic Islands and Turbulence

The flexibility of WEGA's magnetic topology offers the possibility to study new aspects of the broad field of plasma turbulence. One point which has been addressed in this work is the impact of symmetry breaking magnetic perturbations and thus magnetic islands on the dynamics of turbulence and on turbulent transport. The main purpose of this work was the general characterisation of turbulence in WEGA, which has been presented in all details in the past chapters. The study of turbulence in magnetic islands is a rather novel scientific field. Within this work only some initial experiments on this topic could be conducted, yielding encouraging results for further studies.

6.1 Motivation

The motivation to study turbulence in disturbed magnetic fields is based mainly on two aspects. First, it has been shown in other experiments that the presence of rational surfaces in the plasma is linked to phenomena like transport barriers and improved confinement [Cas+04]. But so far it has not been investigated to what extent these phenomena are affected by small error fields being resonant with the rational surfaces and leading to the formation of magnetic islands. A second point of interest affects the divertor operation of stellarators. In several devices magnetic islands are used to form the divertor field with open field lines ending at target plates. It is known that, due to the long connection length from the LCFS to the target plates in island divertors, parallel competes with perpendicular transport [Fen+06]. Therefore, it is necessary to understand transport in magnetic islands.

It is known, that in low shear stellarator experiments (i.e. the Wendelstein series [GRW85]) the energy confinement depends sensitively on the value of t . Optimum confinement was found in the vicinity of low order rational numbers ($t = 1/2, 1/3$), but not exactly at the rational numbers. Close to these fundamental resonances only high order Fourier components of the magnetic field perturbation may create small islands [Wob+87]. If a large number of rational surfaces is present in the t

profile, the effective plasma radius is decreased by the formation of islands.

The effect of rational surfaces being present in the τ profile has been studied in detail by Brakel et al. in the Wendelstein 7-AS stellarator [BWAT02]. Brakel et al. found that the observed reduced confinement in the presence of low order rational surfaces cannot be modelled by the assumption of islands being a radial short circuit for the plasma, with vanishing pressure gradient across islands. Transport at rational surfaces could be enhanced by e.g. turbulence or MHD instabilities.

The unique possibility to study the impact of field perturbations on turbulence in WEGA is given because it is known from flux surface measurements that $m = 1$ non-natural islands exist. The error producing these islands can - with some restrictions - be simulated in field line tracing calculations. It is also known that with additional error field compensation coils (EFCC) islands can be controlled both in size and position. The control of islands was limited to low field operation before this work. Saturation effects caused by the transformer yokes close to the EFCC introduced a strong nonlinearity in the control of the island width towards higher magnetic fields. In the frame of this work a new set of compensation coils was installed at WEGA which allows the reduction of the native island width by a factor of about 2 at $B = 500$ mT, corresponding to a reduction of the field error by a factor of about 4. The step to high field operation was necessary because magnetic effects are expected to be more pronounced in these plasmas.

6.2 Initial Experimental Results

In the following, some initial results on the effect of resonant magnetic field perturbations leading to the formation of islands are presented. The explanation is more phenomenological, comparing different plasma parameters for two extreme cases, referred to as without and with compensation. Both, results from stationary and fluctuation measurements are presented. The reference magnetic configuration is characterised by the $\iota = 1/5$ resonance being located just inside the LCFS. WEGA's intrinsic field perturbation leads to the formation of a static magnetic island chain at this resonance, as shown in fig. 6.2.1 (black) from flux surface measurements. The island width on the low field side was $w_{1/5} \approx 1$ cm. On the high field side w was much larger, up to about 3 cm. This is the case called "without compensation". Driving the EFCC at the maximum current of $I_{cc} = -500$ A, the island width could be reduced by a factor of about 2. This is the case called "with compensation" (red curve in fig. 6.2.1).

The reduction of $w_{1/5}$ on the low field side was in the order of the probe dimension. Hence, the observable effect caused by the pure reduction of w is expected to be small. More important is the estimated reduction of $\delta B_{1/5}$ by a factor of about 4 ($w_{mn} \propto \sqrt{\delta B_{mn}}$).

All results presented subsequently were obtained from discharges at high field using Neon as the discharge gas. Some of the experiments have also been undertaken using He as working gas. These results are not presented, because no effect larger than the error bars was found, which could be related to magnetic islands.

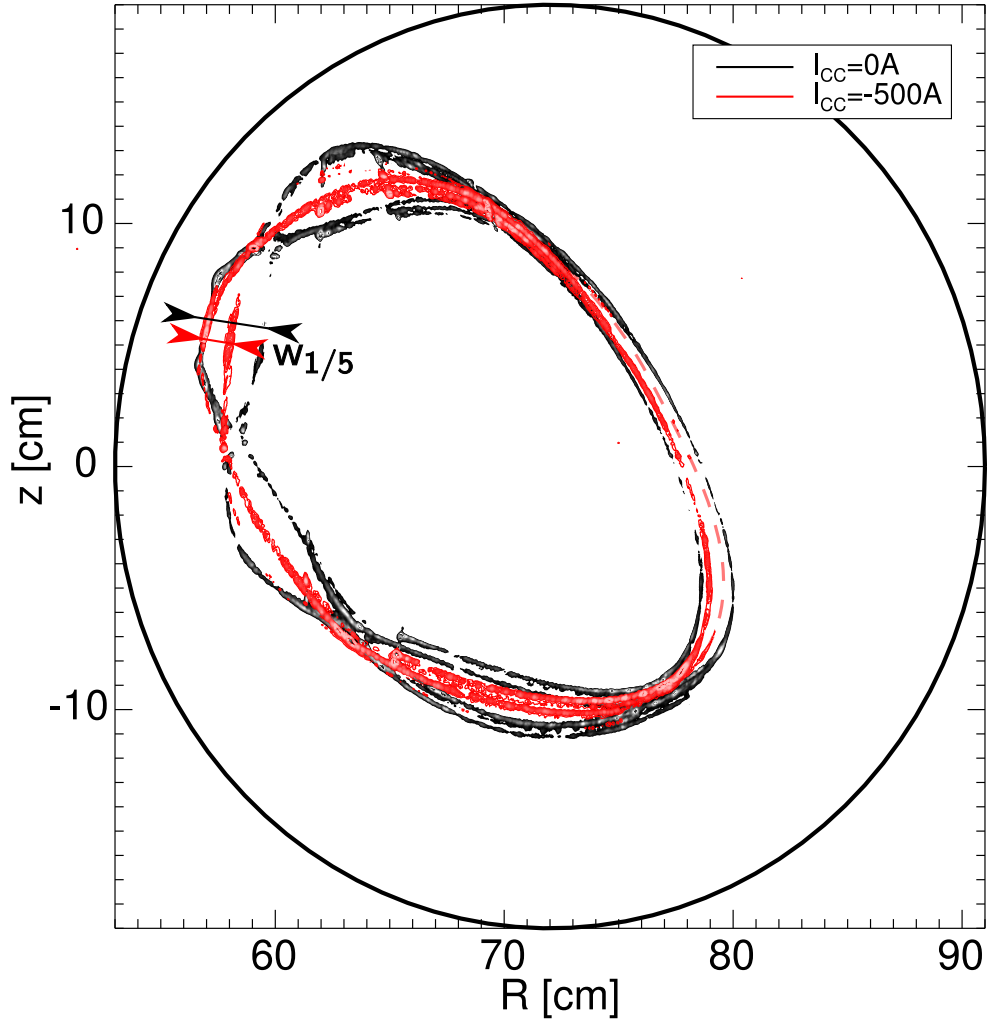


Figure 6.2.1: Flux surface measurement for the magnetic configuration in which the impact of magnetic islands was studied. The black curve is referred to as reference configuration without error field compensation. The observed island chain at $t = 1/5$ is located close to but completely inside the LCFS. The island width on the low field side is about 1 cm. The case of optimum compensation (EFCC current is maximum) is shown in red. The island chain is still present at the same radial position. Its poloidal phase is not affected by the EFCC, but the island width is reduced by a factor of about 2. The reduction is indicated by the arrows on the high field side.

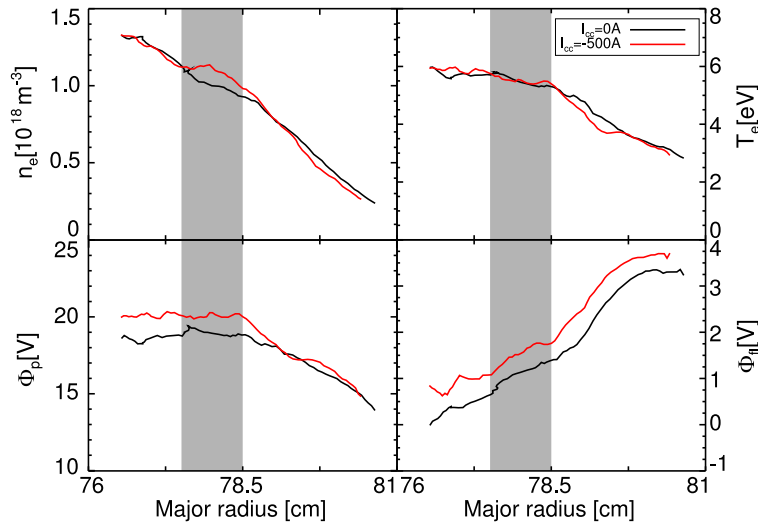


Figure 6.2.2: *Equilibrium profiles of plasmaparameters derived from swept Langmuir probe measurements in a Ne discharge at high field. The configurations without (black) and with (red) are compared. The grey shaded region marks the width of the $t = 1/5$ island without compensation.*

6.2.1 Profile Flattening Caused by Magnetic Islands.

The intuitive physical picture of what an island means for the plasma is a radial short circuit. Inner and outer boundaries of the island are connected by magnetic field lines. The pressure gradient should vanish at perturbed rational surfaces [Boo84]. A flattening of density profiles in islands has been observed at other experiments before [Ped+00; Tan+02]. A small, but reproducible effect of magnetic islands on equilibrium profiles was also observed in WEGA. In fig. 6.2.2 equilibrium profiles obtained from Langmuir probes for the two cases, namely without (black curves) and with (red curves) compensation are compared. The grey shaded region reflects the island width at $t = 1/5$ without compensation. The profiles represent an average over three equivalent discharges each. In the averaging process probe characteristics from individual discharges measured at the same radial position have been averaged before applying the fit function to obtain the plasma parameters. The results show that the gradients, which are important for the turbulence dynamics, are different for the two cases under consideration. In the density profiles, a slight flattening of the profile in the region of the island can be seen. With compensation the flattening is, just as the island width, reduced to a smaller radial region. No remarkable change can be seen in temperature profiles, where the profiles are flat in the edge region in any case, with or without compensation. Hence, no further change can be expected under these circumstances. More remarkable is the change in the plasma potential profile. Without compensation, the profile is rather smooth, lacking any abrupt changes in the gradient. This changes, however, when compensating the island. In

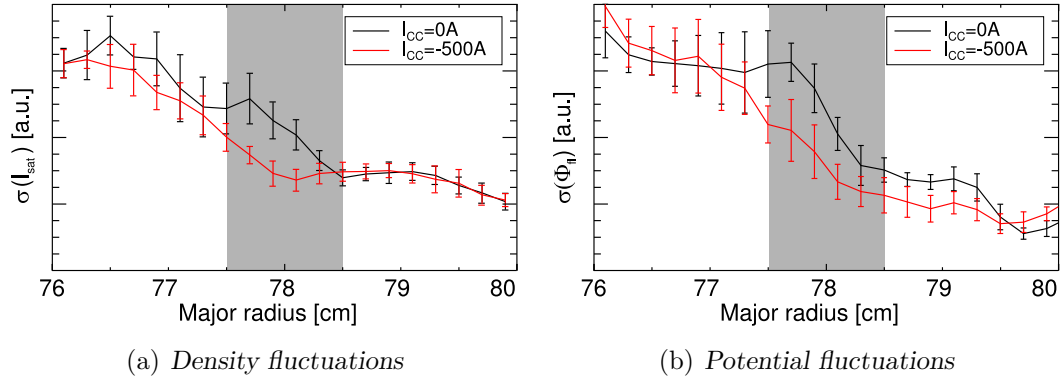


Figure 6.2.3: Comparison of the standard deviation (fluctuation amplitude) of \tilde{I}_{sat} (a) and $\tilde{\Phi}_f$ (b) without and with compensation. Both signals show a distinct local increase in the region of the $\iota = 1/5$ island, being smoothed with compensation.

this case the profile inside the LCFS is flat. At the LCFS, located at $R = 78.7$ cm, the profile shows a distinct shoulder with a steep gradient in the SOL. A similar behaviour, i.e. an alteration of the radial electric field due to island formation, has been observed at the TJ-II heliac, where it could be associated with the formation of transport barriers in the vicinity of magnetic islands [HPG02].

The reproducibility of the effects could be shown in individual discharge series. Further evidence for the flattening of the density profiles to be caused by magnetic islands could be given by slightly varying ι in order to shift the resonance position radially. The region of the flattening could be shifted together with the resonance.

6.2.2 Impact of Magnetic Islands on Turbulence

The described changes in the equilibrium profiles imply, that the turbulence characteristic might also be affected by the compensation of error fields, since turbulence dynamics is mainly controlled by the gradients in the background equilibrium. Therefore, several fluctuation parameters were measured and compared for the two cases under consideration.

Enhanced Fluctuation Amplitude

The most simple experiment for studying the effect of magnetic islands on turbulence is to compare the fluctuation amplitude σ with and without compensation. Fig. 6.2.3 shows radial profiles of σ for the ion saturation current (a) and the floating potential (b), hence the density and potential fluctuation amplitude. The black and red curves reflect equivalent discharges without and with compensation, respectively, averaged over five discharges each. The error bars represent the standard deviation within the discharge series.

The striking outcome from the comparison was a distinct local increase of the fluctuation amplitude without compensation, just inside the region of the island

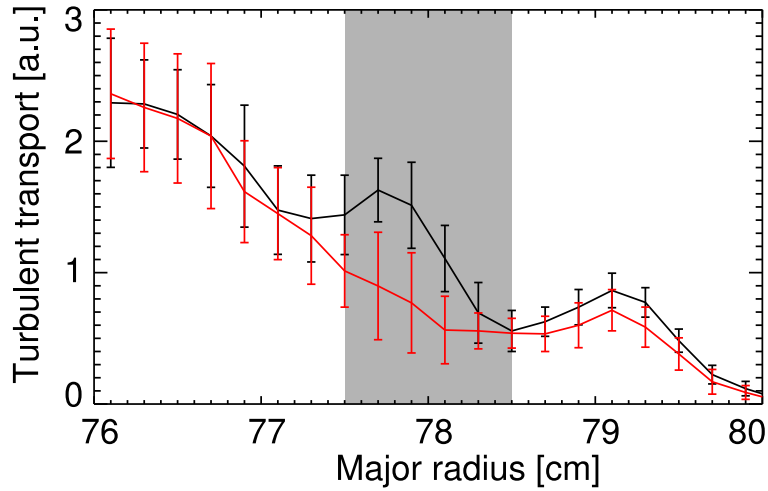


Figure 6.2.4: Profiles of the net turbulent radial $\mathbf{E} \times \mathbf{B}$ -flux for the two cases. The observed hump in the fluctuation amplitude leads to enhanced transport in the region of the $\iota = 1/5$ island. A second hump in the Γ profile is observed outside the LCFS close to the expected $\iota = 1/4$ resonance in the vacuum magnetic field configuration. This hump is unaffected by the EFCC.

(grey shaded). This local increase appeared as a hump in the profile. This hump appeared for both, density and potential fluctuations. When applying the EFCC the hump disappeared for both signals. Regarding the error bars it is important to note, that the effect was reproducible and did not vanish within the scatter of data from individual discharges. The centre of the hump was slightly shifted radially with respect to the experimentally obtained island position, but the shift was comparable to the probe dimensions reflecting only one source of error in the radial resolution.

Enhanced radial $\mathbf{E} \times \mathbf{B}$ Flux

The next parameter to be compared was the net turbulent radial particle flux. Fig. 6.2.4 shows the result of the analysis of data from the same discharges that were considered in the previous section. Without compensation again a hump in the profile can be seen in the region, where the $\iota = 1/5$ island is located. As expected, the error bars are larger, because the flux is a parameter derived from two signals (\tilde{I}_{sat} and $\tilde{\Phi}_{\text{fl}}$) being each subject to a statistical error. In contrast to the profiles of the density fluctuation amplitude, a second hump appears in the profile outside the LCFS at $R \approx 79.1$ cm. This is the position where, according to flux surface calculations, the $\iota = 1/4$ resonance is located in the vacuum magnetic field configuration. With compensation the hump inside the LCFS at $\iota = 1/5$ disappears, whereas the one at $\iota = 1/4$ is almost unaffected by the compensation. A possible explanation for this discrepancy is the Fourier spectrum of the EFCC, which is actually unknown. Flux surface measurements showing the effect of the EFCC concentrated on the one ι configuration, which is shown in fig. 6.2.1. Configurations

with $t = 1/4$ inside the LCFS have not been investigated. Therefore, it is possible, that the Fourier component $\delta B_{1,4}$ of the EFCC is much smaller than the $\delta B_{1,5}$ contribution.

The increased transport at $t = 1/5$ by a factor of about two (maximum of the hump) could be clearly related to the increase in the fluctuation amplitude. The cross-power and cross-phase spectrum between density and potential fluctuations contribute both to the particle flux as shown in section 2.2.2 ($\Gamma(\nu) \sim |\Psi_{n,\Phi}| \sin \alpha_{n,\Phi}$). An increase in the cross-power spectrum by a factor of about two without compensation was observed without affecting the shape of the spectrum. The turbulent broad band character of the fluctuations was conserved. A direct comparison of the cross-phase cannot be given here, because the error was too large to make a clear statement. The large error results from the artificial phase shift being introduced by the poloidal velocity v_θ of the structures. The radial position under consideration is close to the reversal point, where v_θ changes sign. Due to the small value of v_θ in the vicinity of the reversal point, its error may be larger than the average value.

Change of Perpendicular Dynamics

Poloidally resolved measurements were undertaken in order to study the perpendicular dynamics of turbulence in the region of islands. Radial profiles of fluctuation parameters derived from the poloidal-temporal correlation function were again compared for the cases without and with compensation. The poloidal correlation length was found to be unaffected by the compensation within the error of about 25% in d_θ . Clear effects were observed in the profiles of the poloidal velocity v_θ and the lifetime τ_L .

As shown in section 5.2.5 discharges in the high field operation regime of WEGA generally show a velocity shear layer in the region of the LCFS. This feature could be reproduced here for both cases, as shown in fig. 6.2.5 (a). But it can be clearly seen, that the position of the reversal point is changed when the EFCC is applied. Without compensation it was located at $R = 78.2$ cm in the equatorial plane. With compensation it was shifted inwards by 7 mm to $R = 77.5$ cm. The radial shift was comparable to the experimentally observed reduction in the island width. In both cases the position of the reversal point agreed satisfactorily with the outer separatrix of the island structure.

Besides the change in the velocity profiles, the lifetime of structures was also affected by the island formation as shown in fig. 6.2.6 (b). τ_L was significantly increased in the region of the island without compensation compared to the case with compensation. This result must be interpreted under the restrictions described in section 3.2. Since no information about the radial dynamics of structures was available for the considered cases, the increased lifetime might be an artefact. However, the result shows that the perpendicular dynamics of turbulence is somehow affected by the formation of island and needs to be studied in more detail.

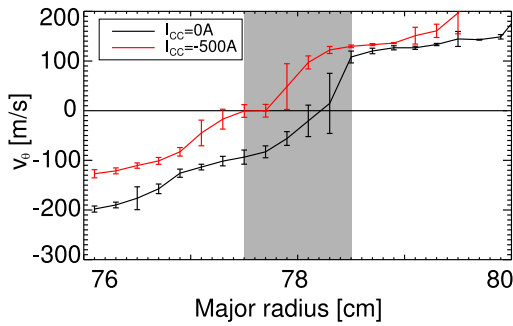


Figure 6.2.5: Poloidal velocity of turbulent structures. The velocity shear layer shifts radially when compensating the islands.

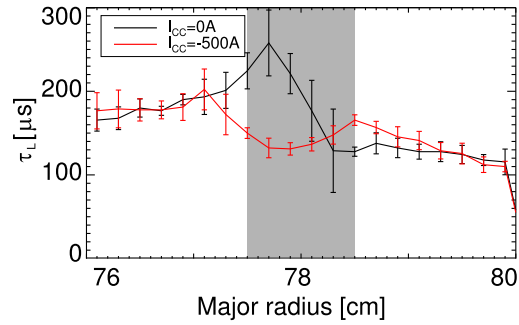


Figure 6.2.6: The lifetime obtained from poloidally resolved measurements changes significantly when manipulating the island width.

Radial Shift of Resonant Surface

The reference configuration showed locally increased turbulent transport in islands inside the LCFS as well as in the SOL. To what extent these observed humps are affected by mechanical limiters shall be clarified by shifting the islands radially. These experiments may also give further information on the linking between the island position and the reversal point of v_θ . The radial position of the resonance can be changed by small variations of the rotational transform. In a classical stellarator this can easily be done by varying the ratio between I_T and I_H . Since the toroidal field strength is specified by the ECRH frequency, the helical field was changed in order to shift the resonance. I_H was varied in steps of 2% with respect to the magnetic field configuration shown in fig. 6.2.1 (defined as reference configuration, $I_{H,ref}$). The results of these experiments are shown in fig. 6.2.7. Profiles of the turbulent particle flux are plotted for field configurations in the range from $I_H = (0.94 \dots 1.04) \cdot I_{H,ref}$. In all cases distinct humps in the profiles can be seen. As expected the humps shifted systematically in radial direction with varying rotational transform. Decreasing I_H , the hump associated to the $t = 1/5$ shifted radially outwards. The second hump at $t = 1/4$ disappears in this case, but it could be shifted radially inwards by increasing I_H with respect to the reference. Quantitatively there was a systematic discrepancy between the radial shift of the humps and the calculated position of the island, marked by the shaded regions in the plot. During the t -scan the predicted island position shifted stronger than the local transport maximum.

Transport profiles with compensation have not been measured for other than the reference configuration. However, the local maximum with respect to an assumed underlying smooth profile with compensation became more pronounced, when the island was partially or completely located in the limiter shadow. The LCFS is located at $R = 78.7$ cm.

An interesting result is the comparison of the transport maxima with the location of the reversal point of v_θ . The lowermost graph in fig. 6.2.7 shows the velocity

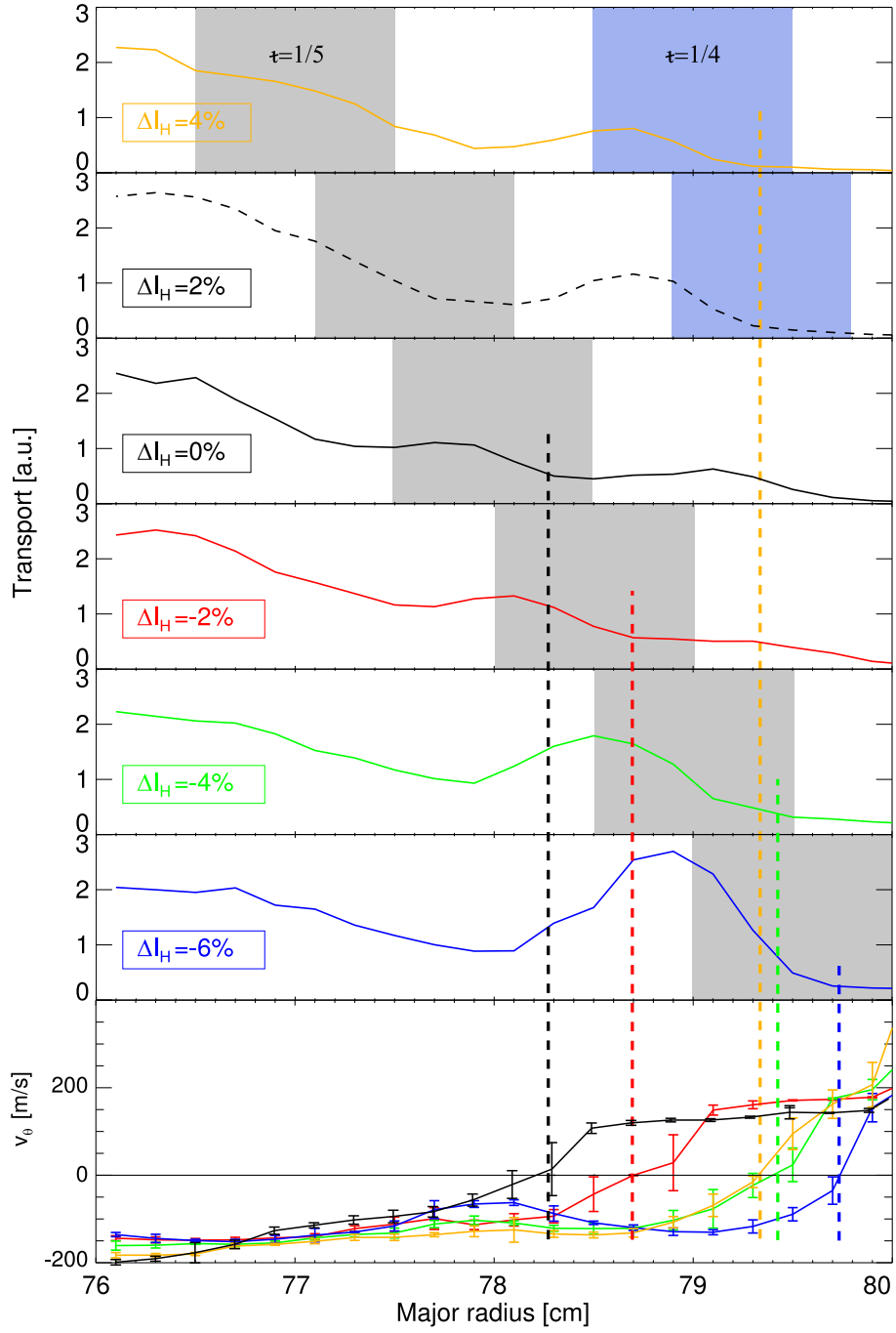


Figure 6.2.7: Profiles of Γ and v_θ for different τ configurations. The island position is shifted radially by small variations of the helical field coil current I_H . The grey shaded regions correspond to the predicted position of the $\tau = 1/5$ resonance, light blue corresponds to $\tau = 1/4$. ΔI_H is the variation with respect to the reference configuration shown previously. The dashed vertical lines mark the position of the velocity shear layer (change of sign in v_θ). It is mapped to the corresponding Γ -profile.

profiles corresponding to the individual transport profiles. In all cases the reversal point was located close to the outer boundary of the hump, as indicated by the dashed vertical lines in fig. 6.2.7. In the reference configuration, it was located just inside the LCFS as shown previously. Reducing t it was shifted outwards together with the $t = 1/5$ resonance into the region of open field lines. The reversal point 'left' the $t = 1/5$ resonance when it was shifted inwards by increasing t . As shown in fig. 6.2.7 for $\Delta I_H = +4\%$ it is located at the $t = 1/4$ resonance where the hump in the profile is consecutively very distinct, and which is closer to the LCFS than the $t = 1/5$ resonance.

6.3 Discussion

The interpretation of the results presented in this chapter is difficult because only some initial experiments could be undertaken within this work. The study of turbulence in the region of perturbed rational flux surfaces is a novel scientific field. The study is motivated by the observation in Wendelstein 7-AS, that rational surfaces have a strong impact on the confinement in low shear stellarators, which may not be simply explained by assuming magnetic islands to be radial short circuits reducing the effective plasma radius. Comparable studies of fluctuations in the vicinity and inside magnetic islands have been undertaken in the LHD heliotron, where an influence of islands on coherent MHD modes has been investigated [Wat+08]. At the TJ-II torsatron the role of rational surfaces on fluctuations and transport has been studied by comparing magnetic field configurations with and without low order rational surfaces being present in the region of closed flux surfaces. With islands a local change of $\mathbf{E} \times \mathbf{B}$ particle flux resulting from a change in the phase shift between density and potential fluctuations has been observed at TJ-II. Those changes in the flux are associated to a quasi-coherent mode related to the presence of rational surfaces [Ped+01; Ped+04]. Enhanced pressure driven fluctuations in the region of magnetic islands have been observed in the H-1NF heliac [HPB03].

However, the experiments in WEGA are the first ones comparing electrostatic turbulence for magnetic configurations differing only in the amplitude of magnetic field perturbations being resonant with low order rational flux surfaces.

The observed flattening of the density profiles together with an enhanced fluctuation amplitude gives rise to a typical 'chicken and egg' discussion if the knowledge obtained from the first part of this work is taken into account. On the one hand turbulence has been found to be driven by the density gradient in WEGA. In the intuitive picture of the island as a radial short circuit, this implies, that the fluctuation amplitude should be reduced in the island because the density gradient vanishes or is at least reduced. On the other hand, the flattening might be caused by the enhanced radial particle flux in the island, if perpendicular competes with parallel transport. The question arising from both scenarios is what drives turbulence in the region of magnetic islands. Obviously other driving mechanisms but the density gradient must be involved here. Turbulence in general develops as a balance between source and sink terms driving and damping turbulence, respectively.

A theoretical approach to this problem has been given by Reiser and Scott [RS05]. Simulations of fluid-drift-turbulence in perturbed magnetic fields also have shown an increase of density fluctuations and $\mathbf{E} \times \mathbf{B}$ flux. The results of these simulation and their comparability with experimental results from WEGA need to be discussed in detail. The simulations have been performed for perturbed magnetic fields in the dynamic ergodic divertor (DED) region of the TEXTOR tokamak, hence the edge of a hot fusion plasma. The introduction of a perturbing magnetic field in the simulations have led to additional source terms in the energy balance giving free energy to drive turbulence. The simulation results have shown that collisionality plays an important role for turbulence in disturbed fields. Reiser and Scott characterised

collisionality by the so called ballooning parameter given by:

$$\nu_b = \frac{m_e R \nu_{ee}}{m_i c_s t^2}, \quad (6.1)$$

where ν_{ee} is the electron-electron collision frequency. The additional driving term becomes important for $\nu_b \ll 1$, hence for low collisionality. The background plasma parameters for the simulations were of course different to the experimental conditions in WEGA. The following table compares the relevant parameters and ν_b for simulations and for the experiments undertaken in WEGA.

	R [cm]	n_e [m ⁻³]	T_e [eV]	m_i [amu]	B [T]	t	L_n [cm]	ν_B
TEXTOR, high coll.	175	$6.5 \cdot 10^{19}$	30.8	2	2	1/3	3	1.48
TEXTOR, low coll.	175	$2 \cdot 10^{19}$	100	2	2	1/3	3	0.04
WEGA, Ne	72	$1 \cdot 10^{18}$	5	20	0.5	1/5	3	0.18
WEGA, He	72	$1 \cdot 10^{18}$	5	4	0.5	1/5	3	0.5

This comparison shows what has already been mentioned in sec. 2.5. Dimensionless parameters of WEGA are comparable to the edge plasma of fusion devices. ν_b for experimental conditions in WEGA is comparable to the case of low collisionality in TEXTOR-DED. From this point of view it is reasonable to find increased transport in perturbed magnetic fields in WEGA plasmas. It is also reasonable that such an effect was not observed for He plasmas because ν_b was larger here.

However, a direct comparison of the presented simulation results with WEGA experiments must be handled with care. The additional source term arising in the simulations is of an electromagnetic nature, meaning that it goes together with parallel currents linked to Alfvén waves. This is in contrast to the results from chapter 5 where no electromagnetic activity could be found.

Experimental results on turbulence in islands presented in this work must be seen as an initial step into a new research field. What could be shown is that it is worth to follow this path because some interesting effects have been observed. The observations coincide with simulation results for experimental conditions which are in terms of dimensionless parameters comparable to the experimental conditions in WEGA.

6.4 Outlook

As outlined previously the results on turbulence and magnetic islands can only be seen as an initial step. A brief proposal for a scientific program on this topic following this work will now be given.

The additional driving term given in the TEXTOR-DED simulation is related to fluctuating parallel currents and thus also to magnetic field fluctuations. Measurement of turbulent magnetic fluctuations is a challenge because the signals are typically very small. But it is possible and has successfully been done by other experiments [Sto+99; Rah07]. A common technique is to use tiny pick up coils being sensitive to $\partial B/\partial t$. A first attempt to measure magnetic fluctuations at WEGA with Hall sensors showed that these are not sensitive enough by a long way [Mar02]. Relative fluctuation amplitudes will probably be much less than $\tilde{B}/B \ll 10^{-3}$. An increase of \tilde{B} without compensation would be a fingerprint of increased Alfvénic activity in the island and therefore of electromagnetic effects playing a role. Another point of great interest is to obtain structural information about turbulence in disturbed magnetic fields. As shown in this work it is possible to gain information about the spatial and temporal structure of turbulence from statistical analysis techniques applied to data from multiple Langmuir probes. An open question is how turbulent structure propagate along or across magnetic islands. For unperturbed closed flux surfaces it could be shown that structures propagate along flux surfaces, without a significant radial velocity component in WEGA. In case of perturbed fields it is possible that the increased radial transport is related to a radial velocity component of structures across the island. Using two-dimensional probe arrays it is possible to reconstruct turbulent structures locally in the poloidal plane [MHS02; Ram+05; Gru+07] comparable to the technique used in this work with toroidally separated probes. Unfortunately, the island width on the low field side of WEGA, where easy experimental access is given, is very small. Increasing the island width by amplification of the native error fields does not show very much profit in this region. More information could be gained from measurements on the high field side where the radial width of the islands is much larger. A first draft for a possible more sophisticated probe setup for this region is shown in figure 6.4.1. The technical challenge is that the only ports on WEGA, which are big enough to allow access to the plasma with a large probe array are located on the low field side. So a design has to be found where the array can be retracted from the plasma without drawing it back into a port as done with the poloidal array used so far. This could be done using a remotely controlled tilting mechanism comparable to the mechanism that has been installed for the reference probe. WEGA's unique feature of having access to islands with Langmuir probes providing a surpassing high spatial resolution allows to study more than turbulent particle flux, but also turbulent energy transport. A very sophisticated technological solution to measure energy transport by means of fast swept Langmuir probes [SET07] is installed at WEGA and has been initially tested. The equipment has to be fine tuned to deal with the smaller signals compared to Wendelstein 7-AS where it has been used before.

Further experiments on turbulence in perturbed magnetic fields should be accompanied by simulations for conditions which are more realistic for WEGA. The DALF3 turbulence code used in [RS05] has been successfully implemented for the TJ-K torsatron which is in size, magnetic field and parameter range comparable to WEGA. Thus the applicability of the code for WEGA is given.

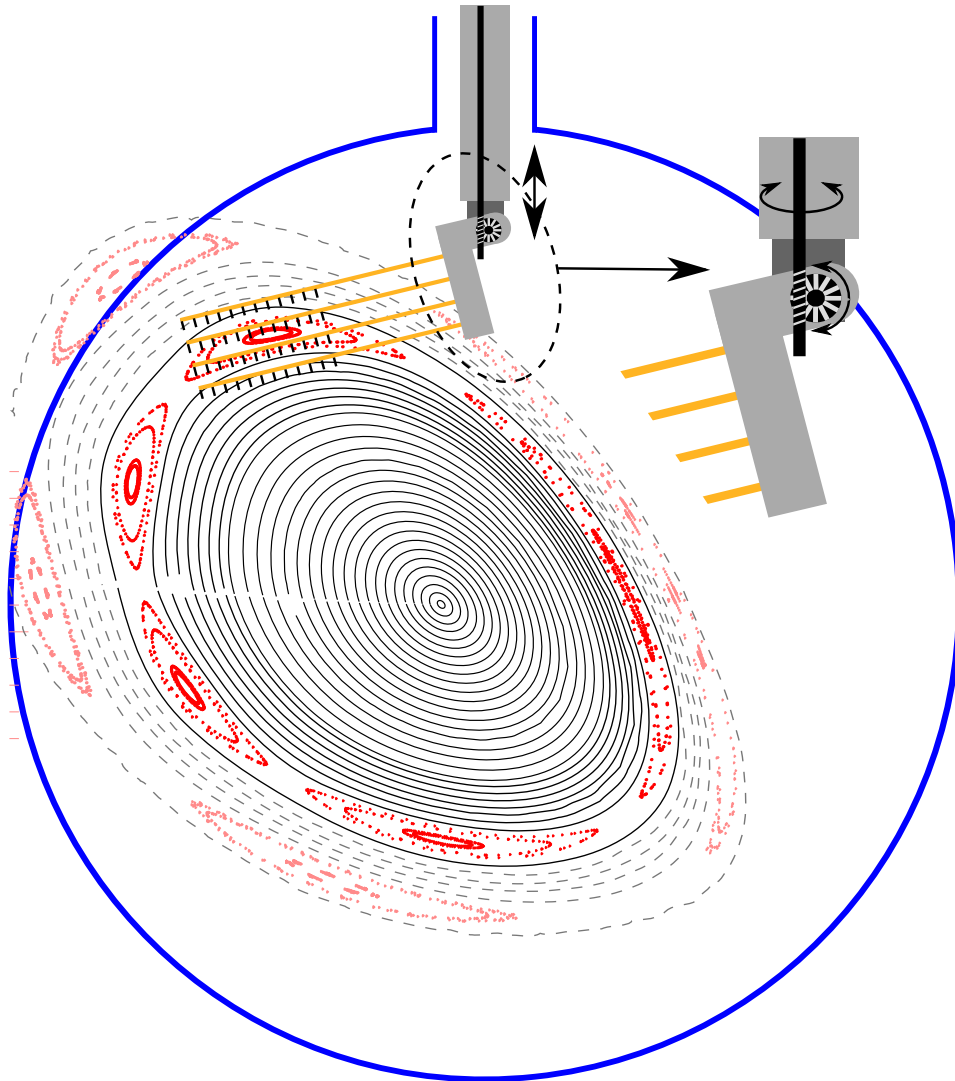


Figure 6.4.1: Sketch of a two-dimensional probe array providing access to the large islands on the high field side of WEGA. The tilting mechanism is necessary to reach the regions of interest and to retract the massive object from the plasma when it is not in use.

Bibliography

- [ABR57] J E Allen, R L F Boyd, and P Reynolds. “The Collection of Positive Ions by a Probe Immersed in a Plasma”. In: *Proceedings of the Physical Society. Section B* 70.3 (1957). Pp. 297–304. DOI: 10.1088/0370-1301/70/3/303.
- [Ant04] Ghassan Y. Antar. “Universality of Intermittent Convective Transport in the Scrape-off Layer of Magnetically Confined Devices”. In: *Contributions to Plasma Physics* 44.1-3 (2004). Pp. 217–221. DOI: 10.1002/ctpp.200410031.
- [BKP82] J. M. Beall, Y. C. Kim, and E. J. Powers. “Estimation of wavenumber and frequency spectra using fixed probe pairs”. In: *Journal of Applied Physics* 53.6 (1982). Pp. 3933–3940. DOI: 10.1063/1.331279.
- [BWR98] R. D. Bengtson, D. L. Winslow, and D. W. Ross. “Fluctuation Measurements with two Separated Probe Arrays on the Same Flux Tube”. In: *Contributions to Plasma Physics* 38.special issue (1998). Pp. 104–109.
- [Ber58] Ira B. Bernstein. “Waves in a Plasma in a Magnetic Field”. In: *Physical Review Letters* 109.1 (Jan. 1958). Pp. 10–21. DOI: 10.1103/PhysRev.109.10.
- [BR59] Ira B. Bernstein and Irving N. Rabinowitz. “Theory of Electrostatic Probes in a Low-Density Plasma”. In: *Physics of Fluids* 2.2 (1959). Pp. 112–121. DOI: 10.1063/1.1705900.
- [Bet39] H. A. Bethe. “Energy Production in Stars”. In: *Physical Review* 55.5 (Mar. 1939). Pp. 434–456. DOI: 10.1103/PhysRev.55.434.
- [Bic97] R J Bickerton. “Magnetic turbulence and the transport of energy and particles in tokamaks”. In: *Plasma Physics and Controlled Fusion* 39.3 (1997). Pp. 339–365. DOI: 10.1088/0741-3335/39/3/002.
- [Ble98] Johannes Bleuel. “Elektrostatische Turbulenz am Plasmarand des Stellarators Wendelstein 7-AS”. IPP Report III/235. PhD thesis. Max Planck Institut für Plasmaphysik, Garching: Technische Universität München, 1998.

- [Boe+03] J. A. Boedo et al. “Transport by intermittency in the boundary of the DIII-D tokamak”. In: *Physics of Plasmas* 10.5 (2003). Pp. 1670–1677. DOI: 10.1063/1.1563259.
- [Boh49a] D. Bohm. “Minimum Ionic Kinetic Energy for a Stable Sheath”. In: *The Characteristics of Electrical Discharges in Magnetic Fields*. Ed. by A. Guthrie and R. K. Wakerling. McGraw-Hill Book Company, inc., 1949. Chap. 3, pp. 77–86.
- [Boh49b] D. Bohm. “Qualitative Description of the Arc Plasma in a Magnetic Field”. In: *The Characteristics of Electrical Discharges in Magnetic Fields*. Ed. by A. Guthrie and R. K. Wakerling. McGraw-Hill Book Company, inc., 1949. Chap. 1, pp. 1–12.
- [Boo84] Allen H. Boozer. “Magnetic island growth”. In: *Physics of Fluids* 27.8 (1984). Pp. 2055–2062. DOI: 10.1063/1.864863.
- [Boo98] Allen H. Boozer. “What is a stellarator?”. In: *Physics of Plasmas* 5.5 (1998). Pp. 1647–1655. DOI: 10.1063/1.872833.
- [BWAT02] R. Brakel and the W7-AS Team. “Electron energy transport in the presence of rational surfaces in the Wendelstein 7-AS stellarator”. In: *Nuclear Fusion* 42.7 (2002). Pp. 903–912. DOI: 10.1088/0029-5515/42/7/313.
- [Bra+97] R. Brakel et al. “Confinement in W7-AS and the role of radial electric field and magnetic shear”. In: *Plasma Physics and Controlled Fusion* 39.12B (1997). B273–B286. DOI: 10.1088/0741-3335/39/12B/021.
- [Bri88] Oran E. Brigham. *The fast Fourier transform and its applications*. Prentice Hall Signal Processing Series. New Jersey: Prentice Hall, 1988.
- [Bur06] Andreas Burkert. “The turbulent interstellar medium”. In: *Comptes Rendus Physique* 7.3-4 (2006). Pp. 433–441.
- [CA05] Carreras and Benjamin A. “Plasma edge cross-field transport: experiment and theory”. In: *Journal of Nuclear Materials* 337-339 (Mar. 2005). Pp. 315–321. DOI: 10.1016/j.jnucmat.2004.10.034.
- [Car+96] B. A. Carreras et al. “Fluctuation-induced flux at the plasma edge in toroidal devices”. In: *Physics of Plasmas* 3.7 (1996). Pp. 2664–2672. DOI: 10.1063/1.871523.
- [Cas+04] F. Castejón et al. “Influence of low-order rational magnetic surfaces on heat transport in TJ-II heliac ECRH plasmas”. In: *Nuclear Fusion* 44.5 (2004). Pp. 593–599. DOI: 10.1088/0029-5515/44/5/003.
- [Cat+85] G. Cattanei et al. “Plasma confinement and the effect of rotational transform in the Wendelstein VII-A stellarator”. In: *Plasma Physics and Controlled Nuclear Fusion Research*. Vol. 2. Proc. 10th Int. Conf. London, 1984. IAEA. Vienna 1985. P. 371.

- [Che65a] F.F. Chen. “Electric Probes”. In: *Plasma Diagnostic Techniques*. Ed. by R.H. Huddleston. Academic Press, New York, 1965. Chap. 4, pp. 113–200.
- [Che84] F.F. Chen. *Introduction to Plasma Physics and controlled Fusion*. Plenum Press, 1984.
- [Che01] Francis F. Chen. “Langmuir probe analysis for high density plasmas”. In: *Physics of Plasmas* 8.6 (2001). Pp. 3029–3041. DOI: 10.1063/1.1368874.
- [Che65b] Francis F. Chen. “Numerical computations for ion probe characteristics in a collisionless plasma”. In: *Journal of Nuclear Energy. Part C, Plasma Physics, Accelerators, Thermonuclear Research* 7.1 (1965). Pp. 47–67. DOI: 10.1088/0368-3281/7/1/306.
- [Coo61] T. Coor. “Plasma diffusion in stellarators”. In: *Journal of Nuclear Energy. Part C, Plasma Physics, Accelerators, Thermonuclear Research* 2.1 (1961). Pp. 81–83. DOI: 10.1088/0368-3281/2/1/311.
- [Cor61] S. Corrsin. “Turbulent flow”. In: *American Scientist* 49.3 (1961). Pp. 300–325.
- [DRR02] V. I. Demidov, S. V. Ratynskaia, and K. Rypdal. “Electric probes for plasmas: The link between theory and instrument”. In: *Review of Scientific Instruments* 73.10 (2002). Pp. 3409–3439. DOI: 10.1063/1.1505099.
- [EMMM80] R. F. Ellis, E. Marden-Marshall, and R. Majeski. “Collisional drift instability of a weakly ionized argon plasma”. In: *Plasma Physics* 22.2 (1980). Pp. 113–131. DOI: 10.1088/0032-1028/22/2/002.
- [End99] M. Endler. “Turbulent SOL transport in stellarators and tokamaks”. In: *Journal of Nuclear Materials* 266-269 (Mar. 1999). Pp. 84–90. DOI: 10.1016/S0022-3115(98)00659-X.
- [End94] Michael Endler. “Experimentelle Untersuchung und Modellierung elektrostatischer Fluktuationen in den Abschälsschichten des Tokamak ASDEX und des Stellarators Wendelstein 7-AS”. IPP Report III/197. PhD thesis. Max Planck Institut für Plasmaphysik, Garching: Technische Universität München, 1994.
- [FS06] G. Falkovich and K. R. Sreenivasan. “Lessons from Hydrodynamic Turbulence”. In: *Physics Today* 59.4 (2006). P. 43.
- [Fen+06] Y. Feng et al. “Physics of Island Divertor Plasmas in Stellarators”. In: *Contributions to Plasma Physics* 46.7-9 (2006). Pp. 504–514. DOI: 10.1002/ctpp.200610037.
- [Fen+00] C. Fenzi et al. “Interplay between edge and outer core fluctuations in the tokamak Tore Supra”. In: *Nuclear Fusion* 40.9 (2000). Pp. 1621–1626. DOI: 10.1088/0029-5515/40/9/306.

- [Fik+96] G Fiksel et al. “Measurement of magnetic fluctuation-induced heat transport in tokamaks and RFP”. In: *Plasma Physics and Controlled Fusion* 38.12A (1996). A213–A225. DOI: 10.1088/0741-3335/38/12A/016.
- [Fil+95] A. V. Filippas et al. “Conditional analysis of floating potential fluctuations at the edge of the Texas Experimental Tokamak Upgrade (TEXT-U)”. In: *Physics of Plasmas* 2.3 (1995). Pp. 839–845. DOI: 10.1063/1.871435.
- [Fis78] Nathaniel J. Fisch. “Confining a Tokamak Plasma with rf-Driven Currents”. In: *Physical Review Letters* 41.13 (Sept. 1978). Pp. 873–876. DOI: 10.1103/PhysRevLett.41.873.
- [Fri95] U. Frisch. *Turbulence: The Legacy of A. N. Kolmogorov*. Cambridge University Press, 1995.
- [GS79] A..A.. Galeev and R.Z. Sagdeev. “Theory of Neoclassical Diffusion”. In: *Reviews of Plasma Physics*. Ed. by M. A.. Leontovich. Vol. 7. Translated from Russian by Herbert Lashinsky. Consultants Bureau, New York, 1979. Pp. 257–+.
- [Gia+94] L. Giannone et al. “Density, temperature, and potential fluctuation measurements by the swept Langmuir probe technique in Wendelstein 7-AS”. In: *Physics of Plasmas* 1.11 (1994). Pp. 3614–3621. DOI: 10.1063/1.870917.
- [Gra+99] E. Gravier et al. “Control of the chaotic regimes of nonlinear drift-waves in a magnetized laboratory plasma”. In: *Physics of Plasmas* 6.5 (1999). Pp. 1670–1673. DOI: 10.1063/1.873423.
- [GRW85] G. Grieger, H. Renner, and H. Wobig. “Wendelstein Stellarators”. In: *Nuclear Fusion* 25.9 (1985). Pp. 1231–1242.
- [Gri+71] G. Grieger et al. “Particle-confinement minima in the Wendelstein II-a-Stellarator”. In: *Plasma Physics and Controlled Nuclear Fusion Research*. Vol. 3. Proc. 4th Int. Conf. Madison, 1971. IAEA. Vienna 1971. P. 37.
- [Gro95] S. Großmann. “Wie entsteht eigentlich Turbulenz”. In: *Physikalische Blätter* 51.7/8 (1995). Pp. 641–646.
- [Gru+07] O Grulke et al. “Laboratory studies of drift waves: nonlinear mode interaction and structure formation in turbulence”. In: *Plasma Physics and Controlled Fusion* 49.12B (2007). B247–B257. DOI: 10.1088/0741-3335/49/12B/S23.
- [Gru01] Olaf Grulke. “Investigation of large-scale spatiotemporal fluctuation structures in magnetized plasmas”. PhD thesis. Christian-Albrechts-Universität zu Kiel, 2001.
- [HPB03] J. H. Harris, D. G. Pretty, and B.D. Blackwell. “Resonances and fluctuations in H-1NF”. In: *International Stellarator Workshop*. 2003.

- [HM78] Akira Hasegawa and Kunioki Mima. “Pseudo-three-dimensional turbulence in magnetized nonuniform plasma”. In: *Physics of Fluids* 21.1 (1978). Pp. 87–92. DOI: 10.1063/1.862083.
- [HM77] Akira Hasegawa and Kunioki Mima. “Stationary Spectrum of Strong Turbulence in Magnetized Nonuniform Plasma”. In: *Physical Review Letters* 39.4 (July 1977). Pp. 205–208. DOI: 10.1103/PhysRevLett.39.205.
- [HM92] Richard D. Hazeltine and James D. Meiss. *Plasma Confinement*. Vol. 86. Frontiers in Physics. Redwood City, CA: Addison-Wesley, 1992.
- [Her89] N. Hershkowitz. “How Langmuir Probes Work”. In: *Plasma Diagnostics*. Ed. by O Auciello and D.L. Flamm. Vol. 1. Discharge parameters and chemistry. Academic Press, San Diego, 1989. Chap. 3, pp. 113–183.
- [Hid95] C Hidalgo. “Edge turbulence and anomalous transport in fusion plasmas”. In: *Plasma Physics and Controlled Fusion* 37.11A (1995). A53–A67. DOI: 10.1088/0741-3335/37/11A/004.
- [HPG02] C Hidalgo, M A Pedrosa, and B Gonçalves. “Fluctuations, sheared radial electric fields and transport interplay in fusion plasmas”. In: *New Journal of Physics* 4 (2002). P. 51. DOI: 10.1088/1367-2630/4/1/351.
- [HH76] F. L. Hinton and R. D. Hazeltine. “Theory of plasma transport in toroidal confinement systems”. In: *Review of Modern Physics* 48.2 (Apr. 1976). Pp. 239–308. DOI: 10.1103/RevModPhys.48.239.
- [Hor99] W. Horton. “Drift waves and transport”. In: *Review of Modern Physics* 71.3 (Apr. 1999). Pp. 735–778. DOI: 10.1103/RevModPhys.71.735.
- [Hor+04] K. Horvath et al. “Langmuir Probe Measurements in the WEGA Stellarator”. In: *Contributions to Plasma Physics* 44.7-8 (2004). Pp. 650–655. DOI: 10.1002/ctpp.200410096.
- [Hor05] Kinga Horvath. “Characterisation and Optimization of WEGA Plasmas”. PhD thesis. Ernst-Moritz-Arndt-Universität Greifswald, 2005.
- [Hor+06] Kinga Horvath et al. “Investigations of the electron temperature profiles at the WEGA stellarator”. In: *Plasma Physics and Controlled Fusion* 48.2 (2006). Pp. 315–323. DOI: 10.1088/0741-3335/48/2/009.
- [Hul+91] T. Huld et al. “Coherent structures in two-dimensional plasma turbulence”. In: *Physics of Fluids B: Plasma Physics* 3.7 (1991). Pp. 1609–1625. DOI: 10.1063/1.859680.
- [IPC07] IPCC. *Climate Change 2007: The Physical Science Basis. Contribution of Working Group I to the Fourth Assessment Report of the Intergovernmental Panel on Climate Change*. Ed. by S. Solomon et al. Cambridge University Press, 2007.

- [Jen98] Frank Jenko. “Numerische Modellierung von stoßfreier Driftwellenturbulenz”. IPP report 5/82, November 1998, Max-Planck-Institut für Plasmaphysik, Garching bei München. PhD thesis. Technische Universität München, 1998.
- [Jha+92] R. Jha et al. “Intermittency in tokamak edge turbulence”. In: *Physical Review Letters* 69.9 (Aug. 1992). Pp. 1375–1378. DOI: 10.1103/PhysRevLett.69.1375.
- [KHP99] Keilhacker, M., Hawryluk, R. J., and Pease, R. S. “JET Deuterium–Tritium Results and Their Implications [and Discussion]”. In: *Philosophical Transactions: Mathematical, Physical and Engineering Sciences* 357.1752 (Mar. 1999). Pp. 415–442. ISSN: 1364-503X.
- [KS03] A. Kendl and B. D. Scott. “Magnetic Shear Damping of Dissipative Drift Wave Turbulence”. In: *Physical Review Letters* 90.3 (Jan. 2003). P. 035006. DOI: 10.1103/PhysRevLett.90.035006.
- [Ker62] D W Kerst. “The influence of errors on plasma-confining magnetic fields”. In: *Journal of Nuclear Energy. Part C, Plasma Physics, Accelerators, Thermonuclear Research* 4.4 (1962). Pp. 253–262. DOI: 10.1088/0368-3281/4/4/303.
- [Kir+05] G.S. Kirnev et al. “Comparison of plasma turbulence in the low- and high-field Scrape-Off Layers in the T-10 tokamak”. In: *Nuclear Fusion* 45.6 (2005). Pp. 459–467. DOI: 10.1088/0029-5515/45/6/007.
- [KA05] J. Kißlinger and T. Andreeva. “Correction possibilities of magnetic field errors in WENDELSTEIN 7-X”. In: *Fusion Engineering and Design* 74.1-4 (Nov. 2005). Pp. 623–626. DOI: 10.1016/j.fusengdes.2005.06.124.
- [Kli+97] T Klinger et al. “Chaos and turbulence studies in low- β plasmas”. In: *Plasma Physics and Controlled Fusion* 39.12B (1997). B145–B156. DOI: 10.1088/0741-3335/39/12B/012.
- [Kol91] A. N. Kolmogorov. “Dissipation of Energy in the Locally Isotropic Turbulence”. In: *Proceedings: Mathematical and Physical Sciences* 434.1890 (July 1991). First published in Russian in: Dokl. Akad. Nauk. SSSR (1941), 32(1). Pp. 15–17. ISSN: 0962-8444.
- [KSH78] A. Komori, N. Sato, and Y. Hatta. “Excitation and Control of the Rayleigh-Taylor Instability in a Plasma with a Curved Magnetic Field”. In: *Physical Review Letters* 40.12 (Mar. 1978). Pp. 768–771. DOI: 10.1103/PhysRevLett.40.768.
- [LL87] B. LaBombard and B. Lipschultz. “Poloidal asymmetries in the scrape-off layer plasma of the Alcator C tokamak”. In: *Nuclear Fusion* 27 (1987). Pp. 81–99.

-
- [Laf66] James G. Laframboise. *Theory of spherical and cylindrical Langmuir probes in a collisionless, Maxwellian plasma at rest*. Tech. rep. Institute for Aerospace Studies, University of Toronto, 1966.
- [Lan23] I. Langmuir. “Positive Ion Currents from the Positive Column of Mercury Arcs”. In: *Science* 58 (Oct. 1923). Pp. 290–291.
- [LMS24] I. Langmuir and H. Mott-Smith. “Studies of Electric Discharges in Gases at Low Pressures”. In: *General Electric Review* 27 (1924). Pp. 449, 538, 616, 762, 810.
- [Laq+07] H.P. Laqua et al. “Electron Cyclotron Wave Experiments at the WEGA Stellarator”. In: *34. EPS Conference on Plasma Phys. Warsaw*. Vol. 31F. 2007. P–1.154. URL: http://epsppd.epfl.ch/Warsaw/pdf/P2_145.pdf.
- [Law55] J. D. Lawson. *Some Criteria for a Useful Thermonuclear Reactor*. Tech. rep. GP/R 1807. Declassified April 1957. Harwell: Atomic Energy Research Establishment, 1955.
- [Lie85] Paulett C. Liewer. “Measurements of microturbulence in Tokamaks and comparisons with theories of turbulence and anomalous transport”. In: *Nuclear Fusion* 25.5 (1985). Pp. 543–621.
- [Mah+07] N. Mahdizadeh et al. “Investigation of the parallel dynamics of drift-wave turbulence in toroidal plasmas”. In: *Plasma Physics and Controlled Fusion* 49 (July 2007). Pp. 1005–1017. DOI: 10.1088/0741-3335/49/7/005.
- [Mah07] Navid Mahdizadeh. “Investigation of Three-dimensional Turbulent Structure in the Torsatron TJ-K”. PhD thesis. Universität Stuttgart, 2007.
- [Mar02] Stefan Marsen. “Entwicklung und Erprobung einer Hallsonde zur Untersuchung des Magnetfeldes im Stellarator WEGA”. Diplomarbeit. Fachhochschule Stralsund, 2002.
- [MHS02] E Martines, M Hron, and J Stöckel. “Coherent structures in the edge turbulence of the CASTOR tokamak”. In: *Plasma Physics and Controlled Fusion* 44.3 (2002). Pp. 351–359. DOI: 10.1088/0741-3335/44/3/305.
- [McC82] J.H. McClellan. “Multidimensional spectral estimation”. In: *Proceedings of the IEEE*. Vol. 70. 9. 1982. Pp. 1029–1039.
- [MY71] A.S. Monin and A. M. Yaglom. *Statistical Fluid Mechanics*. Vol. 1. Cambridge, MA: M.I.T. Press, 1971.
- [MS66] A. I. Morozov and L.S. Solov’ev. “The structure of magnetic fields”. In: *Reviews of plasma physics*. Ed. by M. A. Leontovich. Vol. 2. 1966. P. 1.

- [MSL26] H. M. Mott-Smith and Irving Langmuir. “The Theory of Collectors in Gaseous Discharges”. In: *Physical Review* 28.4 (Oct. 1926). Pp. 727–763. DOI: 10.1103/PhysRev.28.727.
- [NSS02] S Niedner, B D Scott, and U Stroth. “Statistical properties of drift wave turbulence in low-temperature plasmas”. In: *Plasma Physics and Controlled Fusion* 44.4 (2002). Pp. 397–408. DOI: 10.1088/0741-3335/44/4/301.
- [OL02] M. Otte and J. Lingertat. “Initial Results of Magnetic Surface Mapping in the WEGA Stellarator”. In: *29th EPS Conference on Plasma Phys. and Contr. Fusion Montreux*. 2002.
- [OLW03] M. Otte, J. Lingertat, and F. Wagner. “Operation of the WEGA Stellarator with Vertical Field and Compensation Coils”. In: *30th EPS Conference on Plasma Phys. and Contr. Fusion St. Petersburg*. 2003.
- [Ott+07a] M. Otte et al. “Experimental Results from the WEGA Stellarator”. In: *34. EPS Conference on Plasma Phys. Warsaw*. Vol. 31F. 2007. P–2.145. URL: http://epsppd.epfl.ch/Warsaw/pdf/P2_145.pdf.
- [Ott+07b] M. Otte et al. “The WEGA Stellarator: Results and Prospects”. In: *PLASMA 2007: 4th German-Polish Conference on Plasma Diagnostics for Fusion and Applications; 6th French-Polish Seminar on Thermal Plasma in Space and Laboratory*. 2007.
- [Ped+01] M A Pedrosa et al. “Experimental evidence of fluctuation-induced inward transport linked to rational surfaces in the TJ-II stellarator”. In: *Plasma Physics and Controlled Fusion* 43.11 (2001). Pp. 1573–1582. DOI: 10.1088/0741-3335/43/11/311.
- [Ped+04] M A Pedrosa et al. “Interplay between parallel and perpendicular sheared flows and fluctuations in the plasma boundary region of the TJ-II stellarator”. In: *Plasma Physics and Controlled Fusion* 46.1 (2004). Pp. 221–231. DOI: 10.1088/0741-3335/46/1/014.
- [Ped+00] M. Pedrosa et al. “Role of rational surfaces on fluctuations and transport in the plasma edge of the TJ-II stellarator”. In: *Czechoslovak Journal of Physics* 50.12 (Dec. 2000). Pp. 1463–1470. DOI: 10.1023/A:1022859915916.
- [Pfe+98] U. Pfeiffer et al. “Density, Temperature and Potential Fluctuation Measurements with Multiple Fast Swept Langmuir Probe on W7-AS”. In: *Contributions to Plasma Physics* 38.special issue (1998). Pp. 134–144.
- [Pod+07] Y. Y. Podoba et al. “Direct Observation of Electron-Bernstein Wave Heating by O-X-B-Mode Conversion at Low Magnetic Field in the WEGA Stellarator”. In: *Physical Review Letters* 98.25, 255003 (2007). P. 255003. DOI: 10.1103/PhysRevLett.98.255003.

-
- [Pow74] E. J. Powers. “Spectral techniques for experimental investigation of plasma diffusion due to polychromatic fluctuations”. In: *Nuclear Fusion* 14.5 (1974). Pp. 749–752.
- [Rah07] Kian Rahbarnia. “Charakterisierung der elektromagnetischen Turbulenz im Torsatron TJ-K”. PhD thesis. Universität Stuttgart, 2007.
- [Ram+05] M. Ramisch et al. “ ρ_s scaling of characteristic turbulent structures in the torsatron TJ-K”. In: *Physics of Plasmas* 12.3, 032504 (2005). P. 032504. DOI: 10.1063/1.1857531.
- [RS05] D. Reiser and B. Scott. “Electromagnetic fluid drift turbulence in static ergodic magnetic fields”. In: *Physics of Plasmas* 12.12, 122308 (2005). P. 122308. DOI: 10.1063/1.2141928.
- [Rey74] A J Reynolds. *Turbulent flows in engineering*. Wiley-Interscience, 1974.
- [Rey83] Osborne Reynolds. “An Experimental Investigation of the Circumstances Which Determine Whether the Motion of Water Shall Be Direct or Sinuous, and of the Law of Resistance in Parallel Channels”. In: *Philosophical Transactions of the Royal Society of London* 174 (1883). Pp. 935–982. ISSN: 0261-0523.
- [RRB93] T.L. Rhodes, C.P. Ritz, and R.D. Bengtson. “Scaling of far edge plasma turbulence and fluctuation induced particle transport in the TEXT tokamak”. In: *Nuclear Fusion* 33.8 (1993). Pp. 1147–1163. DOI: 10.1088/0029-5515/33/8/I05.
- [Rit+88] Ch. P. Ritz et al. “Advanced plasma fluctuation analysis techniques and their impact on fusion research (invited)”. In: *Review of Scientific Instruments* 59.8 (1988). Pp. 1739–1744. DOI: 10.1063/1.1140098.
- [Ros+66] M. N. Rosenbluth et al. “Destruction of Magnetic Surfaces by Magnetic Field Irregularities”. In: *Nuclear Fusion* 6 (1966). Pp. 297–300.
- [Ros92] D W Ross. “On standard forms for transport equations and quasi-linear fluxes”. In: *Plasma Physics and Controlled Fusion* 34.2 (1992). Pp. 137–146. DOI: 10.1088/0741-3335/34/2/001.
- [Rud90] Alexander Rudyj. “Untersuchung transportrelevanter Fluktuationen in der Randschicht von ASDEX”. IPP Report III/160. PhD thesis. Max Planck Institut für Plasmaphysik, Garching: Technische Universität München, 1990.
- [San+00] E. Sanchez et al. “Statistical characterization of fluctuation wave forms in the boundary region of fusion and nonfusion plasmas”. In: *Physics of Plasmas* 7.5 (2000). Pp. 1408–1416. DOI: 10.1063/1.873958.
- [Sch05] M. Schubert. “Fluctuations of Temperature and Turbulent Radial Energy Transport in the Edge Plasma of the We 7-AS Stellarator”. PhD thesis. Ernst-Moritz-Arndt-Universität Greifswald, 2005.

- [SET07] M. Schubert, M. Endler, and H. Thomsen W7-AS Team. “Spatiotemporal temperature fluctuation measurements by means of a fast swept Langmuir probe array”. In: *Review of Scientific Instruments* 78.5, 053505 (2007). P. 053505. DOI: 10.1063/1.2740785.
- [Sch94] U. Schumacher. “WEGA Akteuller Stand und mögliche Arbeitsgebiete”. Besprechungsprotokoll, IpF Stuttgart. 1994.
- [Sco00] B. Scott. “Low Frequency Fluid Drift Turbulence in Magnetised Plasmas”. IPP report 5/92, March 2001, Max-Planck-Institut für Plasma-physik, Garching bei München. Habilitation thesis. Heinrich-Heine-Universität Düsseldorf, 2000.
- [Sco97a] B Scott. “Three-dimensional computation of collisional drift wave turbulence and transport in tokamak geometry”. In: *Plasma Physics and Controlled Fusion* 39.3 (1997). Pp. 471–504. DOI: 10.1088/0741-3335/39/3/010.
- [Sco97b] B Scott. “Three-dimensional computation of drift Alfvén turbulence”. In: *Plasma Physics and Controlled Fusion* 39.10 (1997). Pp. 1635–1668. DOI: 10.1088/0741-3335/39/10/010.
- [Sco06] Bruce D Scott. “Computation of turbulence in magnetically confined plasmas”. In: *Plasma Physics and Controlled Fusion* 48.12B (2006). B277–B293. DOI: 10.1088/0741-3335/48/12B/S27.
- [Sco07] Bruce D Scott. “Tokamak edge turbulence: background theory and computation”. In: *Plasma Physics and Controlled Fusion* 49.7 (2007). S25–S41. DOI: 10.1088/0741-3335/49/7/S02.
- [SPC74] D. E. Smith, E. J. Powers, and G. S. Caldwell. “Fast-Fourier-Transform Spectral-Analysis Techniques as a Plasma Fluctuation Diagnostic Tool”. Ed. by E. J. Powers. In: *Plasma Science, IEEE Transactions on* 2.4 (1974). Pp. 261–272. ISSN: 0093-3813. DOI: 10.1109/TPS.1974.4316849.
- [SJ58] Lyman Spitzer Jr. “The Stellarator Concept”. In: *Physics of Fluids* 1.4 (1958). Pp. 253–264. DOI: 10.1063/1.1705883.
- [Sre99] Katepalli R. Sreenivasan. “Fluid turbulence”. In: *Rev. Mod. Phys.* 71.2 (Mar. 1999). S383–S395. DOI: 10.1103/RevModPhys.71.S383.
- [Sta95] P. C. Stangeby. “A problem in the interpretation of tokamak Langmuir probes when a fast electron component is present”. In: *Plasma Physics and Controlled Fusion* 37.9 (1995). Pp. 1031–1037. DOI: 10.1088/0741-3335/37/9/008.
- [Sto+99] J. Stockel et al. “Magnetic and electrostatic fluctuations in the CASTOR tokamak”. In: *Plasma Physics and Controlled Fusion* 41.3A (1999). A577–A585. DOI: 10.1088/0741-3335/41/3A/051.

- [Str+04] U. Stroth et al. “Study of edge turbulence in dimensionally similar laboratory plasmas”. In: *Physics of Plasmas* 11.5 (2004). Pp. 2558–2564. DOI: 10.1063/1.1688789.
- [TS61] I. E. Tamm and A. D. Sakharov. “Theory of a magnetic thermonuclear reactor (Part I,II,III)”. In: *Plasma Physics and the Problem of Controlled Thermonuclear Reactions*. Ed. by M.A. Leontovich. Vol. 1. 1961. P. 1.
- [Tan+02] K Tanaka et al. “Influence of the static magnetic island on the density profiles in LHD”. In: *Plasma Physics and Controlled Fusion* 44.5A (2002). A231–A235. DOI: 10.1088/0741-3335/44/5A/322.
- [TL72] H. Tennekes and J. L. Lumley. *A First Course in Turbulence*. MIT Press, 1972. URL: <http://books.google.de/books?id=h4coCj-1N0cC>.
- [TD85] P. W. Terry and P. H. Diamond. “Theory of dissipative density-gradient-driven turbulence in the tokamak edge”. In: *Physics of Fluids* 28.5 (1985). Pp. 1419–1439. DOI: 10.1063/1.864977.
- [The90] Gottfried Theimer. “Methoden zur Untersuchung der räumlichen Struktur von Dichtafluktuationen in der Randschicht von Fusionsexperimenten demonstriert am Divertortokamak ASDEX”. Laborbericht IPP III/169, Max-Planck-Institut für Plasmaphysik, Garching. MA thesis. Technische Universität München, 1990.
- [Tho+02] H. Thomsen et al. “Parallel correlation measurements in the scrape-off layer of the Joint European Torus”. In: *Physics of Plasmas* 9 (Apr. 2002). Pp. 1233–1240. DOI: 10.1063/1.1454122.
- [Tho+01] H. Thomsen et al. “Parallel Correlation Studies of Fluctuations and the Impact of Perturbations in the Magnetic Configuration”. In: *Contributions to Plasma Physics* 41.5 (2001). Pp. 530–536. DOI: 10.1002/1521-3986(200109)41:5<530::AID-CTPP530>3.0.CO;2-W.
- [Tho02] Henning Thomsen. “A dynamics investigation into edge plasma turbulence”. PhD thesis. Ernst-Moritz-Arndt-Universität Greifswald, 2002.
- [Tsa+78] K. T. Tsang et al. ““Absolute Universal Instability” Is Not Universal”. In: *Physical Review Letters* 40.5 (Jan. 1978). Pp. 327–331. DOI: 10.1103/PhysRevLett.40.327.
- [Tsu92] H. Y. W. Tsui. “Formation of a velocity shear layer in confined plasmas”. In: *Physics of Fluids B: Plasma Physics* 4.12 (1992). Pp. 4057–4061. DOI: 10.1063/1.860312.
- [VD82] Milton Van Dyke. *An Album of Fluid Motion*. Stanford, CA: Parabolic Press, 1982.
- [Wag94] F Wagner. “Collisional transport and neo-classical aspects in toroidal confinement”. In: *Contributions to high temperature plasma physics*. Ed. by K. H. Spatschek and J. Uhlenbusch. Akademie Verlag, 1994.

- [WS93] F Wagner and U Stroth. “Transport in toroidal devices—the experimentalist’s view”. In: *Plasma Physics and Controlled Fusion* 35.10 (1993). Pp. 1321–1371. DOI: 10.1088/0741-3335/35/10/002.
- [WH84] Masahiro Wakatani and Akira Hasegawa. “A collisional drift wave description of plasma edge turbulence”. In: *Physics of Fluids* 27.3 (1984). Pp. 611–618. DOI: 10.1063/1.864660.
- [WD83] R. E. Waltz and R. R. Dominguez. “Drift-wave turbulence with wave–wave and wave–particle nonlinear effects in a sheared slab”. In: *Physics of Fluids* 26.11 (1983). Pp. 3338–3349. DOI: 10.1063/1.864071.
- [War+06] G.B. Warr et al. “New 28 GHz Plasma ECR Heating System for the WEGA Stellarator”. In: *33. EPS Conference on Plasma Phys., Rome*. 2006. URL: http://epsppd.epfl.ch/Warsaw/pdf/P2_145.pdf.
- [Wat+08] F. Watanabe et al. “Effects of an externally produced static magnetic island on edge MHD modes in the Large Helical Device”. In: *Nuclear Fusion* 48.2 (2008). 024010 (8pp). DOI: 10.1088/0029-5515/48/2/024010.
- [Wv35] Weizsäcker and C. F. v. “Zur Theorie der Kernmassen”. In: *Zeitschrift für Physik A Hadrons and Nuclei* 96.7 (July 1935). Pp. 431–458. DOI: 10.1007/BF01337700.
- [Wer] Andreas Werner. *private communication*.
- [Wes97] John Wesson. *Tokamaks*. Clarendon Press, 1997.
- [WH87] P.-Th. Wilrich and H.-J. Henning. *Formeln und Tabellen der angewandten mathematischen Statistik*. Springer-Verlag, 1987.
- [W GK06] T. Windisch, O. Grulke, and T. Klinger. “Radial propagation of structures in drift wave turbulence”. In: *Physics of Plasmas* 13.12, 122303 (2006). P. 122303. DOI: 10.1063/1.2400845.
- [Win+97] D. L. Winslow et al. “Determination of field line location and safety factor in TEXT-U”. In: *Review of Scientific Instruments* 68.1 (1997). Pp. 396–399. DOI: 10.1063/1.1147838.
- [Wob94] H Wobig. *Plasma confinement in toroidal systems*. Tech. rep. Grimnetz (Ch): Max-Planck-Institut für Plasmaphysik, 1994.
- [WF88] H Wobig and R H Fowler. “The effect of magnetic surface destruction on test particle diffusion in the Wendelstein VII-A stellarator”. In: *Plasma Physics and Controlled Fusion* 30.6 (1988). Pp. 721–741. DOI: 10.1088/0741-3335/30/6/006.
- [Wob+87] H. Wobig et al. “Plasma confinement in the Wendelstein VII-A stellarator”. In: *Plasma Physics and Controlled Nuclear Fusion Research*. Vol. 2. Proc. 11th Int. Conf. Kyoto, 1986. IAEA. Vienna 1987. P. 369.

- [Wob99] Horst Wobig. “Theory of advanced stellarators”. In: *Plasma Physics and Controlled Fusion* 41.3A (1999). A159–A173. DOI: 10.1088/0741-3335/41/3A/010.
- [WTP92] A J Wootton, H Y W Tsui, and S Prager. “Edge turbulence in tokamaks, stellarators and reversed field pinches”. In: *Plasma Physics and Controlled Fusion* 34.13 (1992). Pp. 2023–2030. DOI: 10.1088/0741-3335/34/13/035.
- [Woo+90] A. J. Wootton et al. “Fluctuations and anomalous transport in tokamaks”. In: *Physics of Fluids B: Plasma Physics* 2.12 (1990). Pp. 2879–2903. DOI: 10.1063/1.859358.
- [Yag01] A. Yaglom. “The Century of Turbulence Theory: The Main Achievements and Unsolved Problems”. In: *New trends in turbulence Turbulence: nouveaux aspects*. Ed. by M. Lesieur, A. Yaglom, and F. David. 2001. Pp. 1–52. DOI: 10.1007/3-540-45674-0_1. URL: http://dx.doi.org/10.1007/3-540-45674-0_1.
- [Zwe+07] S J Zweben et al. “Edge turbulence measurements in toroidal fusion devices”. In: *Plasma Physics and Controlled Fusion* 49.7 (2007). S1–S23. DOI: 10.1088/0741-3335/49/7/S01.

Danksagung

An dieser Stelle möchte ich allen Menschen danken, die mich auf dem langen Weg bis zur Fertigstellung dieser Arbeit begleitet und unterstützt haben.

An erster Stelle sei die enorme Leistung meiner Frau Evelyn erwähnt, die mir durchweg den Rücken frei hielt, um mir die Konzentration auf meine Arbeit zu ermöglichen. Neben unseren Kindern hatte Sie oft noch einen vierten Patienten zu versorgen. Ihre Leistung grenzte zeitweise ans Übermenschliche.

Unsere Kinder, Lola, Frieda und Alva, mussten regelmäßig meine rein physische Anwesenheit ertragen. Für das nicht selbstverständliche Verständnis bedanke ich mich und gelobe Besserung.

Meinem Betreuer Prof. Friedrich Wagner danke ich für seine langjährige Unterstützung auf dem Weg zur Promotion. Im Laufe der Promotion gab er viele richtungsweisende Anregungen und stand mir jederzeit für Fragen offen.

Dr. Matthias Otte danke ich für sein reges Interesse am Fortgang meiner Arbeit und für die fachliche Unterstützung, insbesondere bei der Suche nach unentdeckten Inseln. Weiterhin sei Dr. Otte für das entgegengebrachte Vertrauen gedankt, meine Messkampagnen weitgehend selbständig planen und durchführen zu können. Nicht zu vergessen sein ausdauerndes Korrekturlesen meiner Arbeit.

Dr. Michael Endler danke ich neben der regelmäßigen Versorgung mit frischen (bzw. nicht mehr ganz so frischen) Tektronix Verstärkern für seine fachliche Unterstützung meiner Arbeit und seine Diskussionsbereitschaft. Seine fachliche Kompetenz auf dem Gebiet der Plasmaturbulenz half an einigen Stellen Irrwege zu verlassen und einstürzende Kartenhäuser wieder auf zu bauen.

Dieter Aßmus danke ich für die Lehrstunden in Sachen Maschinenführung und viele nützliche Hinweise zu Messtechnik und Erdschleifen. Auch hier erneut der Dank für das Vertrauen mich selbständig an der Maschine arbeiten zu lassen.

Norbert Paschkowski sei einerseits für die technische Unterstützung beim Aufbau der verwendeten Sondendiagnostiken gedankt. Es war ein beruhigendes Gefühl zu wissen, dass alles benötigte Material zur rechten Zeit am rechten Ort ist und fixe Ideen aus dem Bereich „Jugend forscht“ auch in die Tat umgesetzt werden können. Für die Nachhilfestunden in Sachen Sondenbau auch ein herzliches Dankeschön.

Dr. Martin Schubert danke ich für die motivierende fachliche Unterstützung zu Beginn dieser Arbeit und für die Überlassung vieler nützlicher IDL Routinen.

Allen Kollegen, die mich mit Korrekturen und Hinweisen zur vorliegenden Arbeit versorgt haben sei gedankt. Namentlich in IPP Konvention: Dr. Daniel Andruczyk, Dr. Joachim Geiger, Oliver Lischtschenko, Torsten Stange, Dr. Henning Thomsen

Special thanks go to Horst Punzet from Ireland for his helpful online reviewing of my written english without actually understanding very much of what I am writing about.

Schlussendlich möchte ich meinen Eltern für das danken wozu sie mich gemacht haben und was Grundvoraussetzung für eine erfolgreiche Promotion ist. Der zu erwerbende akademische Grad eines doctor bescheinigt die Fähigkeit zu selbständiger wissenschaftlicher Arbeit was die vorige Erziehung zur Selbständigkeit voraussetzt.

Hiermit erkläre ich, dass diese Arbeit bisher von mir weder an der Mathematisch-Naturwissenschaftlichen Fakultät der Ernst-Moritz-Arndt-Universität Greifswald noch einer anderen wissenschaftlichen Einrichtung zum Zwecke der Promotion eingereicht wurde.

Ferner erkläre ich, dass ich diese Arbeit selbständig verfasst und keine anderen als die darin angegebenen Hilfsmittel benutzt habe.

Lebenslauf von Stefan Marsen

Geboren am 28. Juni 1977 in Frankfurt am Main.

Familienstand: verheiratet, 3 Kinder

Schulbildung

Tilemannschule Limburg, Gymnasium. Sekundarstufe I

Friedrich-Dessauer-Schule Limburg, Fachoberschule. Fachrichtung Elektrotechnik.

Abschluss: Fachhochschulreife.

Studium

- SS 1998 Immatrikulation an der Fachhochschule Stralsund,
Studienrichtung Elektrotechnik, Diplom (FH).
- ab WS 1999/2000 Wahl der Vertiefungsrichtung:
Nutzung regenerativer Energiequellen.
- SS 2001 Praxissemester am Max-Planck-Institut für Plasmaphysik,
Greifswald. Thema:
*„Entwicklung und Implementierung einer Steuerungs- und
Überwachungs-Software für den Stellarator WEGA“*
- 2002 Diplomarbeit am Max-Planck-Institut für
Plasmaphysik, Greifswald. Thema:
*„Entwicklung und Erprobung einer Hallsonde zur
Untersuchung des Magnetfeldes im Stellarator WEGA“*
- 2002 Studienabschluss: Diplom-Ingenieur (FH).

Lehrtätigkeit

- 2003-2005 Gestaltung und Durchführung des Physikalischen Praktikum
in Fachbereich Elektrotechnik und Informatik der
FH Stralsund.
Einführungsvorlesungen zum Thema: *Fehlerrechnung*
Durchführung von Übungsseminaren

Promotion

- SS 2003 Immatrikulation an der Ernst-Moritz-Arndt-Universität Greifswald. Promotionsstudiengang *Greifswald Graduate School in Science (GGSS)*
- 2003-2005 Aufbauphase der GGSS.
- 2005 Abschluss der Aufbauphase durch mündliche Prüfung und Anfertigung einer Abschlussarbeit, Thema:
„*Vorbetrachtungen zu Fluktuationsuntersuchungen am Stellarator WEGA.*“
- 2005-2008 Doktorand am Max-Planck-Institut für Plasmaphysik
Thema der Doktorarbeit:
„*Die räumlich-zeitliche Struktur elektrostatischer Turbulenz am Stellarator WEGA.*“

Sommerschulen und Konferenzen

- “*Summer University for Plasma Physics*“, Greifswald, September 2005.
- “*70. Frühjahrstagung der Deutschen Physikalischen Gesellschaft*“, Augsburg, 2006.
- “*71. Frühjahrstagung der Deutschen Physikalischen Gesellschaft*“, Düsseldorf, 2007.
- “*7th International Workshop on Electrical Probes in Magnetised Plasmas*“
Prag, 2007.

Konferenzbeiträge

Poster

Marsen, S., M. Otte, and F Wagner. “Messung elektrostatischer Turbulenz im Stellarator WEGA”. In: *Frühjahrstagung der Deutschen Physikalischen Gesellschaft, Augsburg*. Augsburg, Germany 2006.

Marsen, S., M. Otte, M. Schubert, and F Wagner. “Zur Struktur turbulent Fluktuationen im Stellarator WEGA”. In: *Frühjahrstagung der Deutschen Physikalischen Gesellschaft, Düsseldorf*. Düsseldorf, Germany 2007.

Vorträge

Marsen, S., M. Otte, and F Wagner. “Structure of Turbulence in the WEGA Stellarator”. In: *7th International Workshop on Electrical Probes in Magnetised Plasmas*. Prague, CZ 2007.

Veröffentlichungen

Als Erstautor

Marsen, S., M. Otte, and F Wagner. “Three-dimensional Structure of Turbulence in the WEGA Stellarator”. In: *Contributions to Plasma Physics* (2008). accepted for publication.

Als Koautor

Warr, G. B., O. Chmyga, E. Holzhauser, J. Howard, W. Kasperek, D. Keil, R. König, H. P. Laqua, M. Laux, J. Lingertat, O. Lischtschenko, S. Marsen, M. Otte, Y. Podoba, M. Schubert, F. Wagner, A. Weller, D. Zhang, and O. Zhezhera. “Overview of WEGA Stellarator Results and Plans”. In: *7th Australia-Japan Workshop on Plasma Physics and Diagnostics*. Toki, Japan 2005.

Otte, M., O. Lischtschenko, S. Marsen, M. Schubert, Y. Y. Podoba, F. Wagner, G. B. Warr, L.I. Krupnik, A.V. Melnikov, and A.I. Zhezhera. “Five years of WEGA operation at IPP Greifswald”. In: *Stellarator News* 106 (2006).

Warr, G.B., H.P. Laqua, D. Assmus, W. Kasperek, D. Keil, O. Lischtschenko, S. Marsen, M. Otte, M. Schubert, and F. Wagner. “New 28 GHz Plasma ECR Heating System for the WEGA Stellarator”. In: *33. EPS Conference on Plasma Phys., Rome*. 2006. URL: http://epsppd.epfl.ch/Warsaw/pdf/P2_145.pdf.

Laqua, H. P., S. Marsen, M. Otte, Y. Podoba, J. Preinhalter, and J. Urban. “Direct Measurement of the Electron Bernstein Wave Absorption and Current Drive at the WEGA Stellarator.”. In: *49th Annual Meeting of the Division of Plasma Physics of the APS*. Orlando, FL 2007.

- Laqua, H.P., D. Andruczyk, E. Holzhauser, S. Marsen, M. Otte, Y. Y. Podoba, J. Preinhealter, J. Urban, and G. B. Warr. “Electron Cyclotron Wave Experiments at the WEGA Stellarator”. In: *34. EPS Conference on Plasma Phys. Warsaw*. Vol. 31F. 2007. P–1.154. URL: http://epsppd.epfl.ch/Warsaw/pdf/P2_145.pdf.
- Otte, M., D. Andruczyk, A. Komarov, A. Kozachek, L. Krupnik, H.P. Laqua, O. Lischtschenko, S. Marsen, Y.Y. Podoba, M. Schubert, F. Wagner, G.B. Warr, and A. Zhezhera. “Experimental Results from the WEGA Stellarator”. In: *34. EPS Conference on Plasma Phys. Warsaw*. Vol. 31F. 2007. P–2.145. URL: http://epsppd.epfl.ch/Warsaw/pdf/P2_145.pdf.
- Otte, M., D. Andruczyk, E. Holzhauser, J. Howard, R. König, L. Krupnik, H. P. Laqua, O. Lischtschenko, S. Marsen, J. Schacht, J. Urban, Y. Y. Podoba, J. Preinhalter, F. Wagner, G. B. Warr, and A. Zhezhera. “The WEGA Stellarator: Results and Prospects”. In: *PLASMA 2007: 4th German-Polish Conference on Plasma Diagnostics for Fusion and Applications; 6th French-Polish Seminar on Thermal Plasma in Space and Laboratory*. 2007.
- Podoba, Y. Y., H. P. Laqua, G. B. Warr, M. Schubert, M. Otte, S. Marsen, F. Wagner, and E. Holzhauser. “Direct Observation of Electron-Bernstein Wave Heating by O-X-B-Mode Conversion at Low Magnetic Field in the WEGA Stellarator”. In: *Physical Review Letters* 98.25, 255003 (2007). P. 255003. DOI: 10.1103/PhysRevLett.98.255003.
- Laqua, H. P. and D. Andruczyk, S. Marsen, M. Otte, Y. Y. Podoba, J. Preinhealter, and J. Urban. “Experiments With Electron Bernstein Waves At The WEGA Stellarator”. In: *15th Joint Workshop on Electron Cyclotron Emission and Electron Cyclotron Resonance Heating*. 2008.